Towards a non-contact determination of the mechanical properties of soft condensed matter using AFM

Erik Abegg

THÈSE

Pour obtenir le grade de

DOCTEUR DE L'UNIVERSITÉ GRENOBLE ALPES

Spécialité : NANOPHYSIQUE

Arrêté ministériel : 25 mai 2016

Présentée par

Erik ABEGG

Thèse dirigée par **Elisabeth CHARLAIX**
et codirigée par **Joël CHEVRIER**

préparée au sein du **Laboratoire Laboratoire Interdisciplinaire de Physique**
dans **l'École Doctorale Physique**

Vers une détermination sans contact des propriétés mécaniques de matière condensée molle avec AFM

Towards a non-contact determination of the mechanical properties of soft condensed matter using AFM

Thèse soutenue publiquement le **6 novembre 2020**,
devant le jury composé de :

Monsieur ALESSANDRO SIRIA
CHARGE DE RECHERCHE HDR, CNRS DELEGATION PARIS-CENTRE, Rapporteur
Monsieur HUBERT KLEIN
MAITRE DE CONFERENCES HDR, AIX-MARSEILLE UNIVERSITE, Rapporteur
Monsieur AHMAD BSIESY
PROFESSEUR DES UNIVERSITES, UNIVERSITE GRENOBLE ALPES, Président
Monsieur CHRISTIAN FRETIGNY
DIRECTEUR DE RECHERCHE HDR, CNRS DELEGATION PARIS-CENTRE, Examinateur
Monsieur GEORGES BREMOND
PROFESSEUR, INSA LYON, Examinateur

Abstract

Accurate determination of elasticity below the microscale through indentation measurements on soft materials is difficult as it is beyond the limits of conventional contact mechanical models. Surface energy contributions dominate the interaction and preclude accurate determination of bulk material elasticity. As a solution to this problem a non-contact measuring method in liquid was developed on the Surface Force Apparatus (SFA) that allows for an absolute determination of elasticity without solid-solid contact. While successful, the SFA has limitations in terms of compatible sample thickness and frequency range due to the macroscopic size of the employed probe. In this manuscript we report on implementation of the non-contact measuring technique on an Atomic Force Microscope (AFM), where smaller probes can be used and a higher frequency range is available. Conventional mechanical piezoacoustic excitation of the AFM probe was found to be experimentally insufficient. A capacitive excitation scheme was developed to resolve this. To implement and explore this new excitation scheme a homemade AFM setup was rebuilt. The performance of this rebuild AFM is demonstrated by performing reference measurements on a rigid substrate in PDMS oil and deionized water. We additionally report on the investigation of p-NIPAM polymer brush surfaces using AFM, where we found a previously unreported bridging interaction below the lower critical solution temperature. Lastly we report on the investigation of quick clay, a soil type associated with landslides. We demonstrate the capability of AFM to investigate the clay microstructure in its natural water saturated state and explore the mechanical properties of clay on the micro- and nanoscale. These results open the door for AFM to contribute in answering key questions in the field of clay geology.

Résumé

La détermination précise de l'élasticité en dessous de l'échelle microscopique par des mesures d'indentation sur des matériaux mous est difficile car elle dépasse les limites des modèles mécaniques de contact conventionnels. Les contributions d'énergie de surface dominent l'interaction et empêchent une détermination précise de l'élasticité en volume du matériau. Pour résoudre ce problème, une méthode de mesure sans contact dans un liquide a été développée sur le Surface Force Apparatus (SFA) permet une détermination absolue de l'élasticité sans contact solide-solide. Bien que réussie, le SFA présente des limites en termes d'épaisseur d'échantillons minces et de plage de fréquences en raison de la taille macroscopique de la sonde utilisée. Dans ce manuscrit, nous rendons compte de la mise en œuvre de la technique de mesure sans contact sur la plate-forme AFM (Atomic Force Micrsocope), où des sondes plus petites peuvent être utilisées et une gamme de fréquences plus large est disponible. L'excitation mécanique piézoacoustique conventionnelle de la sonde AFM s'est avérée insuffisante en milieu liquide et un schéma d'excitation capacitive a été développé pour résoudre ce problème. Pour implémenter et explorer ce nouveau schéma d'excitation, une configuration AFM "maison" a été reconstruite. Le potentiel de cet AFM est démontré en effectuant des mesures de référence sur un substrat rigide dans de l'huile pdms et de l'eau déionisée. Nous rendons également compte de l'étude des surfaces des brosses en polymère p-NIPAM à l'aide de AFM, où nous avons trouvé une interaction de pontage non signalée en dessous de la température de solution critique inférieure. Enfin, nous présentons de nouvelles mesures par AFM sur les argiles dites "quick clay", constituant d'un type de sol sujet à des glissements de terrain impressionnants. Nous démontrons la capacité de l'AFM à étudier la microstructure de l'argile dans son état naturel saturé en eau et à explorer les propriétés mécaniques de l'argile à l'échelle micro et nanométrique. Ces résultats ouvrent la voie à l'AFM pour contribuer à répondre à des questions clés dans ce domaine de la géologie où les argiles sont des matériaux importants.

Acknowledgements

First of all I would like to deeply thank my thesis supervisors Joël Chevrier and Elisabeth Charlaix for guiding me through my thesis project. I want to thank Joël for all the knowledge he bestowed upon me, both about the field of AFM and life as scientist in general, and all the lunch meetings that never failed to reinvigorate my motivation. I want to thank Elisabeth for always providing so many ideas to pursue.
I am very grateful to the Fondation Nanoscience for providing the grant that allowed me to work on my thesis subject for three years.
I would also like to thank Pieter-Jan van Zwol, who introduced me to Joël and Elisabeth and inspired me to pursue the completion of my scientific education with a PhD.
I would like to thank Simon Carpentier for introducing me to the AFM setup, teaching me the ropes and for housing me during my first days in France.
A special thanks to Jérôme Giraud for the CAD designs of the AFM setup, the engineering knowledge he shared and his infinite patience with my French during our first meetings.
I would like to warmly thank Elise Lorenceau for the many times she helped me in administrative matters, even though this technically was not part of her responsibilities.
Thanks to Lionel Bureau for teaching me about p-NIPAM, providing the p-NIPAM samples and the fruitful discussions on this subject.
A thanks to all the members of the MODI team and other people at the LiPhy who helped me during my thesis project. Specifically Benjamin Cross for sharing his general knowledge on force sensor experiments and Cyril Picard for helping me with thermal isolation.
A special thanks to the CIME Nanotech for allowing me to make use of their AFMs and Valentine Bolcato for supporting me while using them. I also want to thank Ahmad Bsiesy and Florence Marchi for being part of my *conseil de these* each year.
I would like to thank Jelke Dijkstra and Georgios Birmpilis, for introducing me to their studies on quick clay and providing the clay samples used for this thesis.
I want to thank the people I was in contact with at Bruker: Mickael Febvre, Jerome Beaumale and Alexander Dulebo for their interest in my project and the technical support and equipment that they provided.
I would also like to thank Mario Rodrigues and Miguel Vitorino for inviting me to the beautiful country of Portugal, where they taught me about AFM at the beginning of my thesis, and discussed my results with me at the end.
A big thanks to the many people, in the lab and outside, that shared their friendship with me during these three years in France: Nilankur, Katha, Saranath, Adel, Vanni, Tomas, Dandara, Edouardo, Preeti, Mehdi, Komi, Tim, Morgan, Georges, Celine, Mariana, Laila and others.
I would like to thank all my friends in the Netherlands who supported me at a distance, especially Rik, Wouter, Adriaan and Epco, who have blessed me with their friendship and support for so many years already.
And finally I would like to thank my mother, Marjon, for always confidently believing in me and my sister, Marjolein, for supporting me during all these years.

The manuscript in overview

What follows is a short description of the main results put forward in this manuscript and the topics discussed in each chapter.

Chapter 2 - The homemade AFM system

To facilitate the capacitive excitation measurement in liquid our homemade AFM system has been rebuild. The system was redesigned to be cheaper, robuster and modular. In this chapter we present the design choices we made and why capacitive excitation is the form of excitation best suited for a non-contact measurement in liquid on the AFM platform. A technical overview of the setup and its components is provided.

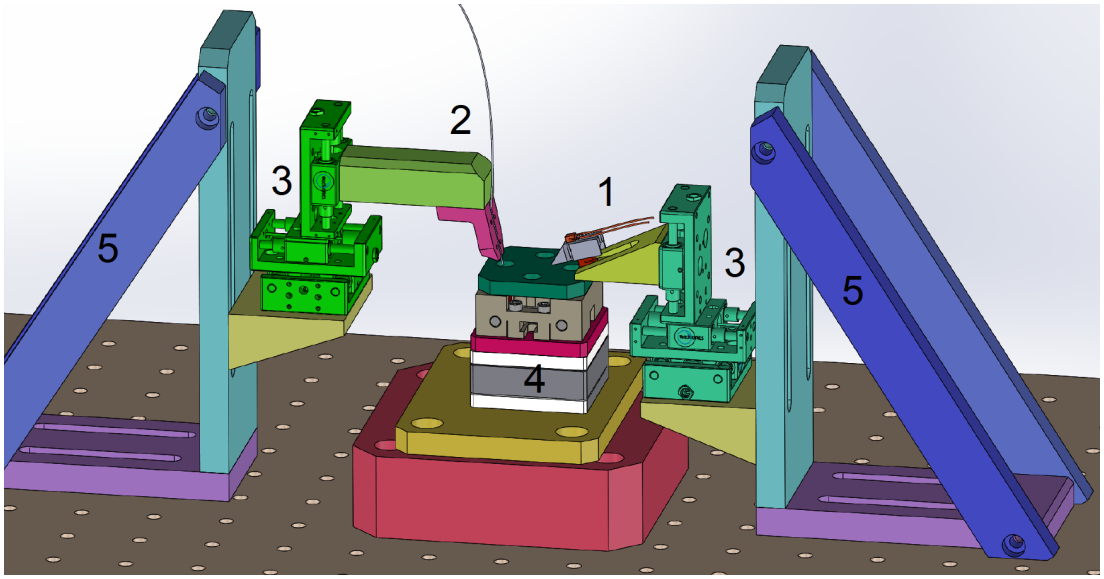

Figure 2.4: Schematic drawing for the homemade AFM platform. Indicated are the: 1) Probe holder, 2) Fiber holder and fiber, 3) Course alignment motors, 4) Fine alignment scanner, 5) Aluminium frame.

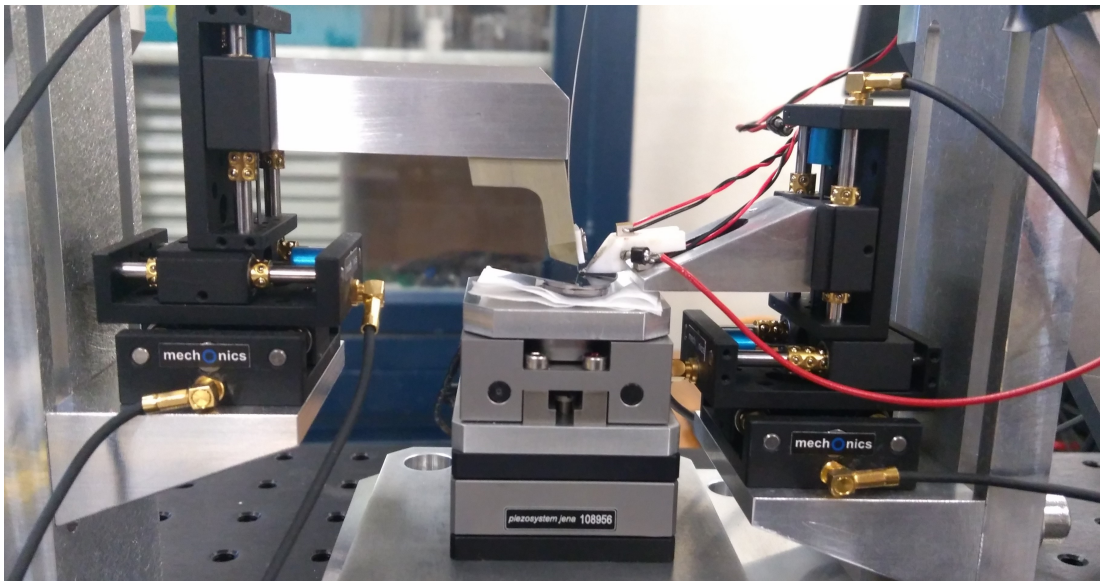

Figure 2.5: Side view of the homemade AFM platform. From left to right: The fiber holder, the sample holder and the tip holder.

Chapter 3 - Theoretical considerations

The use of capacitive excitation in AFM requires some modification of the conventional formalism for converting the measured amplitude and phase data into the mechanical impedance ($\mathcal{Z}$) of the probed interaction. In this chapter we present two methodologies to achieve this. We also explicitly include the dependence of the excitation force on separation.

Chapter 4 - Capacitive excitation in PDMS oil

In this chapter we present the main result of determining $\mathcal{Z}$ using capacitive excitation in PDMS oil on a stiff substrate. Both interpretative methodologies presented in the previous chapter are explored. We demonstrate that the first methodology provides access to $\mathcal{Z}$ at the resonance. The second methodology allows for for accurate measurement of the dissipative component Z'' over a broad frequency range, while the determination of the elastic component Z' is made difficult by a high sensitivity to calibration parameters.

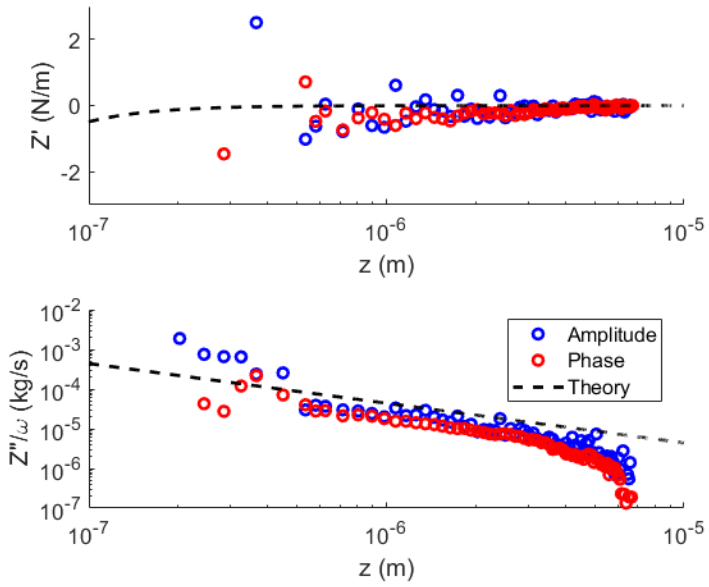

Figure 4.6: The two components of the mechanical impedance $\mathcal{Z}(z)$ as determined through the first methodology by measuring the change in resonance frequency and quality factor using capacitive excitation in PDMS oil. The measurement of $Z'(z)$ follows the electrostatic gradient as expected from the applied voltages, while the measurement of $Z''(z)$ finds the z^{-1} scaling expected from the Reynold's dissipation. The difference with the theoretically predicted values is likely due to residual interactions at the calibration distance of 5 µm from the surface.

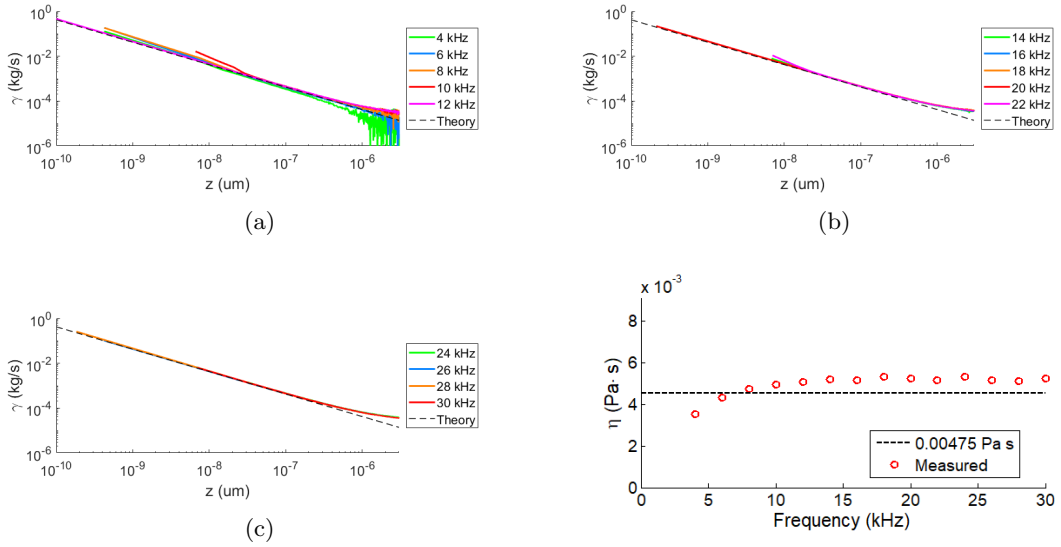

Figure 4.12: (a-c) Found values for the dissipative part of the mechanical impedance $Z''(z)$ as measured at intervals of 2 kHz between 4 to 30 kHz using the second methodology with capacitive excitation in PDMS oil, that follows the change in amplitude and phase at a specific frequency. Between 10 to 500 nm the curves closely follow the values predicted by the Reynold's dissipative force. Figure 4.13c: Fitted value for the viscosity η per frequency. For frequencies below 10 kHz the viscosity is underestimated, while for higher frequencies a consistent value is found.

Chapter 5 - Capacitive Excitation in deionized water

In this chapter we present our first attempts at using capacitive excitation in deionized water to determine $\mathcal{Z}$. While the AFM lever can be excited, the strength of this excitation decreases significantly for small separations. As the driving force cannot be quantified, only the first methodology set out in chapter 3 can be used. We demonstrate that using this methodology it is possible to determine $\mathcal{Z}$ at the resonance frequency of the AFM lever.

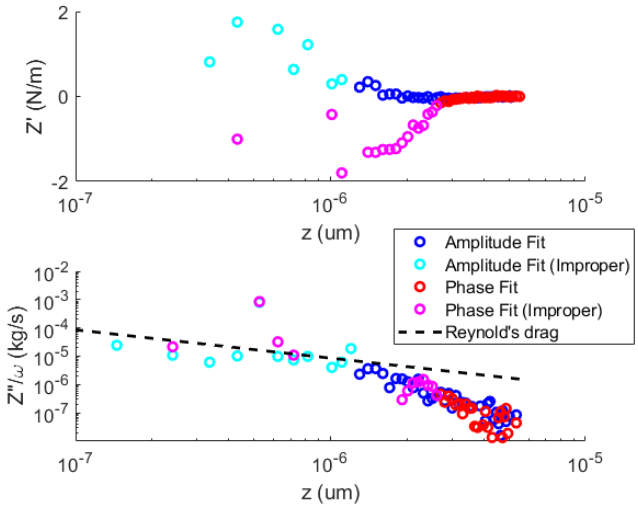

Figure 5.6: Values for $Z'(z)$ and $Z''(z)$ found from ω_0 and Q as determined from the measured amplitude data using capacitive excitation in deioinized water. These curves demonstrate that it is possible to extract the mechanical impedance at resonance from the amplitude and phase curves measured in liquid using capacitive excitation. As the surface potential V_0 is not known, it is not possible to calculate the expected electrostatic gradient. The value found for $Z''(z)$ is underestimated at large separations, but approaches the value predicted by the Reynold's force for smaller separations.

Chapter 6 - P-NIPAM polymer brushes

The investigation of the mechanical properties of polymer brush thin films is an important application of the non-contact measurement on the AFM platform. As a precursor to this investigation, thermosensitive P-NIPAM polymer brushes were investigated through conventional nano-indentation using AFM. In this chapter we present our finding of an anomalous polymer bridging interaction between the AFM probe and brush surface below the temperatures normally required for such interactions.

Chapter 7 - Quick Clay

The last chapter of this manuscript explores the contributions AFM can make to the investigation of water saturated quick-clay, a soil type associated with landslides in the northern hemisphere. We demonstrate the capability of AFM to resolve the micro structure of clay material as it is extracted from the ground with minimal sample preparation. We measure the mechanical response of the material below and above the length scale of its micro structure. These results pave the way for resolving recent discussions on the precise structure of clay materials.

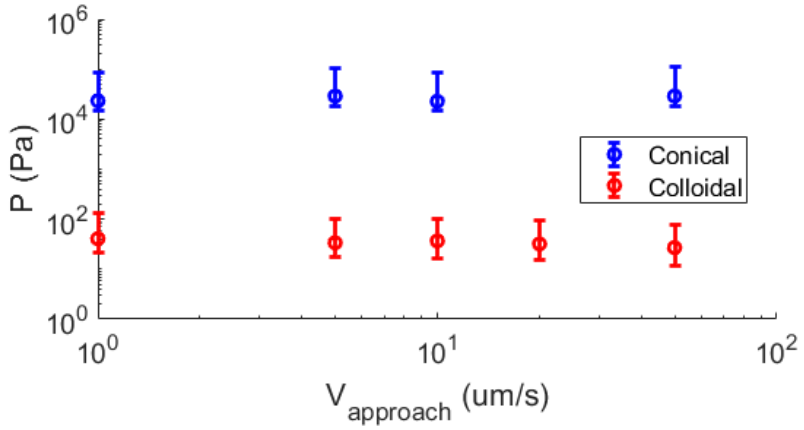

Figure 7.24: Found average pressure near maximum indentation for indentation measurements on the water saturated clay as a function of approach speed for both conical and colloidal indenters

$\langle P \rangle$	Dry	Water Sat.
Conical	0.1 GPa	10 kPa
Colloidal	1 kPa	10 Pa
Ratio	10^5	10^3

Table 7.3: Order of magnitude with which the clay material resists nano and micro indentation in both dry and water saturated state as measured using AFM.

Contents

Chapter 1

Introduction

Contents

The majority of this manuscript will present our work on implementing a non-contact measurement of soft-condensed matter elasticity using capacitively excited Atomic Force Microscopy (AFM). The core issue that we attempt to resolve is accurate determination of soft elastic moduli below the micro scale, where surface energy contributions preclude the use of conventional indentation experiments.

By removing solid-solid contact from the classical indentation experiment and instead applying the indentation force with a confined layer of liquid, we avoid these surface contributions and can determine the absolute elastic modulus of soft matter below the microscale. This non-contact measuring technique is not limited to the resonance frequency of the AFM lever and allows investigation of material properties over a broad range of frequencies using the same probe, something not possible using conventional AFM techniques.

Implementation of this technique on the AFM platform comes with experimental difficulties, as conventional piezoacoustic excitation is ill-suited for quantitative measurements in liquid at frequencies other than the resonance frequency of the cantilever. To resolve this issue a capacitive excitation scheme is implemented that provides the desired analytical transfer function over a broad frequency range. The technique is conceptually demonstrated by presenting experimental data on a rigid surface in PDMS oil and deionized water. Demonstration of the technique on a soft surface is beyond the scope of the manuscript.

To situate this work in its scientific context, this introduction shortly demonstrates the importance of accurate determination of mechanical properties below the microscale in the fields of cellular biology and medicine. It will be illustrated which difficulties prevent application of conventional indentation measurements at such small length scales. Finally we will see how a non-contact measurement can be performed, how it avoids the problems of conventional indentation techniques and what advantages implementation on the AFM platform can bring to the technique.

1.1 Mechanics in cell biology

While the biochemical influences on the proliferation, differentiation and migration of cells have been extensively studied for quite some time, the effect of the micro-mechanical environment on cell development only became an active field of research in the past two decades. [1–4]

Cells are exposed to forces on a broad range of length scales, from the full-body scale of gravity, to shearing forces from the flow of adjacent blood. Cells also exert their own microscopic forces using their actin-myosin cytoskeleton with which they pull on the extra cellular matrix and adjacent cells. They can be regarded as microscopic force sensors, as many of their properties are influenced by the mechanical cues from their surrounding.

To show how the micro-mechanical environment influences cellular properties, we provide some key examples of how the elasticity and surface energy of the surrounding material can determine the fate of a cell.

Mesenchymal stem cell differation

Mesenchymal stem cells are an important candidate for use in stem cell therapy due to their capacity to differentiate into multiple cell lineages including bone, cartilage, fat and muscle. Applications are found in both tissue repair and immune disorder therapy. [5] The mechanical properties of the stem cell micro environment play an important part in its self-renewal and differentiation. [6, 7]

Mesenchymal stem cells grown on softer tissue are found to be more likely to differentiate into myoblast muscle cells, while preferring to become osteoblast bone cells on stiffer substrates. [8–11] Likewise they are more likely to differentiate into neurons on substrates with brain like stiffness, while preferring to differentiate into glials on substrates with a stiffness similar to glial scars. [12] The elastic moduli involved in this differentiation span three orders of magnitude, from 500 Pa for brain tissue to 400 kPa for bone tissue (Fig. 1.1). The surface energy of the micro environment likewise affects differentiation, though the precise mechanism is still poorly understood. [13]

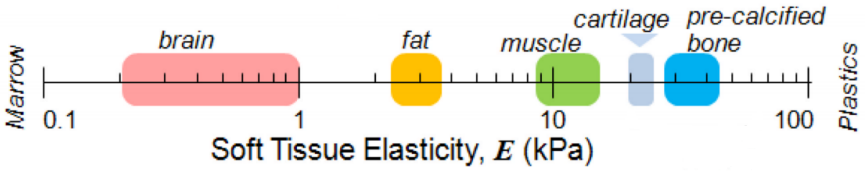

Figure 1.1: The elasticity of mesenchymal stem cell micro-environment, spanning three order orders of magnitude, plays an important role in determining their differentiation type. Taken from [14].

Tissue engineering

For myoblasts the substrate stiffness was found to be an important factor in both proliferation and organization (Fig. 1.2). Using poly-electrolyte multilayer films, it was found that mechanical gradients and patterns can regulate myoblast adhesion and proliferation, both at the single cell level and for multicellular structures. [15–17]

The fusion of myoblasts into myotubes is important in the formation of muscle fibers. Control of this process is critical in skeletal muscle tissue engineering. The fusion of myoblasts

into myotubes was found to be optimal on substrates with a stiffness comparable to tissue. [18] Substrates with a structured elasticity are a promising candidate to control the architecture of the fiber growth. [19]

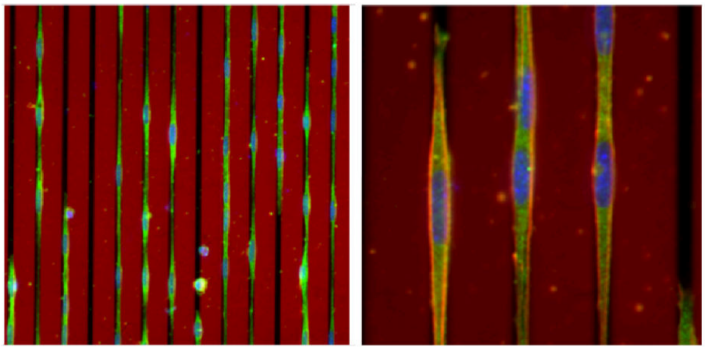

Figure 1.2: Myoblast cells align along lines with a higher stiffness on polyelectrolyte multilayer thin films. Taken from [16].

Elastic gradients are found to drive cell migration, with cells displacing to stiffer regions over time in a process named 'durotaxis'. This behavior was not only found for myoblasts, but also for mesenchymal stem cells and endothelial cells. [20–22]

Medical applications

Determination of cell stiffness is used in medical diagnosis to differentiate cancerous cells from non-cancerous ones, as metastatic cancer cells are found to be 70% softer than benign cells. [23, 24] In fact, the softness of a cell is an indicator of their metastatic potential. [25] Cancerous cells are also found to have different viscoelastic properties than their non-cancerous counterparts (Fig. 1.3). [26]

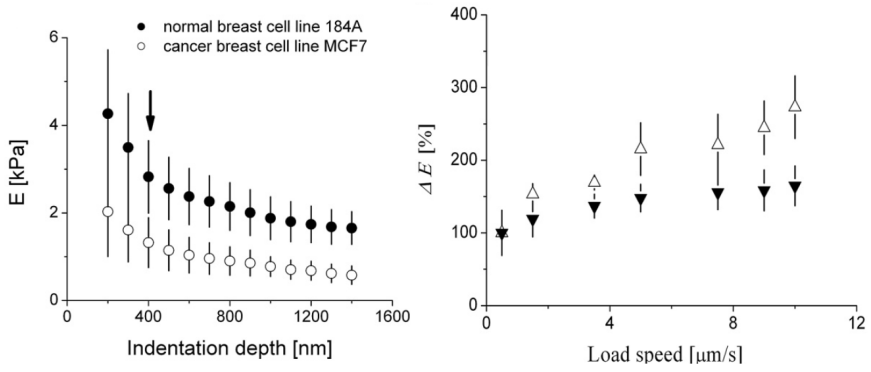

Figure 1.3: Young's modulus of cancerous cells compared to normal cells for different indentation depths and loading speeds. Cancerous cells were found to have a lower stiffness that is less dependent on loading speed compared to normal cells. Taken from [26].

Red blood cell flow

The rheological properties of red blood cells in the venous network depend on both their mechanical deformability and their interaction with the venous walls. [27, 28] The mechanical properties of red blood cells are investigated using a broad range of techniques, [29, 30] which led to findings such as the loss of reversible deformability as a function of cell age. [31]

More recently it was found using biomimetic systems that elastohydrodynamic interactions between red blood cells and the glycocalyx, a brush like structure that lines the walls of veins, play an important rheological role. In microcapilaries the glycocalyx influences both the flow resistance and regulates the adhesion of red blood cells, leukocytes and platelets to the vessel wall (Fig. 1.4). [32, 33]

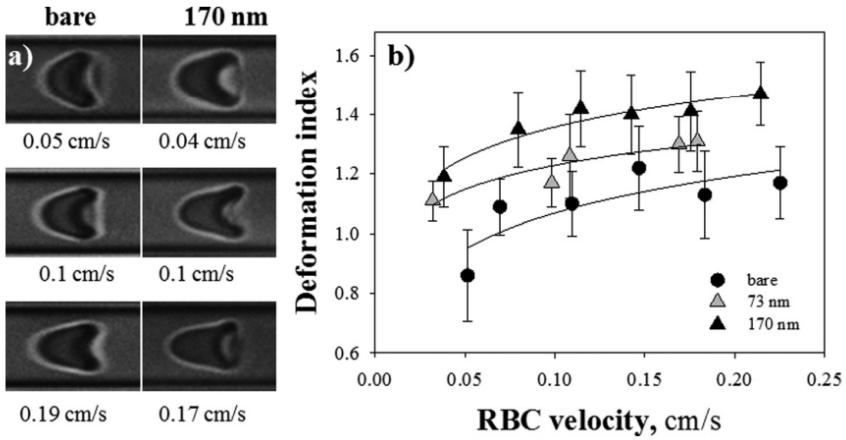

Figure 1.4: Change in red blood cell deformation induced by coating the microcapilary walls with polymer brushes. Taken from [32].

A commonality in all these examples is the requirement to quantify mechanical interactions below the micron scale, be it of the substrate or the cellular material itself. Patterned materials require local confirmation of the mechanical properties below the size of the pattern, while cells interact with their environment on a microscopic length scale. The cells themselves are heterogeneous and mapping their mechanical structure likewise requires sub micrometric resolution.

As we will shortly see, the mechanics at play when measuring the stiffness of soft materials at the macroscopic and sub micrometric scale are categorically different due to surface energy contributions. Values found at one length scale cannot be applied to another.

1.2 Indentation measurements

The conventional method to determine surface elasticity consists of indenting the surface with a probe of known geometry. The measured indentation as a function of applied normal force is interpreted through the application of a contact mechanical model, which allows extraction of the elastic modulus. The first model of this kind was developed by Hertz who considered the indentation of two fully elastic isotropic materials. [34] For the geometry of a sphere indenting

an infinite half plane this provides the relation

$$F = \frac{4}{3}\sqrt{R}E^*\delta^{\frac{3}{2}} \tag{1.1}$$

where F is the measured force response, R the sphere radius, E^* the reduced elastic modulus and δ the indentation. The elastic modulus of the surface of interest is extracted from E^* through

$$\frac{1}{E^*} = \frac{(1-\nu_s^2)}{E_s} + \frac{(1-\nu_i^2)}{E_i} \tag{1.2}$$

where $\nu_{s,i}$ and $E_{s,i}$ are the Poission ratio and elastic modulus of the surface and indenter respectively. Note for a perfectly rigid indenter this reduces to $E^* = E_s/(1-\nu_s^2)$.

Further additions to this model were made by Derjaguin-Muller-Toporov (DMT), who included attractive surface interactions outside the contact area, and Johnson-Kendall-Roberts (JKR), who included the surface energy inside the contact area to model adhesion between surface and indenters. [35, 36]

For soft solids the JKR contact model is generally the most applicable. When including the energetic loss due to surface energy, the JKR model makes the following corrections for a sphere indenting an infinite half plane

$$F = F_{Hertz} - 4\sqrt{\frac{E^*F_{det}a^3}{3R}} \tag{1.3}$$

$$\delta = \frac{a^2}{R} - 2\sqrt{\frac{F_{det}a}{3E^*R}} \tag{1.4}$$

where F_{Hertz} is the Hertzian force response, a is the radius of contact and F_{det} is the measured detachment force upon withdrawal of the indenter.

1.3 Soft matter elasticity at small length scales

While the JKR model includes the surface energy within the area of contact, it assumes this energy to be small compared to the elastic energy stored in the material. This assumption is not always valid when dealing with soft materials and small length scales. [37]

We can illustrate this with some energy considerations. As elasticity is a property of volume and adhesion a surface property, the corresponding energies during indentation with a rigid probe scale as

$$U_E \propto E \cdot a^3 \tag{1.5}$$

$$U_\gamma \propto \gamma \cdot a^2 \tag{1.6}$$

where U_E and U_γ are the energies associated with the elastic and adhesive components of the indentation, a is the length scale of the interaction, E the elastic modulus and γ the surface energy. Comparing the ratio of these energies we can define the elasto-capillary length as

$$l_c = 2\frac{\gamma}{E} \tag{1.7}$$

which gives us the length scale of interaction under which the surface energy in the interaction dominate the elastic energy. Setting a value of $\gamma = 0.1$ J/m^2 we can estimate this length scale as a function of material elasticity (Fig.1.5). This value is comparable to the surface energy

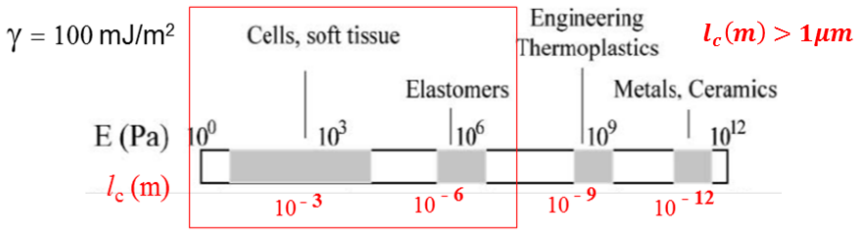

Figure 1.5: Elasto-capillary length (l_c) as a function of elastic modulus for a surface energy of $\gamma = 100$ mJ/m^2. The red box indicates the stiffness range for which l_c is below a micron. Adjusted from [37]

associated with cells and microorganisms in aqueous solutions, which is found to be on the order of $\gamma = 0.05$ J/m^2. [38, 39]

From these considerations it is clear that for materials softer than 1 MPa at length scales below 1 µm the interaction will be dominated by the surface energy. Under such conditions the material response deviates from the JKR model, as has been confirmed in experiments. [40–43] In particular this creates difficulties for the case of soft thin films, where contributions from the substrate preclude the use of macroscopic probes, but surface effects prevent qualitative interpretation for smaller probes. [44–48]

Developing improved contact models that fully account for these surface energy contributions is an active field or research. [49–51] Additionally experimental methods have been developed which solve the problem in a different fashion: measuring the elastic modulus of a soft surface without solid-solid contact.

1.4 Non-contact measurements of elasticity

A non-contact method for determining the elastic modulus of a soft surface in liquid was developed and demonstrated on the Surface Force Apparatus (SFA). [52] It functions by bringing a millimetric spherical probe within a nanometric distance from the soft surface. (Fig. 1.6) A nanoscale flow is generated between probe and surface by applying an oscillation of nanometric amplitude at a frequency of interest. With each oscillation the liquid is forced to drain in and out of the gap between the probe and the surface.

By measuring the amplitude and phase of the probe oscillation in reference to the excitation signal, the complex amplitude of the hydrodynamic force $\tilde{F}_\omega$ acting on the probe can be determined. [53] This allows us to define the mechanical impedance $\mathcal{Z}$ of the probe-surface interaction

$$\mathcal{Z} = Z' + iZ'' = \frac{\tilde{F}_\omega}{h_0} \tag{1.8}$$

where h_0 is the amplitude of the oscillation. In this equation the real component Z' represent the motion in phase with the driving force and is associated with the elastic energy stored in the interaction. The imaginary component Z'' represents the motion that is out out of phase and is associated with the energy dissipated in the interaction.

The accurate determination of $\mathcal{Z}$ is key to the measurement. By determining the variation of this parameter as the probe approaches the surface we can determine how the interaction varies as a function of probe sample separation.

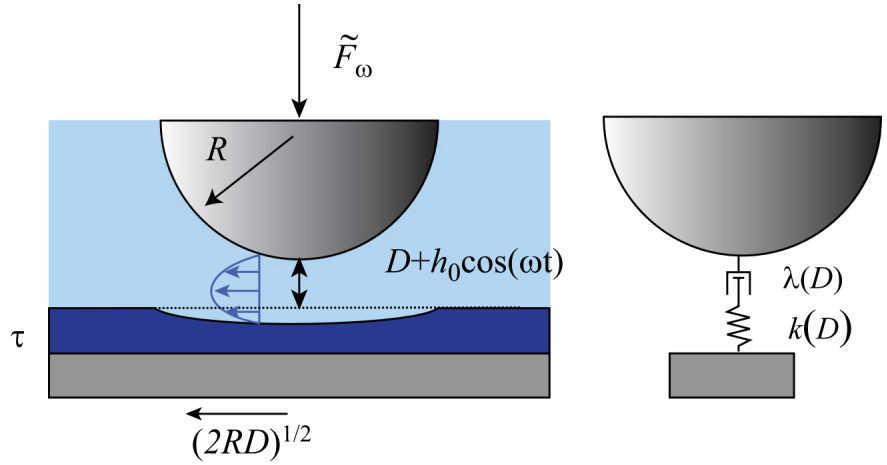

Figure 1.6: Overview of the non-contact measuring technique. An oscillating driving force $\tilde{F}_\omega$ is applied to a spherical probe close to the soft material surface. With each oscillation liquid is forced in and out of the gap between probe and surface. If sufficiently close this flow causes indentation of the soft sample surface. These interaction components can be modeled as a spring and dashpot system. Taken from [54].

At large distances the force exerted by this nanoscale flow on the surface is small and the surface can be approximated to be rigid. Assuming no slip of the liquid on the surface boundary, the only interaction between the probe and surface is the increase of dissipated energy due to confinement of the liquid, the Reynolds dissipative force, which is described by

$$Z''(z) = \frac{6\pi\eta\omega R^2}{z} \tag{1.9}$$

where η is de viscosity of the liquid, ω the angular frequency of the excitation, R the radius of the probe and z the distance from the surface. These large separations where such a purely dissipative response is found is named the viscous regime.

The force exerted by the flow will increase as the probe approaches the surface and when the probe is sufficiently close, the applied force becomes large enough to induce elastic deformation. This introduces an elastic component to the interaction that can be described by a $z^{-5/2}$ power law.

Closer to the surface the two components of $\mathcal{Z}$ become the same order of magnitude and their values saturate (Fig. 1.7). We transition from the viscous regime into the elastic regime, where the liquid is confined to such a degree that it is no longer expelled and the oscillation amplitude h_0 is mostly transferred into the elasticity of the surface.

The total response of the system can be described by a single expression

$$\mathcal{Z}_\omega(z) = \frac{6\pi\eta\omega R^2}{z_k} \cdot g_k\left(\frac{z}{z_k}\right) \tag{1.10}$$

where z_k is the distance at which we transition between regimes, which for a semi-infinite elastic surface is determined as

$$z_k = 8R\left(\frac{\eta\omega}{E^*}\right)^{2/3} \tag{1.11}$$

which depends on the elastic modulus of the surface. The analytical derivation of this equation and the precise form of the function g_k can be found in [54].

By measuring $\mathcal{Z}_\omega(z)$ and fitting equation (1.10) we can determine z_k and thus E^*. The effectiveness of this technique has previously been demonstrated on reticulated PDMS using the SFA. [52] Due to the absence of solid-solid contact the measurement is unaffected by surface energy contributions that dominating at small length scales and an absolute value for the elastic modulus is found.

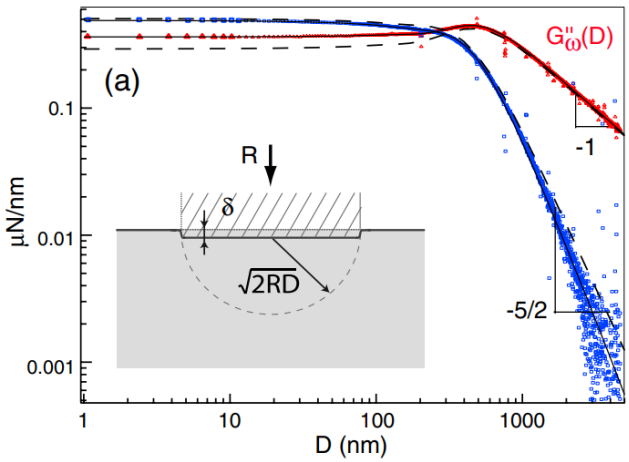

Figure 1.7: The elastic (blue) and dissipative (red) components of $\mathcal{Z}$ as a function of probe-sample separation. Measured using a SFA on a reticulated PDMS surface with $E \approx 2$MPa. In the viscous regime the dissipative component scales as z^{-1} due to the Reynolds visous damping, while the elastic component follows a $z^{-5/2}$ power law. Close to the surface both components become the same order of magnitude and saturate. Taken from [52].

Use of the SFA has some experimental limitations. The millimetric probe prevents measuring at the microscale. Likewise the highest available frequency is on the order of a few hundred hertz, which precludes the investigation of viscoelastic materials at higher frequencies. It would thus be of interest to apply the concept of this non-contact measurement on a platform that allows the use different length and time scales.

1.5 Atomic force microscopy

This manuscript presents our work towards implementation on the Atomic Force Microscope (AFM) to bring the non-contact measuring technique beyond the limitations of the SFA. Due to the use of a miniaturized force sensor in AFM, probe radii as small as 20 µm and excitation frequencies exceeding 500 kHz can be reached. When used in conjunction with the SFA this paves the way for the investigation of elastic properties across a large range of time and length scales.

A non-contact measurement in liquid using AFM provides its own set of experimental challenges. In contrast to the SFA, the force sensor of the AFM is submerged when measuring in liquid, which reduces sensitivity due to the increase in dissipation. Furthermore, when using traditional piezo-electric excitation in liquid the transfer function can be plagued by a 'forest-of-peaks'; Parasitic resonances within the system that obscure the lever response. [55,56]

This precludes the use of piezo-acoustic excitation and an alternative has to be found. In this manuscript we present the implementation of capacitive excitation in liquid, where electrostatic coupling imposes an excitation force between probe and surface.

In this manuscript it is assumed that the reader is reasonably familiar with the AFM technique. Should the reader not yet be sufficiently familiar with these concepts they are referred to the ample excellent literature available. [57–65]

1.6 AFM on real systems - polymer brushes and quick clay

In addition to the main subject of realizing a non-contact measurement of mechanical properties on the AFM platform, we present exploratory investigations into two complex material systems. The materials investigated using conventional AFM techniques are often relatively artificial. In such cases the complexity of the surface is minimized to ease quantitative interpretation of the data. Materials are made homogenous and surface roughness minimized to remain as close to the analytical models as possible.

We present experimental data on two materials, P-NIPAM polymer brushes and quick clay, in which we break with the application of conventional contact mechanics. We show that AFM can nevertheless be used to extract valuable information from these materials. As these two investigations are somewhat removed from the main topic of the manuscript, an introduction into either subject will be given at the start of their respective chapters.

Chapter 2

The homemade AFM system

Contents

2.1 Introduction

As a precursor to the work in this manuscript the non-contact measurement was attempted using a commercial AFM tool. Piezoacoustic excitation in liquid combined with optical beam deflection proved to be insufficiently reliable to determine the mechanical impedance $\mathcal{Z}(z)$ of the probe-sample interaction at frequencies other than the resonance frequency of the lever.

To illustrate the problem, we can consider the AFM as a single mode harmonic oscillator. For the measurement to be performed properly, the amplitude and phase response of this oscillating system as it varies with frequency, named 'the transfer function', needs to be clearly measurable over a broad range of frequencies around the resonance.

When using piezo-acoustic excitation in liquid where dissipation is high, parasitic resonances from other components of the AFM excited by the piezo-electric element distort the transfer function (Fig. 2.1). This is sometimes referred to as a 'forest of peaks', in reference to the many resonance peaks that can appear. Due to this distortion of the transfer function it is not possible to qualitatively perform the non-contact measuring method, as will be further illustrated in the appendix of chapter 4.

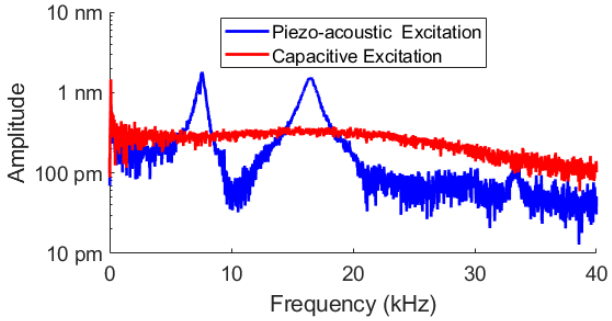

Figure 2.1: Comparison of piezo-acoustic and capacitive excitation of an AFM cantilever in liquid. Capacitive excitation provides a 'clean' resonance, while when using piezo-acoustic excitation the lever response is obscured by parasitic peaks around 8 and 15 kHz.

A different method of excitation in liquid is required that provides the proper excitation at each frequency; a 'clean' transfer function. The goal remains to use a commercial setup to make the technique available to a broad scientific audience, making it important to use a method of excitation that requires minimal modification of hardware. For this reason we propose capacitive excitation as an alternative. The colloidal probe and substrate can be made conductive, creating a sphere-plane capacitive system. By applying an alternating potential difference between these two electrodes an oscillatory force can be applied on the probe.

Combining capacitive excitation and the quantification of the interaction impedance is new in the field of AFM. The capacitance of the sphere-plane system varies with separation and the excitation force along with it, which is a difficulty that has to be faced. Resolving this and other practical difficulties requires an AFM system on which all relevant parameters are fully controlled and which can easily be modified to explore and develop this new experimental methodology.

Commercial devices do not lend themselves well for such purposes. Limited hardware modifications can be made and it is difficult to perform measurements outside of the 'modes' predefined in the control software. Commercial AFM systems have proprietary components to improve operation of the device, but of which the precise functioning is not public. Such components

make it difficult to precisely quantify the experiment.

For these reasons we chose to develop capacitive excitation in liquid on a homemade AFM system. It gives us full control of all parameters, providing the freedom to explore different implementations of the capacitive excitation technique. Instead of optical beam deflection method commonly using in commercial devices, the homemade AFM uses an interferometric measurement of the lever motion. This has the advantage of directly measuring probe displacement regardless of movement of the lever base.

The previous iteration of the homemade AFM, though in principle capable of performing the measurement, was not ideal for these purposes. The components used were fragile and expensive to repair, while exchanging or modifying them was not easy. We created a cheaper and robuster design that is easier to modify and manipulate: an ideal platform for experimenting with measuring methods.

In this chapter, we will shortly summarize the relevant AFM components and what is required for a capacitively excited non-contact measurement. After this we will specify which solutions were used to meet these requirements.

Figure 2.5 provides a broad view on the design, while an overview of the requirements, specifications and our solutions can be found in table 2.1.

2.2 Components of an AFM

An AFM system consists of multiple components working in unison to perform a measurement. These components and their function will be summarized to provide context to the design choices made for the new homemade AFM system. We will highlight specific difficulties that arise for each component when performing AFM measurements in liquid.

2.2.1 The force sensor

The core of an AFM is the force sensor, a micrometric lever that allows us to investigate the interaction force profile with a surface of interest. By measuring its deflection we determine the total force acting upon the beam in the $\hat{z}$ direction. The sensitivity of this measurement is determined by the stiffness of the lever (k_c , usually in the range of 0.001 - 10 N/m) and the accuracy with which we detect its motion. The most commonly used detection methods are two optical techniques.

Optical beam deflection

In Optical Beam Deflection (OBD) a laser beam is reflected on the backside of the lever and captured by a four quadrant photodiode (Fig. 2.2a). When an applied force deflects the lever we track this deflection through the change in position of the laser on the photodiode. The advantage of this technique is the ease of alignment, as the laser spot can be aligned at the end of the lever using rotating mirrors. [66] For this reason the technique is commonly used in commercial AFM designs.

The sensitivity of the photodiode needs to be calibrated to an external standard. The position of the laser on the photodiode does not directly represent the positional motion of the lever, but its angular deflection; the difference between base and end position of the lever. If the lever base moves significantly these are not the same which poses a problem for piezoacoustic excitation in liquid where large base motion is required to provide sufficient excitation. While partial solutions to such problems exist, they were found to be insufficiently reliable as will be illustrated in the appendix of chapter 4. The different optical index of the used liquid will

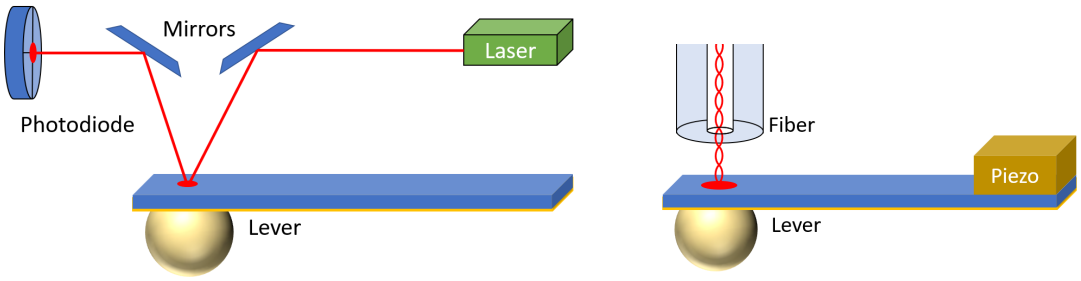

(a) (b)

Figure 2.2: (a) Schematic representation of the Optical Beam Deflection setup. A low power laser is reflected on the back of the AFM lever onto a photodiode. Two bi-axial rotating mirrors are used for alignment. (b) Schematic representation of interferometric detection using an optical fiber. The fiber is positioned above the end of the lever, with a piezoelectric element keeping lever-fiber distance constant through a feedback loop.

also affect the optical path of the laser beam, though this can usually be corrected through the rotating mirrors.

Optical fiber interferometer

A second method for detection of the lever motion is an interferometric measurement using an optical fiber (Fig. 2.2b). A low power laser beam is injected into an optical fiber of which the end is positioned above the lever. A small part of the laser reflects at the fiber end, while the majority reflects on the back of the lever, creating an interferometric cavity. [67] A feedback loop is used to displace a piezo at the base of the lever to keep the probe-fiber separation constant, allowing the deflection of the beam to be determined from the piezo movement. [68]

This detection method directly measures the displacement of the lever independently of movement of the base. Calibration is done internally by relating the detected displacement to the wavelength of the laser. The price to pay is that the fiber must be aligned in three dimensions; both at the end of the lever and at the right distance. The fiber end must be sufficiently flat, which is achieved by cleaving the fiber using a specialized fiber cutter. Due to contamination the smoothness of the surface deteriorates over time and the fiber must be recleaved periodically, slowly consuming the fiber material.

2.2.2 Displacement and alignment

Detection of the lever motion provides access to the total force acting upon the probe, the variance of which we want to measure as a function of the separation between the probe and the surface of interest. This probe must be put in a specific position and kept there for the duration of each measuring point.

Course alignment

Alignment of the lever and detector must be sufficiently stable and accurate so as to not influence the measurement. This is usually referred to as 'course' alignment as it requires only micro metric accuracy. A first approach of the sample to within microns of the probe is also included

in this category. Many methods of displacement are suitable for this, though most commonly used are (motorized) micrometric screws and 'stick-slip' piezo actuated stepper motors. [69]

Fine alignment

The required level of positional control between probe and sample, or fine alignment, is determined by the length scale of the investigated interaction force and the size of the probe. Measuring short ranged forces with sharp probes requires sub nanometric positional control, while control on the scale of some 10 nm may suffice for micrometric probes and longer ranged interactions.

In most cases fine alignment is achieved through piezoelectric elements. [70] The extension of these elements is continuous, thus accuracy is determined by the applied voltage. The extension does have a finite response time and is not completely linear, requiring calibration before the experiment.

The performance of piezoelectric elements does not significantly deteriorate when performing measurements in liquid, as the mass of the added liquid is usually small compared to the load capacity of the piezos. Care should be taken that the piezos are well protected from spillage of the liquid.

Stability

If components move while integrating an observable for a measuring point, the data will be averaged over this displacement. On short timescales, vibrations originating from outside the setup can displace components. Passive isolation can stop these vibrations from entering the setup, such as placing the AFM on a heavy platform suspended on springs, which damps oscillations above a few hertz due to the inertia. Active isolation can also be used, in which the noise is measured and compensated.

On longer timescales components drift out of position. Different components are not necessarily at full thermal equilibrium and expand unevenly due to thermal expansion. By isolating the AFM from the environment using an insulated box and allowing it to internally equilibrate before each measuring session these drifts are pushed to timescales longer than the experiment. This has the added advantage of preventing acoustic vibrations from affecting the measurement.

2.2.3 Probe-sample interaction

The scaling of the interaction strength depends on both the interaction investigated and the geometry of probe and sample. In most applications the sample is locally approximated as an infinite half space, while on the probe side there are multiple geometries that can be fabricated.

The length scale of interest

It should be emphasized that one of the powers of AFM is the ability to investigate a material over a broad range of length scales. From 100 µm radius colloidal probes [71], to a radius of curvature of some nanometers for sharp probes [72] the interaction with a surface can be investigated over 5 orders of magnitude. While this ability is not fully utilized in our implementation of the non-contact measuring method in liquid, it will play an important part in the investigation of clay materials in chapter 7.

Sharp probes

For most experiments levers with sharp probes are used, most commonly with pyramidal or conical geometry. The lateral resolution achievable with such probes is set by the final radius of curvature, which can be below 10 nm. Sharp probes are important in imaging techniques for this reason. This high lateral resolution comes at the cost of decreased sensitivity as the force profile is integrated over a smaller volume.

Colloidal probes

It is difficult to fabricate sharp probes that fulfill the analytical description of their geometry. Near-perfect spheres of glass can however be fabricated with relative ease by utilizing surface tension. [73] Some care should be taken as not all commercially available spheres are equally smooth. [74] The radius of the sphere sets both the lateral resolution and the interaction strength. In principle smooth spheres with a radius below 10 µm can be fabricated, but should the size of the probe be comparable to the range of the investigated force, the lever will not be sufficiently far away from surface and its contributions to the measured force profile cannot be approximated to be 0.

2.2.4 Dynamic AFM

The harmonic oscillator properties of the AFM lever can be used to perform a more sensitive AFM measurement. By tracking shifts in the resonance frequency it possible to measure the force gradient acting on the lever, while tracking the quality factor gives access to the dissipated energy. [75–77] The resonance of the lever acts as an amplifier, increasing sensitivity by roughly the quality factor.

While large amplitudes are commonly used to create topography maps, [60] small amplitudes allow for linearization of the local force profile. [78–81] This allows variations in the force gradient and dissipated energy to be determined through the amplitude and phase signal, even off resonance, as will be explained in chapter 3.

The high dissipation in liquid significantly decreases the quality factor thus lowering the sensitivity. This however has the advantage of spreading out the resonant response of the lever over a broader frequency range which allows for the investigation of a surface over a broader range of frequencies using a singe probe, as will be demonstrated in chapter 4. [82]

2.2.5 Excitation methods

To perform dynamic AFM measurements, one would ideally have a method of excitation that is reliable, provides a clean transfer function and excites the probe directly. Multiple excitation techniques have been developed but none is perfect for every application. To better appreciate our choice for capacitive actuation in liquid we will shortly review the varying excitation methods.

Piezo acoustic

The most commonly used excitation method is piezoacoustic, where a piezoelectric element supplied with an oscillating voltage signal shakes the base of the lever (Fig 2.3a). [83, 84] As a technique it is simple to implement, works for any probe and in principle works in liquid. [85–87]

For certain applications it is not ideal as excitation is not contained to the lever but affects any nearby resonant component. [87] While in air it is possible to distinguish between these

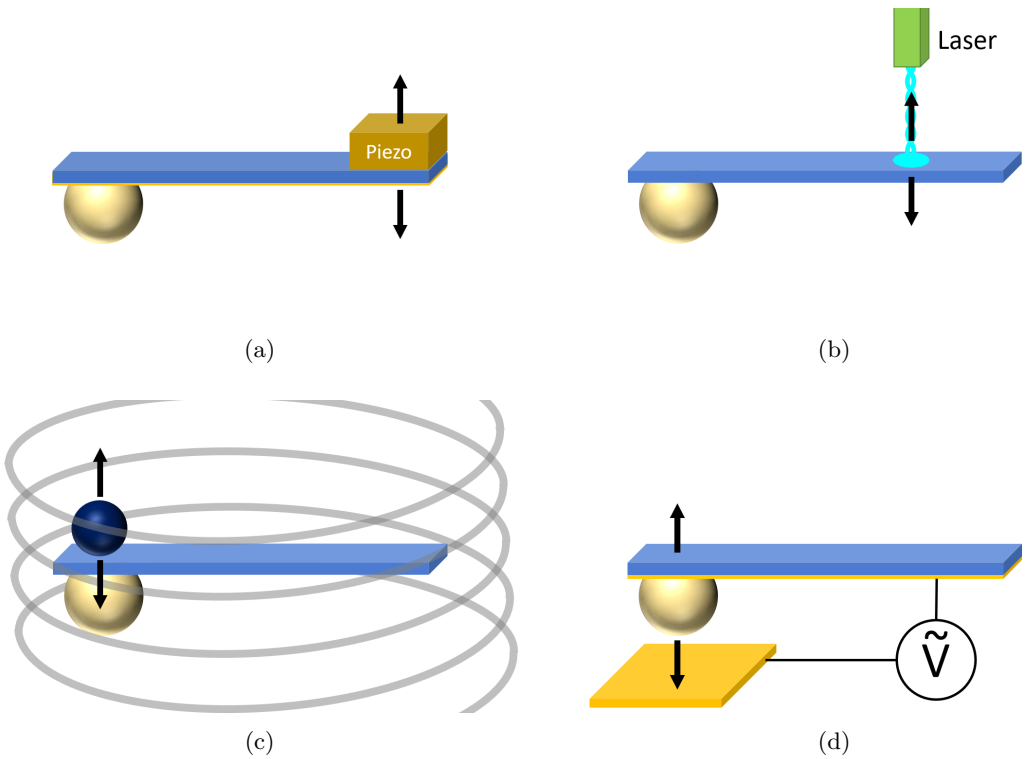

Figure 2.3: Schematic overview for (a) piezoacoustic, (b) photothermal, (c) magnetic and (d) capacitive excitation. Black arrows indicate the position at which the excitation force is applied, which for (a) and (b) is at the base of the lever and for (c) and (d) is directly at the probe.

different responses, in liquid these 'parasitic' resonances often obscure the lever response as they are 'spread out' over a broad frequency range due to the high dissipation. [55, 56] The motion of the piezo also generates acoustic waves in the liquid that create an additional excitation force. [88] While various methods were developed to reduce such effects, at the time of writing no complete solution exists. [89–92]

As will be demonstrated in the appendix to chapter 4, the combination of optical beam deflection and piezoacoustic excitation in liquid did not provide the needed stability and spectral purity required for the non-contact measuring method.

Photothermal

The AFM lever can be excited by heating the base of the lever with a pulsed high power laser (Fig. 2.3b). The absorbed heat induces local thermal expansion, creating a bending moment as the lever asymmetrically absorbs heat. [93] This allows for excitation in liquid without exciting other components. [94–96]

Implementation of photothermal excitation is relatively complex, requiring a second optical setup for the excitation laser. The position of the excitation laser spot must be well chosen to guarantee the response of the lever is harmonic. [97] While the spectral response in liquid is better than piezoacoustic excitation, it is not perfect, especially off resonance. [98]

While photothermal excitation would be an improvement to piezoacoustic with regards to our application, it is difficult to implement. As of writing, there is a single commercial AFM on the market with photothermal excitation capability, the 'blueDrive' made by Oxford Instruments for their 'Cypher' line of AFMs. [99] The high cost of this equipment combined with the non analytic excitation spectrum was sufficient reason not to pursue this technique.

Magnetic

Excitation of the lever through an oscillating magnetic field is another option (Fig. 2.3c). [100] External coils create an oscillating magnetic field that drives the lever, which has been demonstrated to work in liquid. [55] The excitation force is given by

$$\vec{F} = -\nabla\vec{E} = -\nabla(\vec{m}\cdot\vec{B}) \tag{2.1}$$

where m is the magnetic moment of he lever and B the applied field.

As commercial AFM levers have no magnetic moment a magnetic particle must be added. Adding such a large particle distorts the eigenmodes of the lever motion and the optimal position on the backside of the lever end directly impedes with optical detection techniques. [101] While magnetic excitation does provide a near analytic transfer function, the excitation strength is limited even for large particle sizes. [102] For these reasons it is not suited for our current application.

Capacitive

Lastly the probe can be excited by making the AFM lever an electrode in a capacitive system. A force can be applied by controlling the potential difference between the two electrodes (Fig. 2.3d), the strength of which is given by

$$F = -\frac{1}{2}\frac{dC}{dz}V^2 \tag{2.2}$$

where V is the potential difference and C the capacitance of the system. [103,104] Excitation in liquid is possible, though the dielectric constant of the medium has to be taken into account. If the probe is used as an electrode, capacitive excitation provides a transfer function that is close to analytical. [98] Faraday effects need to be avoided by using non-polar, non-disassociating liquids, though capacitive actuation has also been demonstrated in pure water. [98]

The implementation of capacitive excitation requires minimal hardware modifications on most commercial AFM systems. Due to ease of implementation and clean transfer function it was implemented by using the probe-substrate system as a sphere-plane capacitor. For such a geometry $\frac{dC}{dz} \propto \frac{1}{d}$ where d is the distance of separation. [105] The dependency of the excitation strength on probe-sample separation will need to be faced during data analysis, as will be further explained in chapter 3.

2.3 Design specifications

With a clear overview of the components critical to AFM operation in mind, we can determine which specifications are imposed on the setup by the non-contact determination of mechanical properties in liquid. An overview of these of specifications can be found in table 2.1.

The goal is to measure the distance at which the transition in the mechanical impedance $\mathcal{Z}$ takes place due to the confinement of liquid between the probe and sample, and the buckling of the sample material under the applied oscillating pressure. As discussed in chapter 1 this occurs at a distance of

$$D_k = 8R\left(\frac{\eta\omega}{E^*}\right)^{\frac{3}{2}} \tag{2.3}$$

which for micrometric probes, MPa stiffness materials and excitation frequencies in the range of kHz is on the order of 0.5µm. A measuring range of 0.1-1 µm is required for demonstrating the technique with nanometric control of fine alignment. For stiffer and softer materials the radius of the probe provides a controlled parameter to keep the transition on a measurable length scale.

As lever deflection contributes to tip-sample separation, it should equally be measured or compensated at nanometric accuracy.

A clean transfer function is crucial and thus should be measured with sufficient accuracy. The sub nanometric amplitude required for linearization of the force profile sets the sensitivity required of the setup. A 50 pm amplitude signal should be measurable in the time span of 100 ms, requiring a noise floor of 250 pm^2/Hz. Such a sensitivity is commonly achieved with both optical beam deflection and interferometric detection methods.

To evaluate the timescale of the measurement, a 5 µm measuring range with 1 data point at each nanometer of displacement measured at 10 Hz makes the measurement take just under 10 minutes. Drift within this time frame should not significantly affect the measurement, thus be no worse then 1 nm/min for a max shift of 10 nm per measured curve.

2.4 Possible solutions

To fulfill the demands of the non-contact measurement in liquid as set in the previous section, three possible avenues of approach were considered.

2.4.1 Capacitive actuation on a commercial setup

One of the main arguments for incorporating capacitive excitation is the ease of implementation on a commercial setup. The only modification required is an electrical connection between the probe and sample, which most commercial AFMs accommodate due to applications such as kelvin probe microscopy (KPM). [106, 107] The sensitivity and spatial control indicated in the preceding chapter are within specifications for most modern commercial AFMs, with a possible exception in the required frequency range. Commercial AFMs are not always equipped to measure responses below 10 kHz, though in such cases a more suitable external lock-in can often be used.

It is clear that we need to complete our understanding of capacitive actuation combined with the non-contact measuring method in practice. Commercial setups do not provide the freedom required to do this, as it not possible to change hardware or perform measurements outside the measuring modes defined in the software and they do not provide direct access to the raw signal.

As a quick example, the calibration, approach and feedback protocols on the Bruker ICON AFM system are designed with amplitude modulation AFM in mind, which assumes the amplitude of oscillation to always decrease as a function of probe-sample separation. This is not true for the case of capacitive excitation, as the excitation force increases for smaller separations.

For this reason we decided to not directly attempt to implement the measuring technique on a commercial setup, but first explore its intricacies on the homemade setup. Once the technique has been fully mastered on this setup, we will be ready to face the implementation of the technique on a commercial setup.

2.4.2 The homemade setup

The biggest technical difference between the homemade setup and commercial setups is the use of optical fiber interferometry as the method of detection. It was previously used to investigate nanoscale radiative heat transfer, [108,109] nanoscale emmissivity, [110] and later the dynamics of a water nano-meniscus between a sharp probe and a surface. [97] Due to the short range of the forces involved, this required (sub)nanometric positional control and in the case of radiative heat transfer, thermal isolation and operation under vacuum.

To achieve this sub-nanometric precision in vacuum, 'Attocube' piezoelectric nanopositioners were used. Due to their vacuum compatibility, these nanopositioners are fragile, difficult to manipulate, and costly to repair and replace. All components were situated in a single metallic frame, making it difficult to add, modify or perform maintenance on components.

2.4.3 A redesigned homemade AFM

We thus decided to not use the setup "as-is" but to redesign it, with two goals in mind: Firstly to replace the expensive and fragile nanopositioners with alternatives that, though not vacuum compatible, perform sufficiently well, are cheaper, and more robust. Secondly to make the detector, lever and scanner individually removable components that allow for easy manipulation. This creates an AFM system that can be modified to meet the demands of the measurement at hand. The optical system and electronics of the setup were left unchanged.

Requirement	Specification	Solution	Section
Static deflection detection	<1nm accuracy	Optical fiber	2.5.1
Dynamic deflection detection	<50pm in 100 ms	Optical fiber	2.5.1
Course alignment	∼100 nm accuracy, >15 mm range	Stepper motors	2.5.3
Fine alignment, XY	∼1 nm accuracy, 100 µm range	Piezoelectric elements	2.5.3
Fine alignment, Z	∼1 nm accuracy, 10 µm range	Piezoelectric elements	2.5.3
Measurements	$F(d)$, $A(d,\omega)$, $\phi(d,\omega)$, Force Volume Mapping	SPM controller	2.5.4
Frequency decomposition	0.1-100 kHz range, 1-100 Hz Integration bandwidth	Lock-in amplifier	2.5.4
Vibrational Isolation		Passive isolation	2.5.5
Thermal Drift	<10 nm per measurement	-	2.5.5
Interaction	Analytically solvable, Interaction range >5 µm	Colloidal probes	2.8

Table 2.1: Overview of the requirements of the setup demanded by the non-contact determination of mechanical properties in liquid.

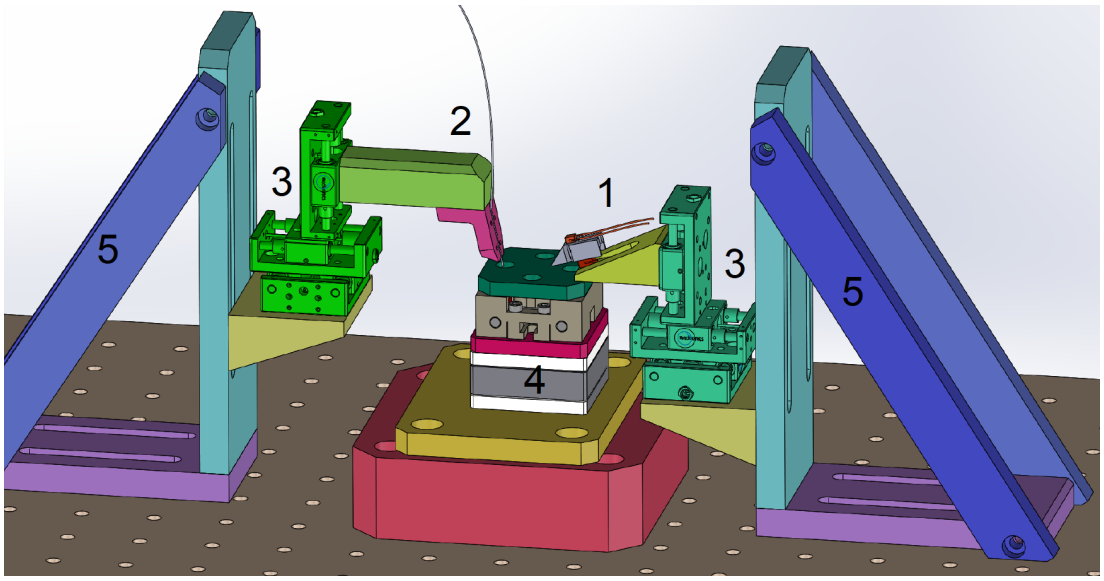

Figure 2.4: Schematic of the measuring setup. 1) Probe holder, 2) Fiber holder and fiber, 3) Course alignment motors, 4) Fine alignment scanner, 5) Aluminium frame.

2.5 Description of the homemade AFM

The redesigned homemade AFM roughly consists of three separate components: The fiber holder, probe holder and sample holder (Fig. 2.4). The fiber and probe holder are equipped with micropositioners for course alignment, while the sample has nanopositioners for fine alignment. For course alignment the sample is considered stationary and the probe and fiber are aligned correctly, while for fine alignment the fiber is considered stationary and the probe and sample are displaced.

The fiber holder clamps the fiber at a 15^o angle normal to the sample surface (Fig. 2.5 & 2.5). For course alignment it is connected to three MechOnics nanopositioners (one for each dimension) suspended above the breadboard by an aluminium frame.

The probe holder is connected to a second stack of three Mechonics nanopositioners suspended by an aluminium frame. A metal wedge correctly angles the probe holder orthogonal to the fiber (Fig. 2.5b). The probe is glued to the probe holder using silver glue, which doubly serves as an electrical connection. The holder is seated on a piezoelectric element for fine displacement in the $\hat{z}$ direction, designated as the 'W-piezo'. This piezo is used to keep the fiber-lever distance constant, as will be further explained in section 2.2.1. A small piezo dither is glued to the top of the probe holder for piezoelectric excitation, though the larger W-piezo can be used for this purpose as well.

The sample is displaced by two piezoelectric scanners: a PiezoJena PXY100 for movement in $\hat{x}\hat{y}$ and a PiezoJena PZ10 for movement in $\hat{z}$. They are connected to the breadboard using an aluminium block and covered with a plate for protection. Samples are glued onto aluminium disks and magnetically connected to the cover plate. For measurements involving liquid, a piece of cloth is used to protect the scanners from spillage.

The functioning and calibration off the individual components will now be discussed in detail.

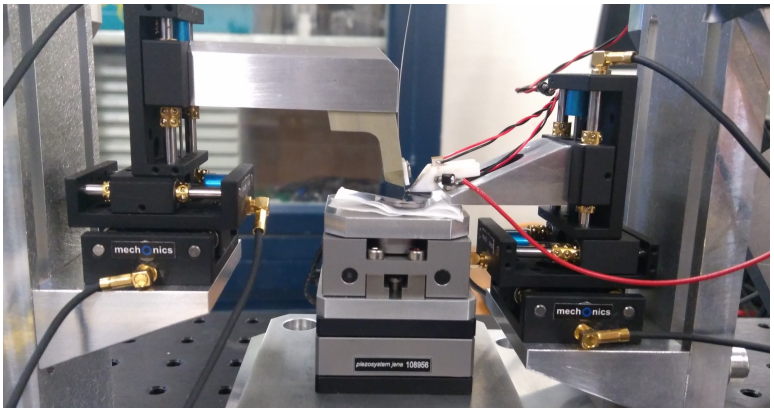

(a)

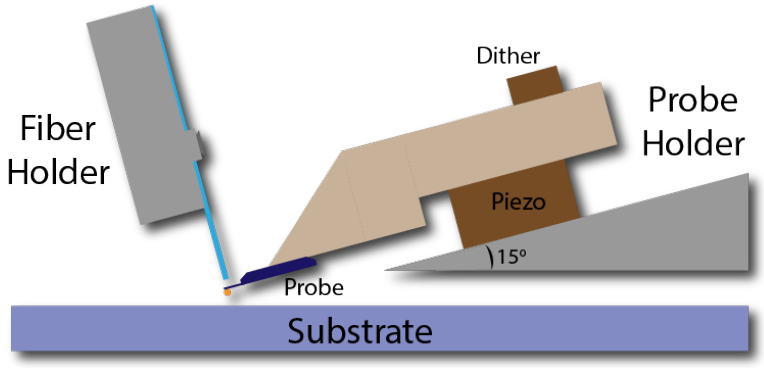

(b)

Figure 2.5: (a) The AFM setup. From left to right: The fiber holder, the sample holder and the tip holder. (b) Schematic overview of the heart of the measurement.

2.5.1 Optical fiber interferometer

The homemade AFM directly measures the lever position through interferometry using an optical fiber. It has comparable sensitivity to optical beam deflection [111] and works regardless of displacement of the lever base.

Interferometric measurement

A laser source creates a laser beam that is injected in an optical fiber positioned above the end of the AFM lever (Fig. 2.6). The fiber end is cleaved with a surface roughness below the wavelength of the laser and can be considered as a planar interface for optical reflection considerations. 4% of the beam is reflected back due to reflection coefficient of the silicon-oxide/air interface (S_1), while the majority of the beam is transmitted. [67]

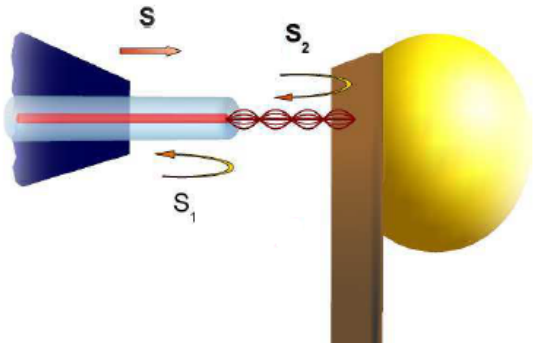

Figure 2.6: Schematic of the interferometric measurement. The laser beam is emitted from the fiber and in first order reflects on two surfaces creating two reflected beams: beam S_1 is reflected at the final interface of the fiber and beam S_2 is reflected on the back of the AFM lever. Both reenter the fiber where they create an Adjusted from [112].

The beam reflects a second time at the lever surface and in part reenters the optical fiber (S_2). The difference in the path length between beams S_1 and S_2 creates an interference pattern in the intensity profile of the beam traveling back through the fiber (Fig. 2.7), described by

$$I(d) = I_0 + \Delta I_0 \sin\left(\frac{4\pi}{\lambda} d + \phi\right) \tag{2.4}$$

where d is the lever-fiber separation and λ is the wavelength of the laser beam.

Sensitivity to changes in this intensity is highest where the slope is the largest, at the inflection points of the sinusoidal function where $I(d) = I_0$. Through expansion of the function at these points we find a first order sensitivity of

$$\frac{\delta I}{\delta d} = \frac{4\pi I_0}{\lambda} \tag{2.5}$$

If the fiber and lever are submerged in a liquid the difference in refractive index of the medium will change the effective wavelength of the laser light and rescale our interferometric perception of distance. This can be corrected through $\lambda' = \frac{\lambda}{n'}$, where n' is the ratio of the refractive index of the medium relative to that of air where $n \approx 1$.

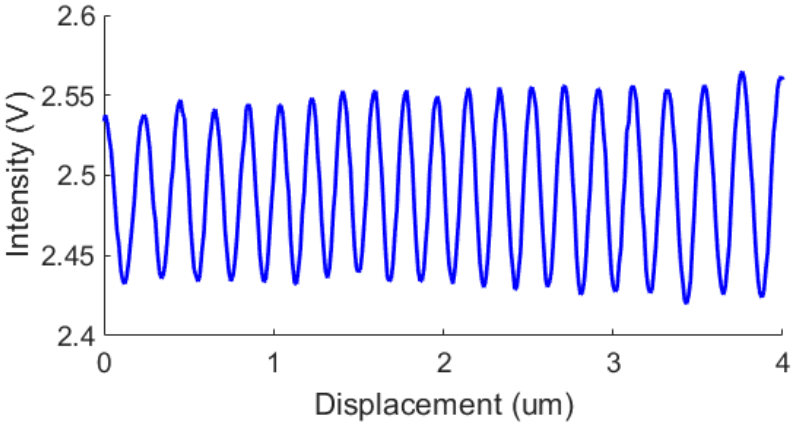

Figure 2.7: Measured intensity profile $I(d)$ as a function of decrease in probe-sample separation. The interference between the reflected beams S_1 and S_2 creates an oscillating profile with amplitude ΔI_0 on top of the baseline intensity I_0. The oscillation has a wavelength of half the wavelength of the laser, in this case 330 nm.

Distance control

Only measuring the instantaneous reflected intensity is insufficient to precisely determine position. The relative position in the oscillatory pattern is not known beforehand and the sensitivity varies strongly as a function of distance, reaching zero on the maxima of the interferometric pattern.

As a solution, a PI-controller actuating a piezo in the probe holder keeps the lever-fiber separation constant. [68] Any slowly varying deflection of the lever will be compensated and the lever deflection can be inferred from the piezo movement. The inflection points, where sensitivity is highest, are on first order asymmetric to a change in separation and are thus a suitable position to apply the control loop. The positional error of this loop is generally on the order of 200 pm in air and 500 pm in water, which is sufficient for our current purposes.

The feedback system however cannot distinguish between different branches of the interference pattern. If the lever moves a distance of $\frac{\lambda}{8}$ due to an uncompensated force for a period longer than the feedback time, the feedback will apply in the wrong direction and move to the next branch in the interference pattern. [113] It is not guaranteed that this new inflection point has the same sensitivity as was calibrated for the first.

2.5.2 Optical setup

The optical setup required for the interferometric measurement consists of a laser source, coupler, photodiode and amplifier (Fig. 2.8). Ideally one would inject the laser beam and measure the reflected beam on the same line but requires superimposing of the laser and detector. Instead the beam is split across two optical fibers through evanescent wave coupling. [114]

The injected beam R0 is split over fiber P0 leading to the lever, and a 'dummy' fiber P1. The beam in P0, after reflecting at the lever and fiber end, reenters the fiber and is again split over fibers R0, which leads back to the laser source, and R1, where it is detected by the photodiode.

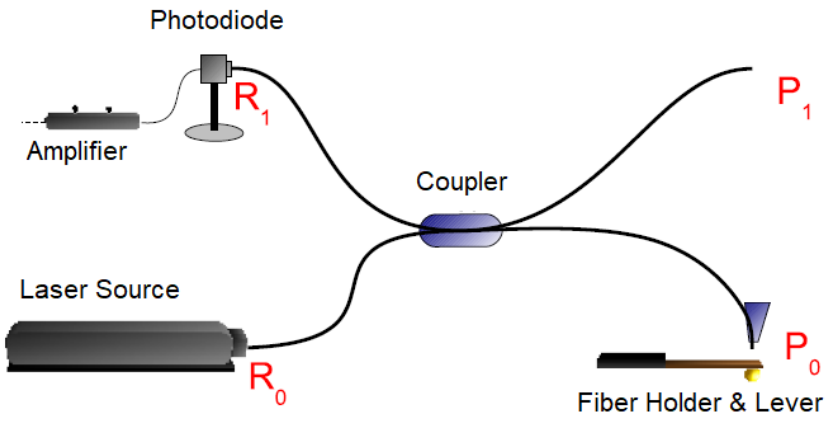

Figure 2.8: Overview of the optical setup used for the interferometric position measurement. The laser source inject a beam into fiber R_0, which is split equally by the coupler over fibers P_0 and P_1. The P_0 beam reflects of the lever, and reenters the fiber, where it is again split over R_0 and R_1. The beam at R_1 is converted into a current by the photodiode, which is subsequently turned into a voltage by the amplifier. Taken from [112].

Laser source

The laser source is a 51nanoFI made by Schäfter and Kirchhoff, a thermally stabilized diode laser. It is equipped with a M01 coded laser diode, which emits at a wavelength of 661 nm and has a maximum power of 5.4 mW. It is equipped with a Faraday Isolator which prevents reflected light reentering the source through the coupler. The beam profile has rotational symmetry and a Gaussian intensity distribution, while the power can be controlled through a potentiometer or an externally applied voltage.

Coupler

A 2 way beam splitter or 'coupler' is used to split the beam equally across the two fibers using evanescent wave coupling. It is made by Schäfter Kirchhoff and features 4 ports, allowing for use in both directions, as is required for the interferometric measurement.

Photodiode

A ThorLabs DET100A/M photo-diode measures the total incident intensity over a wavelength range of 350 to 1100 nm through a silicon based detector. It is used in photo-voltaic mode that generates a current from incident photons through the photo-voltaic effect. The peak response is 0.72 A/W at a wavelength of 970 nm.

Amplifier and converter

The roles of I/V converter and amplifier are fulfilled by a DPLCA-200 Femto amplifier (Fig. 2.9). The photo-generated current from the photo-diode is converted into a voltage for the Nanonis control system at gains of 10^5 or 10^6 V/A with corresponding frequency bandwidths of 500 and 200 kHz in the 'low-noise' operational mode.

Figure 2.9: DPLCA-200 Femto Amplifier.

2.5.3 Positional control

Course alignment

For course alignment of the fiber and probe two stacks of three MechOnics MS30 piezoelectric inertial motors is used, one per $\hat{x}$, $\hat{y}$ and $\hat{z}$ direction, each with a range of 30 mm. The motors work through the 'stick-slip' principle. Movement is performed in steps, where the applied voltage is first slowly ramped to extend a piezoelectric column carrying the platform: the 'stick' part. When sufficient extension is reached, the applied voltage is quickly removed, causing rapid contraction of the piezo. Due to the inertia difference between piezo and platform, the piezo 'slips' back while the platform remains stationary. To displace the platform this cycle is repeated at a high frequency.

For the MechOnics the smallest step size achievableis about 50 nm. Nanometric calibration of the positioners is not required as it is only used for rough alignment and are stationary during the measurement.

Fine alignment, lateral

A PiezoJena PXY100 was used to laterally displace the sample up to 100 µm. The piezoelectric response of this scanner is continuous, thus the resolution is limited by the precision of the voltage applied by the controller, marketed at 0.2 nm. It has a resonance frequency of about 400 Hz in both directions, which is sufficiently low response time for the measurements presented in this work.

The scanner is calibrated by imaging a NT-MDT TGX1 reference grid twice using AM-AFM, once with each lateral directions as the primary scanning axis (Fig. 2.10). The calibration factors were found to be 6.46 and 6.62 µm/V for the $\hat{x}$ and $\hat{y}$ directions respectively. Assuming a linear response this makes the effective scanning window 129.4 by 132.4 µm.

Fine alignment, vertical

For displacement of the sample in the $\hat{z}$ direction a PiezoJena PZ10 scanner is used. It features a 10 µm scanning range and a resonance frequency of 4 to 5 kHz depending on the applied load. As with the PXY100, the platform is piezo actuated and the resolution limit is determined by the controller, marketed at 20 pm.

Precise calibration of the PZ10 is important as it sets the probe-sample separation axis. Determining the height difference between planes in the TGX1 reference structure is insufficient, as it only provides two calibrated positions and cannot resolve non-linearity or hysteresis.

This can be resolved by interferometrically measuring the displacement of the scanner surface using the fiber. This technique was previously used to measure displacements up to 1 µm, where the measured profile is directly evaluated with equation (2.4) and a second order polynomial in d to account for nonlinearity. [97, 101, 112]

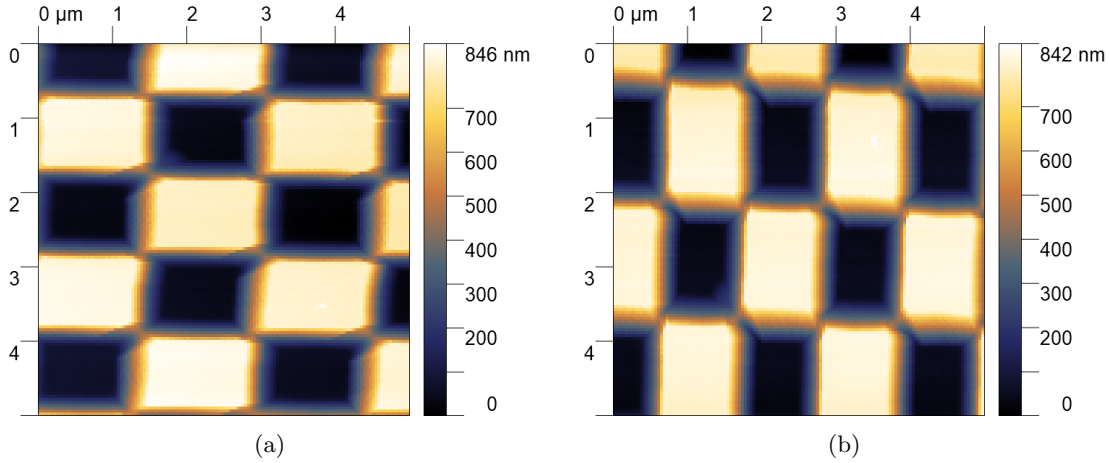

(a) (b)

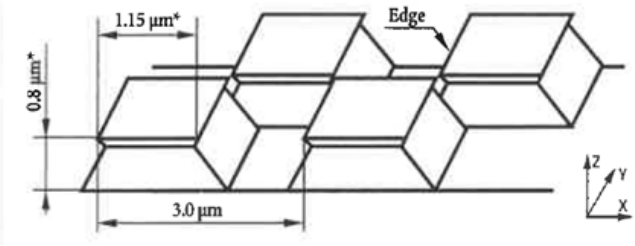

(c)

Figure 2.10: Calibration images for the PXY100 scanner in the (a) $\hat{x}$ direction and (b) $\hat{y}$ direction. The calibration factors were found to be 6.46 and 6.62 µm/V for the $\hat{x}$ and $\hat{y}$ directions respectively. (c) Specifications of the TGX1 reference structure as supplied by NT-MDT.

This procedure is unfeasible for the PZ10, as it is difficult to directly fit the variation in the wavelength of $I(d)$ caused by non-linearity of the scanner over its large range. As an alternative the reflected laser intensity $I(d)$ is measured over the entire scanner range. Taking the average $\langle I(d) \rangle \approx I_0$, we extracted

$$I(d) - \langle I(d) \rangle \approx \Delta I_0 \sin\left(\frac{\lambda}{4\pi} d + \phi\right) \tag{2.6}$$

Though not important for our current considerations, we can see that ΔI_0 varies with d (Fig. 2.11a). This is due to more reflected light reentering the fiber as the fiber-surface distance decreases.

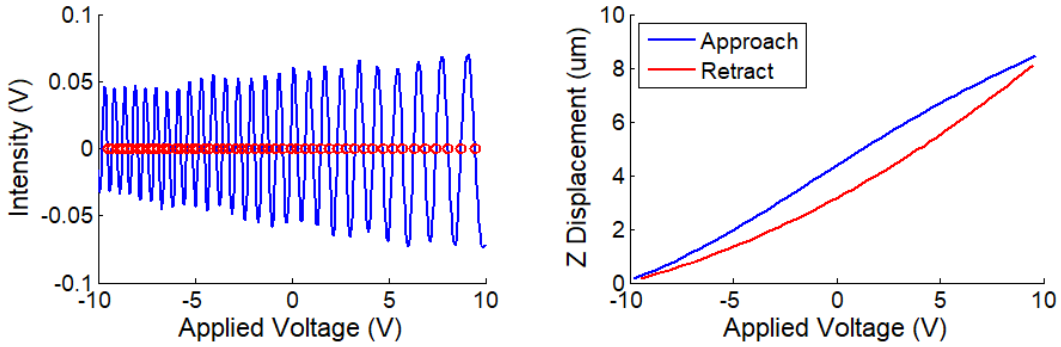

(a) (b)

Figure 2.11: (a) Variation of intensity as a function of voltage applied to PZ10 controller. Red circles indicate the zero crossings (b) Calibrated extension of the PZ10 scanner as a function voltage applied to the controller.

However, each full wavelength has two inflection points at the zero crossings, separated by a distance of $\frac{\lambda}{4} = 165$ nm. Assuming smooth piezo extension, we can reconstruct the displacement as a function of applied voltage (Fig. 2.11b). As the fiber is at a 15^o angle the found values must be corrected by $\cos(15^o) = 0.965$.

Probe holder piezo

Due to its smaller range of motion of 1 µm, the piezoelectric element under the probe holder can be calibrated by directly fitting the interference pattern to equation 2.4. This calibration is automatically performed by the Nanonis software. The sensitivity is determined through equation (2.5) which also sets the sensitivity for the lock-in.

2.5.4 SPM controller

A Nanonis SPM controller by Specs-Zurich drives the experiment. Its components are considered in three parts:

Realtime control system and signal conditioning 4

The Realtime Control System (RCS) performs realtime signal analysis and is the interface between the Nanonis control software and the experiment. It uses a National Instruments

7965R FPGA card and interfaces through an external Signal Conditioning 4 (SC4) module that features 8 analog inputs and 8 analog outputs and associated AD/DA converters, with an input/output range of -10 to 10 V each.

The Nanonis software package driving the RCS is written in Labview. It offers functionality such as PID controllers, force-distance curves, spectral analysis, image acquisition and force-volume experiments. For further functionality custom Labview programs can be incorporated through subVIs.

Oscillation control

The 'OC4' module functions as the lock-in amplifier of the system, featuring a bandwidth from 100 Hz to 1 MHz, a maximal excitation voltage of 10 V and maximal input signal up to 10 V. It can also function as a Phase-Locked Loop (PLL) and spectrum analyzer.

High Voltage Amplifier

The 10 V output of the SC4 module is not sufficient to directly drive piezoactuators which may require up to 400 V to achieve full extension. For this purpose the Nanonis SPM controller is equipped with the High Voltage Amplifier (HVA4) module. It amplifies 4 input signals (X, Y, Z, Aux) into 6 output signal (X-, X+, Y-, Y+, Z, Aux) with a selectable gain of 1, 4, 15 and 40, and a bandwidth up to 300 kHz.

2.5.5 Isolation

AFM systems rely on nanometric alignment of multiple components and use mechanical oscillations to investigate interactions. This makes them susceptible to external mechanical noise sources, such as vibrational noise that enters the setup through its connection with the floor.

For this purpose the setup is positioned on a marble slab with a weight of roughly 1000 kg suspended on 6 springs. Due to the large mass of the table, the spring-table system has a resonance frequency on the order of 1 Hz and will damp the vibrations sufficiently above this frequency.

Acoustic vibrations can also enter the system through the AFM lever. No measures were taken to remove these from the system in its current iteration, though they were also not found to significantly influence the presented results.

During operation the noise floor of the system for frequencies above 1 kHz was found to be on the order of 1 pm/$\sqrt{\text{Hz}}$.

Thermal drift

As parts of the AFM are exchanging heat with the environment the AFM system is not at full thermal equilibrium. This causes time dependent temperature gradients in the system, creating thermal expansion and dilatation. To ensure a stable measurement, AFM systems are often thermally isolated and allowed to equilibrate before measuring.

The homemade AFM was not thermally isolated from the lab room. To nevertheless minimize thermal expansion in the system, it was left to equilibrate for 2 hours before each measuring session. After such a period of equilibriation the drift between fiber and lever was on the order of 1 nm/min (Fig. 2.12). As a sweep of the probe-sample separation takes less than 10 minutes, the distance axis can drift by some 10 nm at maximum. This was found to be sufficiently small to perform the presented measurements at the accuracy required.

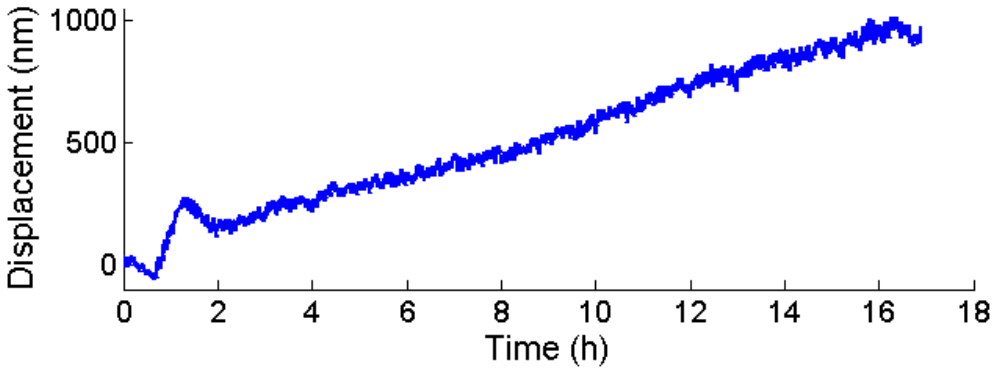

Figure 2.12: Drift of the probe-fiber system over time, which was found to be on the order of 1 nm/min.

Should it be desired to further minimize thermal drift in the future, the setup can be mounted on a smaller breadboard and positioned inside a thermally and acoustically isolated chamber.

2.6 Stiffness calibration

Accurate calibration of the lever stiffness is important in any quantitative AFM measurement, either to calibrate the force axis in static measurements or to quantify the probe-sample interaction in dynamic measurements.

In principle it is possible to directly determine the stiffness k_c of an unloaded AFM cantilever by solving the Euler-Bernoulli beam equation for the first mode, which finds

$$k_c = \frac{Et^3w}{4l^3} \tag{2.7}$$

where E is the Young's modulus of the beam material and l, w and t are its length, width and thickness. This value scales with the thickness of the lever to the third power, which is hard to measure and not well controlled in the silicon etching process used for AFM lever fabrication. As such it is important to calibrate the stiffness of the lever in-situ.

Multiple methods have been proposed to this purpose [115], with notable mentions such as calibration against a known standard [116], the Cleveland added mass model [117] and the so called Sader method [118,119]. For the work presented here we used the thermal method. [120] It is commonly used in the field as it requires no external measurement of the lever shape or manipulation of the lever.

In this method, the lever is modeled as an harmonic oscillator with a single degree of freedom connected to a thermal bath. Molecules from the thermal bath excite this degree of freedom creating the so called Brownian motion. Through the equipartition theorem we state that the total thermal energy for a single degree of freedom is $\frac{1}{2}k_bT$, where k_b is the Boltzmann constant and T the temperature of the thermal bath. This thermal energy is distributed over all the oscillatory modes of the AFM lever, but as the stiffness of each mode increases significantly with mode number we can neglect the energy stored in modes beyond the first. [121] We write

$$\frac{1}{2}k_c\langle x^2\rangle \approx \frac{1}{2}k_BT \tag{2.8}$$

where k_c is the stiffness of the lever in the first mode and $\langle x^2\rangle$ the mean square displacement of the first mode of the lever. $\langle x^2\rangle$ can be determined from the power spectral density PSD of the lever ($S(\omega)$, in units of m^2/Hz), measured in absence of any excitation beyond the thermal bath (Fig. 2.13). The PSD is determined by taking the square of the measured amplitude response $A(\omega)$ and dividing by the integration bandwidth through $S(\omega) = \frac{A(\omega)^2}{B}$. The PSD of the first mode for an harmonic oscillator in the high Q limit can be approximated as

$$S(\omega) = A^2_{white} + \frac{A^2_{\omega_0}\omega_0^2}{4Q^2}\frac{1}{(\omega-\omega_0)^2 + (\frac{\omega_0^2}{4Q^2})} \tag{2.9}$$

where A_{ω_0} is the amplitude at the resonance frequency. This equation can be directly fitted with a Lorentzian. [122] From this we determine the mean square displacement through

$$\langle x^2\rangle = \int_0^\infty S(\omega)d\omega \tag{2.10}$$

$$= \frac{\pi A^2_{\omega_0}\omega_0}{2Q} \tag{2.11}$$

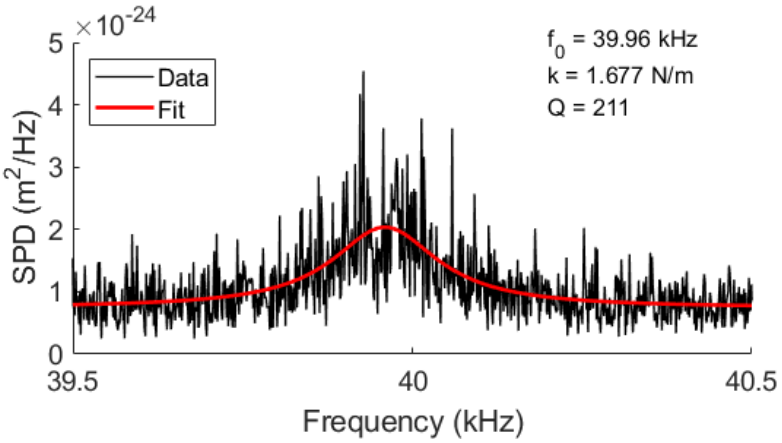

Figure 2.13: Brownian motion of an AFM lever in air, as measured with the homemade AFM.

One could expect that the simple harmonic oscillator model for unloaded beams loses validity for colloidal AFM probes. However, loading the cantilever by gluing a sphere was not found to significantly alter the shape of the first bending mode. [123]

The dynamic nature of the non-contact measuring method requires AFM cantilever with a resonance frequency on the order of 10 kHz, resulting in a stiffness on the order of 1 N/m. Measuring the Brownian motion of such stiff levers in liquid is unfeasible due to the high dissipation. For this reason, the stiffness of each lever was determined in air.

2.7 Force sensitivity

To evaluate the performance of the setup we can estimate the minimal force density S_{FF} that can be resolved. As the applied force is determined by measuring the displacement of the lever, the force detection sensitivity is related to the displacement detection sensitivity S_{XX} through

$$S_{FF} = \frac{S_{XX}}{|X|^2} \tag{2.12}$$

Where $|X|^2$ is the transfer function of the system, which can be determined from the intrinsic resonant properties of the lever. At frequencies below 100 Hz S_{XX} is dominated by the $1/f$ noise. For higher frequencies the system has a constant broadband noisefloor of about 1 pm^2/Hz (Fig. 2.13).

When measuring the liquid the lever has a lower quality factor due to increased dissipation. The transfer function only varies on the order of unity and can be approximated by its low frequency value which is the inverse of the lever stiffness. For the non-contact measurements in liquid presented in this work, the lever stiffness is on the order of 1 N/m. From these values we can estimate S_{FF} at 1 pN^2/Hz, meaning we can resolve a 1 pN force in a second.

This far exceeds the sensitivity requirements from table 2.1. The difficulty of the non-contact measuring method in liquid is not one of sensitivity but of stability and clean excitation of the lever.

2.8 Colloidal probes

Colloidal AFM probes are an important tool in the quantitative measuring of interaction profiles. In this work they were used for both the non-contact measuring technique and for nano-indentation into quick clay. Their well defined geometry allows for modeling of probe-sample interactions and due to their radial symmetry the probes are insensitive to problems of parallelism.

At the time of writing, no mass produced colloidal AFM probes are commercially available. Some commercial probes can be bought, but these are made by hand and thus quite expensive, making it generally more convenient to make them manually for each measurement.

The following is a description of the production protocol used for creating colloidal probes in this work. Gold coated probes were required for the capacitive excitation technique presented in chapter 4, while uncoated probes were used for the measurement on clay in chapter 7.

2.8.1 Materials

The colloidal probes consist of three components: a tipless AFM cantilever, a colloidal sphere and glue to connect the two together.

NSC and CSC series tipless probes by MikroMasch were used as a base lever. Made of n-type silicon, they are available with a stiffness between 0.03 and 16 N/m and resonance frequencies in air between 10 and 300 kHz. The levers have a width of 35 µm, thickness of about 2 µm and length varying between 90 and 350 µm depending on the desired stiffness. The backside of the lever is coated with aluminum to increase reflectivity.

While long ranged interactions are not very sensitive to the precise surface state of the probe, it is still advisable to use smooth spheres. Duke Standard spheres of borosilicate glass with a radius of 10 or 30 µm were used, as supplied by ThermoScientific, which are listed with a mean diameter of 20.2 µm and standard deviation of 2.8 µm. They were supplied as dry

spheres in a bottle. Previously the spheres were found to have a RMS surface roughness of 0.7 nm. [74]

A rapid drying two-component epoxy was used as a glue, as sold by Sader.

A micro positioning system is required for the physical manipulation of the lever, for which an NT-MDT NanoSolver AFM was used. An overhead microscope was used to guide the lateral displacement of the AFM lever.

2.8.2 Creation protocol

The colloidal probes used in this work were created through the following protocol:

- The base probe is mounted in the AFM.
- A clean silicon wafer is cut into squares of approximately 1 cm^2.
- Some spheres are removed from the bottle using clean tweezers and deposited on a first silicon square.
- The two components of the epoxy resin are mixed together thoroughly on a glass slide.
- Using a piece of stiff metal wire, the mixed resin is deposited on a second wafer square as a droplet of about 1 mm diameter.
- The two silicon squares are mounted side-by-side in the AFM.
- The end of the lever is approached onto the edge of the droplet until it breaks the surface tension and enters the resin.
- After about 2 seconds the lever is removed from the resin by retracting.
- The lever is moved over the other silicon square and aligned over an isolated sphere.
- The lever is approached onto the sphere, taking care that sphere and lever remain well aligned during the approach.
- As soon as the resin touches the sphere, surface tension will pull it into the lever. The lever is retracted as soon as this happens.
- The lever is removed from the AFM and left to dry for at least 12 hours.

2.8.3 Determination of probe radius

As there is some spread in the sphere size, the radius of each colloidal probe was determined using a calibrated optical microscope before each measurement (Fig. 2.14). Found values were consistently within a µm of those indicated by the supplier.

2.8.4 Conductive coating

As the colloidal probes are made of borosilicate glass, a conductive coating is required for capacitive excitation. Typically the probes are coated with a sub 100 nm layer of metal through magnetron sputtering. The requirements for this coating are to adhere to the borosilicate glass and not significantly increasing surface roughness. To avoid deformation of the coating upon unintentional contact with the sample surface, it is useful to choose a coating that is mechanically resilient.

Previously created probes were used for the capacitive excitation as a time saving measure. These probes were made for Casimir force [124] [125] and nanoscale radiative heat flux measurements. [110] [109] In these measurements the optical properties in the IR range matter and thus

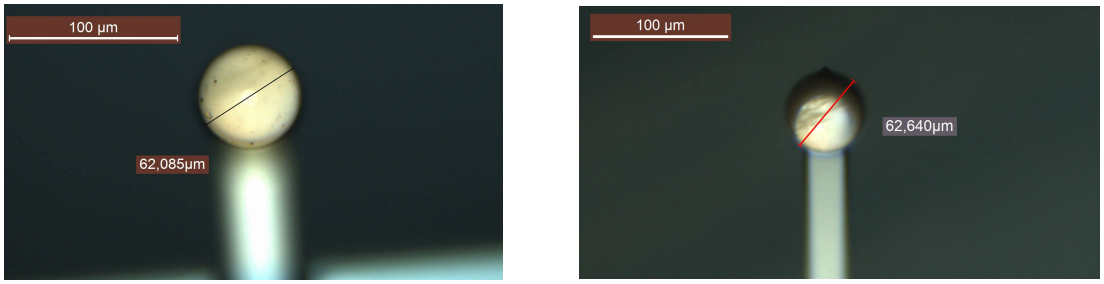

(a) (b)

Figure 2.14: Microscope images of glued colloidal probes, including radius determination.

they are covered with 60 nm of gold on top of a 15 nm adhesion layer of chromium. This has the down side of gold being relatively plastic and can deform upon contact. As unintentional contact with the surface is difficult to avoid during an experiment, the metallic coating will likely degrade over time within the area of contact. Due to long range nature of the forces investigated in this manuscript the impact of this on the accuracy of the measurement is expected to be small.

Chapter 3

Theoretical considerations

Contents

3.1 Introduction

As explained in the previous chapter, capacitive excitation in liquid provides us with a near analytical transfer function over a broad frequency range that is free of the parasitic resonances that plagues piezoacoustic excitation. To perform the non-contact determination of mechanical properties in liquid as described in chapter 1, we have to specify how this capacity can be used to determine the mechanical impedance $\mathcal{Z}(z)$ of the probe-sample interaction.

Two methodologies will be presented that allow us to extract $\mathcal{Z}(z)$ from the harmonic properties of the excited lever. First by tracking the resonance frequency ω_0 and the quality factor Q of the oscillating lever as these vary due to the probe-sample interaction. This only requires determination of the shape of the resonance and is independent of the excitation strength. This method is limited in that it only provides access to $\mathcal{Z}(z)$ at the resonance frequency of the lever.

The second methodology determines $\mathcal{Z}(z)$ from the change in the amplitude and phase response at a specific frequency. This requires that the scaling of the driving force with separation z is explicitly taken into account. As the driving force scales with V^2 as well, the system is driven at both the first and second harmonic of the excitation frequency. We will show that for our application it can be beneficial to utilize the second harmonic, as it does not depend the surface potential V_0.

For both methods the measured data must be compared to the intrinsic resonant properties of the system in absence of probe-sample interaction. Due to the nature of capacitive excitation this cannot be done directly as the excitation strength decays with increasing separation and does not provide a signal at separation arbitrarily far from the surface. While this is a problem for the excitation technique in general, for the specific application of the non-contact measurement of mechanical properties we will show that the free properties of the resonant system can be extracted by performing a calibration measurement at a known distance from the surface. Knowledge of the precise nature of the probe-sample interaction at large distances allows the interaction components to be substracted and the natural response of the lever to be approximated.

3.2 $\mathcal{Z}(z)$ from the resonant properties

To extract $\mathcal{Z}(z)$ directly from the shape of the resonance of the lever, we will describe the system as an harmonic oscillator (Fig. 3.1) and express the equation of motion in terms of the resonant properties ω_0 and Q. We will then quantify their change under the additional probe-sample interaction $Z'(z) = k_{int}(z)$ and $Z'' = \gamma_{int}(z) \cdot \omega$.

The AFM probe and lever can be described as a driven harmonic oscillator, for which the equation of motion is given by

$$m\ddot{x} + \gamma_c \dot{x} + k_c x = F_d \tag{3.1}$$

where k_c is the effective stiffness value of the lever and γ_c its effective dissipation, predominantly determined by dissipation in the surrounding medium. The capacitive driving force F_d will be further specified in the next section, but is of the shape $F_d = F_{cap}\cos(\omega t)$. The equation of motion can be expressed in the properties of the harmonic oscillator by defining

$$\omega_0 = \sqrt{\frac{k_c}{m}} \tag{3.2}$$

$$Q = \frac{m\omega_0}{\gamma_c} \tag{3.3}$$

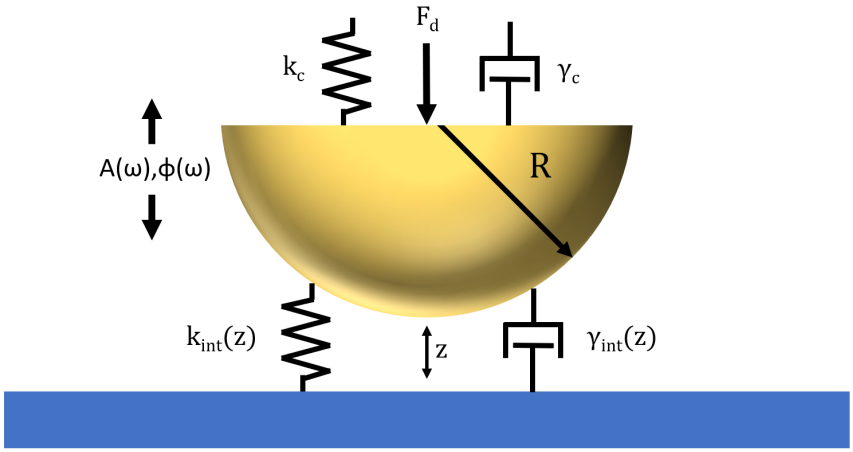

Figure 3.1: Overview of the relevant parameters in the system. A spherical probe of radius R is connected to the AFM lever with stiffness k_c and internal dissipation γ_c. An oscillating driving force F_d excites the system at frequency ω, which leads to an oscillation with amplitude A_ω and phase ϕ_ω. When brought at a separation z from the surface, additional conservative and dissipative interaction terms $k_{int}(z)$ and $\gamma_{int}(z)$ enter the equation of motion and change the resonant properties of the system.

and rewriting the equation of motion as

$$\frac{F_d}{m} = \ddot{x} + \frac{\omega_0}{Q}\dot{x} + \omega_0^2 x \tag{3.4}$$

Following the regular description of a driven harmonic oscillator, [126] the steady state solution for the amplitude of the oscillation as a function of frequency can likewise be written as

$$A(\omega) = \frac{F_d}{k_c}\frac{1}{\sqrt{\left(1-\frac{\omega^2}{\omega_0^2}\right)^2 + \left(\frac{\omega}{\omega_0 Q}\right)^2}} \tag{3.5}$$

By measuring the amplitude response of the probe and lever as a function of ω and fitting the above expression, Q and ω_0 can be directly determined. F_d can be determined as well if the stiffness of the lever is known, though this is not required for our current analysis.

If a probe-sample interaction with a conservative component $k_{int}(z)$ is added the resonance frequency will shift from ω_0 to $\omega_0'(z)$ according to

$$\omega_0'(z) = \sqrt{\frac{k_c + k_{int}(z)}{m}} \tag{3.6}$$

which can be rewritten as an expression for the conservative component of the mechanical impedance through

$$Z'(z) = k_{int}(z) = k_c\left(\frac{\omega_0'(z)^2}{\omega_0^2} - 1\right) \tag{3.7}$$

Any additional dissipative component will likewise change the quality factor Q to $Q'(z)$

through

$$Q'(z) = \frac{m\omega_0'}{\gamma_c + \gamma_{int}(z)} \tag{3.8}$$

which can be rewritten into an expression for the dissipative component of the mechanical impedance through

$$Z''(z) = \gamma_{int}(z) \cdot \omega_0 = \frac{k_c}{\omega_0}\left(\frac{\omega_0'(z)}{Q'(z)} - \frac{\omega_0}{Q}\right) \tag{3.9}$$

The measurement consists of calibrating the resonant properties ω_0 and Q of the lever without interaction, and measuring $\omega_0'(z)$ and $Q'(z)$ while approaching the sample (Fig. 3.2). From these measured values $\mathcal{Z} = Z' + iZ''$ can be directly determined through equations (3.7) and (3.9).

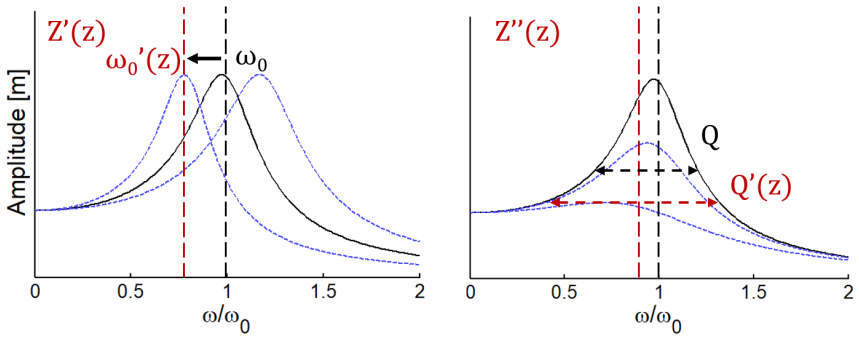

Figure 3.2: Adding a conservative probe sample interaction $Z'(z)$ will shift the resonance frequency of the oscillator according to equation (3.7), while adding a dissipative interaction $Z''(z)$ will decrease the quality factor according to equation (3.9).

3.3 $\mathcal{Z}(z)$ from amplitude-phase-distance data

To determine $\mathcal{Z}(z)$ from the variation of the amplitude $A_\omega(z)$ and phase $\phi_\omega(z)$ measured at a specific frequency, we first have to precisely quantify the capacitive driving force.

3.3.1 Capacitive excitation in liquid

To determine the driving force provided by capacitive excitation, we will describe our conducting colloidal probe and substrate as a capacitive system with interdistance z (Fig. 3.1). [105] From the energy in a capacitor we derive

$$U_{cap} = \frac{1}{2}CV^2 \tag{3.10}$$

$$F_{cap} = -\frac{dU_{cap}}{dz} \tag{3.11}$$

$$= -\frac{1}{2}\frac{dC}{dz}V^2 \tag{3.12}$$

$$\frac{dF_{cap}}{dz} = -\frac{1}{2}\frac{d^2C}{dz^2}V^2 \tag{3.13}$$

The applied force and its derivative depend on first and second derivative of the capacitance of the system, which is determined by the geometry of the probe and substrate.

Sphere-plane geometry

The advantage of using colloidal probes is that the capacitance of the sphere-plane geometry can be analytically described by a two geometrical parameters. The capacitance for a sphere of radius R at separation z from an infinite half plane is given by the series

$$C_{sp} = 4\pi\epsilon_0\epsilon_r R \sinh(\alpha) \sum_{n=1}^{\infty} \frac{1}{\sinh(\alpha)} \tag{3.14}$$

where $\cosh(\alpha) = 1 + \frac{z}{R}$ and ϵ_r is the relative permittivity of the material filling the space between the plane and sphere. [127] Calculating the series for each separation is impractical, but under the assumption of small separations $z << R$, as will be the case in our measurements, it can be approximated as

$$C_{sp} \approx 2\pi\epsilon_0\epsilon_r R \left(\ln\left(\frac{R}{z}\right) + \beta \right) \tag{3.15}$$

where β is a numerical constant. [128] It is clear that for the derivatives we find

$$\frac{dC_{sp}}{dz} = -2\pi\epsilon_0\epsilon_r \frac{R}{z} \tag{3.16}$$

$$\frac{d^2C_{sp}}{dz^2} = 2\pi\epsilon_0\epsilon_r \frac{R}{z^2} \tag{3.17}$$

Excitation force

From this we can determine the force exerted on the probe by an externally applied potential difference

$$F_{cap} = \pi\epsilon_0 \frac{R}{z} V^2 \tag{3.18}$$

$$\frac{dF_{cap}}{dz} = -\pi\epsilon_0 \frac{R}{z^2} V^2 \tag{3.19}$$

When applying an oscillating potential difference $V = V_{DC} - V_0 + V_{AC}\cos(\omega t)$, with V_{DC} the static component, V_0 due to any surface charge and V_{AC} the oscillation strength, this creates a force $F_{cap}(z)$ at three frequency components:

$$F_{cap}(z) = f_0(z) + f_\omega(z)\cos(\omega t) + f_{2\omega}(z)\cos(2\omega t) \tag{3.20}$$

$$f_0(z) = \frac{\pi\epsilon_0\epsilon_r R}{z}\left((V_{DC} - V_0)^2 + \frac{1}{2}V_{AC}^2 \right) \tag{3.21}$$

$$f_\omega(z) = 2\frac{\pi\epsilon_0\epsilon_r R}{z}\left(V_{DC} - V_0\right) V_{AC} \tag{3.22}$$

$$f_{2\omega}(z) = -\frac{1}{2}\frac{\pi\epsilon_0\epsilon_r R}{z} V_{AC}^2 \tag{3.23}$$

In this expression f_0 results in a static deflection of the lever, while the other two components provide excitation at both the first and second harmonic of the excitation frequency.

The f_ω component depends on the surface potential V_0, an uncontrolled parameter that is the result of the local state of the electrodes. It can be measured independently by sweeping V_{DC} and finding the point for which $f_\omega(V_{DC} = V_0) = 0$, a technique that is utilized in Kelvin Probe Force Microscopy. [106] For measurements in PDMS oil on a silicon surface it was found to be on the order of -100 mV and varies slightly with z, as will be presented in the next chapter. For this reason it can be beneficial to use the second harmonic for excitation, so that the driving force is independent of $V_{DC} - V_0$.

Additional force gradient

A downside of capacitive excitation is that the gradient of the driving force ∇f_0 enters the measurement as an additional stiffness. If our amplitude of oscillation is small compared to the spatial variance of ∇f_0, we can linearize its contribution at a specific distance z_0 and express it as

$$\begin{aligned} f_0(z \approx z_0) &\approx f_0(z_0) + (z - z_0) \cdot \nabla f_0(z_0) + O\left((z - z_0)^2\right) + \dots && (3.24) \\ &\approx [f_0(z_0) - z_0 \cdot \nabla f_0(z_0)] + z \cdot \nabla f_0(z_0) && (3.25) \end{aligned}$$

The term in brackets does not vary in time or space and is a static deflection of the lever that can be ignored for the time development of our system. The other term acts as an additional stiffness that varies with z.

$$\begin{aligned} k_{cap}(z) &= -\nabla f_0(z) && (3.26) \\ &= \frac{\pi \epsilon_0 \epsilon_r R}{z^2} \left((V_{DC} - V_0)^2 + \frac{1}{2} V_{AC}^2 \right) && (3.27) \end{aligned}$$

Any additional conservative probe-sample interaction, such as the buckling of the soft surface in the non-contact determination of mechanical properties, will be superimposed on this force gradient as $k_{tot} = k_c + k_{int} + k_{cap}$. Determining k_{int} will require subtracting this additional force gradient, which is made difficult by the dependency on V_0 which has to be determined in a separate measurement. A directer method to determine $\nabla f_0(z)$ could consist of taking the gradient of the measured static deflection of the lever $f_0(z)$.

3.3.2 Determining $\mathcal{Z}(z) = Z'(z) + iZ''(z)$

With the capacitive driving force quantified, we have all the required components to express $\mathcal{Z}(z)$ in terms of the observable of our measurement, $A_\omega(z)$ and $\phi_\omega(z)$. The derivation presented here follows Rodrigues et.al. [80] with novel additions to describe the specific case of capacitive excitation.

We again describe the AFM lever as a damped harmonic oscillator, this time expressing the equation of motion as

$$m\ddot{x} + \gamma_t(z)\dot{x} + k_t(z)x = f_\omega(z)\cos(\omega t) \tag{3.28}$$

where k_t and γ_t are the effective total stiffness and dissipation coefficients of the system at a distance z from the surface

$$\begin{aligned} k_t(z) &= k_c + k_{int}(z) - \nabla f_0(z) && (3.29) \\ \gamma_t(z) &= \gamma_c + \gamma_{int}(z) && (3.30) \end{aligned}$$

Here $k_{int}(z)$ and $\gamma_{int}(z)$ are the changes in the effective stiffness and dissipation coefficient due to the probe-sample interaction and $\nabla f_0(z)$ is the additional force gradient introduced by the capacitive excitation as explained in the previous section.

By solving the damped harmonic oscillator for a driving force $f_\omega(z)$, we find the stationary state solutions for the amplitude $A_\omega(z)$ and phase $\phi_\omega(z)$ as expressed in k_t and γ_t

$$A_\omega(z) = \frac{f_\omega(z)}{\sqrt{(k_t(z) - m\omega^2)^2 + \gamma_t(z)^2\omega^2}} \tag{3.31}$$

$$\phi_\omega(z) = \arctan\left(\frac{\gamma_t(z)\omega}{k_t(z) - m\omega^2}\right) \tag{3.32}$$

Using these equations we can define the force/response ration $F_r(z)$ as

$$F_r(z) = \frac{f_\omega(z)}{A_\omega(z)} \tag{3.33}$$

$$= \sqrt{(k_t(z) - m\omega^2)^2 + \gamma_t(z)^2\omega^2} \tag{3.34}$$

By splitting the real and imaginary parts of F_r and writing out the individual components of $k_t(z)$ and $\gamma_t(z)$ we find

$$F_r(z)\cos(\phi_\omega(z)) = k_c + k_{ts}(z) - \nabla f_0(z) - m\omega^2 \tag{3.35}$$

$$F_r(z)\sin(\phi_\omega(z)) = (\gamma_c + \gamma_{ts}(z))\omega \tag{3.36}$$

which allows us to relate the components of the interaction to our observables.

When moving sufficiently far away from the surface to a distance z_0, so that $k_{int}(z) \approx 0$ and $\gamma_{int}(z) \approx 0$, we find the bulk response of the system

$$F_r(z_0)\cos(\phi_\omega(z_0)) = k_c - m\omega^2 \tag{3.37}$$

$$F_r(z_0)\sin(\phi_\omega(z_0)) = \gamma_c\omega \tag{3.38}$$

Combining these four equations we can express the components of the probe-sample interaction in the combination of these two responses as

$$k_{int}(z) = F_r(z)\cos(\phi_\omega(z)) - F_r(z_0)\cos(\phi_\omega(z_0)) + \nabla f_0(z) \tag{3.39}$$

$$\gamma_{int}(z) = \frac{F_r(z)}{\omega}\sin(\phi_\omega(z)) - \frac{F_r(z_0)}{\omega}\sin(\phi_\omega(z_0)) \tag{3.40}$$

or written alternatively

$$k_{int}(z) = F_r(z_0)\left[n(z)\cos(\phi_\omega(z)) - \cos(\phi_\omega(z_0)) - \frac{\nabla f_0(z)}{F_r(z_0)}\right] \tag{3.41}$$

$$\gamma_{int}(z) = \frac{F_r(z_0)}{\omega}\left[n(z)\sin(\phi_\omega(z)) - \sin(\phi_\omega(z_0))\right] \tag{3.42}$$

$$\tag{3.43}$$

where

$$n(z) = \frac{F_r(z)}{F_r(z_0)} = \frac{f_\omega(z)A_\omega(z_0)}{A_\omega(z)f_\omega(z_0)} = \frac{A_\omega(z_0)}{A_\omega(z)}\left(\frac{z_0}{z}\right) \tag{3.44}$$

$$\tag{3.45}$$

In practice, our measurement consists of calibrating $F_r(z_0)$ and $\phi_\omega(z_0)$ at a known distance z_0 where the probe-sample interaction is negligible. The observables $A_\omega(z)$ and $\phi_\omega(z)$ are then measured while the probe approaches the surface. By calculating $n(z)$ and $\nabla f_0(z)$, we can determine $k_{int}(z)$ and $\gamma_{int}(z)$ which directly provides us with $\mathcal{Z}(z)$.

It should be noted that the ratio z_0/z directly enters $n(z)$ and will affect the found value for $\mathcal{Z}(z)$. This makes the technique sensitive to inaccuracies in the calibration of distance axis, which may occur due to thermal drift during the measurement or difficulties determining the precise position of the sample surface.

The calibration distance z_0

To determine $F_r(z_0)$ and $\phi_\omega(z_0)$ the response of the system would ideally be measured at a distance where there is no interaction with the surface. Due to the nature of capacitive excitation there is a limit to how far from the surface z_0 can be taken, as the excitation strength decreases as z^{-1} and will become too small to accurately measure the response of the system. This finite value for z_0 during calibration will induce an error in the values found for $F_r(z_0)$ and $\phi_\omega(z_0)$ due to residual interaction with the surface. This is one of the disadvantages of capacitive excitation in comparison to piezoacoustic excitation, where calibration can be performed arbitrarily far away from the surface.

For the technique in general these inaccuracies cannot be avoided, but in the specific case of the non-contact determination of mechanical properties, additional steps can be taken to minimize these effects.

At short distances from the surface the response of the probe is determined by coupling of the induced flow with the unknown compliance of the elastic surface. However, at larger distances beyond the crossover length $D_k = 8R\left(\frac{\eta\omega}{E^*}\right)^{2/3}$, the contribution to the conservative component decays quickly as $z^{-5/2}$, while the dissipative component is dominated by the Reynolds viscous damping. [54] The response of the system at a known calibration distance $z_c >> D_k$ is thus fully determined by the Reynolds viscous damping and the electrostatic gradient.

If a known liquid medium with viscosity η and relative permittivity ϵ_r is used, the probe-sample interaction at these distance is fully described by

$$k_{int}(z_c) = \nabla f_0(z_c) = \frac{\pi\epsilon_0\epsilon_r R}{z_c^2}V^2 \tag{3.46}$$

$$\gamma_{int}(z_c) = f_{Reynold}(z_c) = \frac{6\pi\eta R^2}{z_c} \tag{3.47}$$

By measuring the resonant properties $\omega_0'(z_c)$ and $Q'(z_c)$ of the lever at this distance, combined with the knowledge of η, ϵ_r, R and V, it is possible to subtract these interactions and determine the natural properties ω_0 and Q of the oscillating lever. This is done by inverting equations (3.7) and (3.9), and taking

$$\omega_0 = \sqrt{\omega_0'(z_c)^2 - \frac{k_{int}(z_c)}{m}} \tag{3.48}$$

$$\frac{m\omega_0}{Q} = \frac{m\omega_0'(z_c)}{Q'(z_c)} - \frac{\gamma_{int}(z_c)}{m\omega_0} \tag{3.49}$$

The calibration parameters $F_r(z_0)$ and $\phi_\omega(z_0)$ can then be directly calculated through equations (3.33) and (3.32). With $F_r(z_0)$ known, we can determine $n(z)$ from $A_\omega(z)$ by taking

$$n(z) = \frac{1}{F_r(z_0)A_\omega(z)} \cdot \frac{1}{z} \tag{3.50}$$

In practice this alternative method of calibration was found to be more reliable than simply assuming the interaction forces at a distance of z_0 to be negligible, as will be demonstrated in the next chapter.

One could argue that using η to calibrate invalidates the measurement, as it presupposes the result of the measurement. It should however be noted that this parameter is only assumed to be true far from the surface in the bulk and not assumed to remain constant closer to the surface.

3.4 Conclusions

In summary we have described two separate methods for determining the mechanical impedance of the probe-sample interaction $\mathcal{Z}(z)$ using capacitive excitation. A first that determines $\mathcal{Z}$ from the change in resonant properties of the lever and a second that determines it from the amplitude and phase response at a specific frequency. The results of these separate methodologies allows us to compare them in terms of sensitivity and accuracy.

As the capacitive excitation strength decays as a function of separation from the surface, calibration measurements without probe-sample interaction cannot be directly performed, though at sufficiently large distances they can be approximated to be absent. Alternatively for the specific application of the non-contact determination on mechanical properties in liquid, calibration can be performed at distances larger than the transition length, where the interaction is fully described by the electrostatic gradient and viscous damping.

In the following the chapters the methodologies described in this chapter will be demonstrated for the cases of PDMS oil and deionized water on a solid surface, using the homemade AFM setup described in chapter 2. We will see that while the first methodology works in both cases, the second methodology does not work for deionized water as the driving force cannot be quantified.

Chapter 4

Capacitive excitation in PDMS oil

Contents

4.1 Introduction

The key to determining the stiffness of a soft material in liquid using capacitive excitation is accurate determination of the the mechanical impedance $\mathcal{Z}(z)$ of the probe-sample interaction over a distance of multiple microns to some nanometers from the surface. In this chapter we present the measurement of $\mathcal{Z}(z)$ on our homemade setup as described in chapter 2, using the two methodologies described in chapter 3.

PDMS oil is used as a non-conducting, non-slipping and non-dissociating reference liquid that has a viscosity comparable to water. A silicon wafer is used as the sample surface, which can be considered as a smooth rigid wall. In this configuration the conservative component of the probe-sample interaction consists only of the electrostatic gradient imposed on the system, while the dissipative component is determined by the Reynolds dissipative force. Both of these interactions can be analytically described without any free parameters, creating a useful system of reference.

As explained in chapter 3, the first methodology used consists of measuring the full resonant response of the lever as it varies with distance from the surface. By tracking the change in the resonant frequency and quality factor of the lever, it is possible to determine the mechanical impedance of the interaction at the resonance frequency. This method has the advantage of being straightforward to analyze, as it does not quantitatively depend on the excitation force and only requires determination of the shape of the resonance.

This classical method to determine the mechanical impedance is normally utilized in air and vacuum where quality factors are high. When measuring in liquid a lot of energy is dissipated by the liquid flowing around the lever with each oscillation, decreasing the quality factor of the lever and lowering sensitivity.

The second methodology involves measuring the amplitude and phase at a single frequency as they vary with probe-sample separation z. The mechanical impedance is extracted from these two observables through comparison with the intrinsic properties of the lever when no probe-sample interaction is present, combined with quantitative knowledge of the driving force as a function of separation. This has the advantage of independently determining the mechanical impedance at any frequency instead of being limited to the resonance frequency of the lever.

We will see that the determination of $Z''(z)$ using this method is very robust, but accurate determination of $Z'(z)$ is not possbile, as the result is too sensitive to the calibration parameters. These parameters consists of the quality factor and resonance frequency of the lever in absence of any interaction. Due to the nature of capacitive excitation, it is not possible to determine these calibration parameters directly, but they must be calculated using calibration curves under residual interaction. As we will see, this calibration process is imperfect, making it difficult to determine $Z'(z)$

To support the claim the limiting factor in the determination of Z' is accurate determination of the calibration parameters, numerical simulations will be presented that qualitatively reproduce the found results if small calibration errors are added to the system.

Lastly, we present a first attempt at demonstrating capacitive excitation and the measurement of the mechanical impedance in deionized water. While the capacitive excitation in water only provides sufficient excitation at separations beyond 2 µm, we will demonstrate that at these distances it is possible to extract the mechanical impedance of the probe-sample interaction at resonance from the change in ω_0 and Q.

4.2 Measurements in PDMS oil

An overview of the used material is provided, after which the functioning of capacitive excitation in PDMS oil is presented. After this two sets of measurements in 5 cSt PDMS oil are presented, one per methodology described in chapter 3.

4.2.1 Materials

The measurements were performed on a p-doped silicon wafer using 5 cSt PDMS oil. AFM levers with gold coated spheres were used as probes.

Substrate

A [100]-orientation silicon wafer is used as a rigid substrate. This semiconductor is a p-type doped to allow charges to flow through, with a resistivity of 0.2 to 0.4 Ω/cm^2 as indicated by the supplier.

The electrical connection to the silicon wafer was made through a steel clamp. While this does not provide an ohmic contact, due to its macroscopic size the capacitance of the the clamp-wafer capacitor is orders of magnitude bigger than that of probe-substrate capacitor. The potential difference lost in the steel clamp is thus negligible.

It should be noted that the zero position for the electrostatic force between probe and substrate does not necessarily coincide with the physical surface of the substrate. Should the silicon wafer be covered with a non-conducting oxide, the charges generating the electrostatic force will be trapped some distance below the surface. As such the zero position found for the electrostatic force and the Reynolds force need not coincide. In general the native oxide layer on silicon is on the order of 0.1 nm. [129] It is thus expected that in the experiment the two zero positions are indistinguishable.

Colloidal probes

Gold covered colloidal probes were used as described in section 2.8. The radius of the spheres was measured to be on the order of 22.00 µm as determined through optical microscopy (Table 4.1).

During the measurement the scanner is moved towards the probe until it makes contact, due to which the surface state of the relatively plastic golden coating can deteriorate and locally lose its sphericity. After this occurs the capacitance of the sphere-plane system will deviate from its analytical value. These effects will nonetheless be limited due to the long range of the electrostatic force.

The stiffness of the used levers was around 2 N/m, with a resonance frequency of 35 kHz and quality factor of 200 in air (Table 4.1). This was determined by measuring the Brownian motion in air as described in section 2.6.

Measurement	R (µm)	k_c (N/m)	ω_0 (kHz)	Q
Methodology I	22.61	2.2	35.71	230
Methodology II	22.06	1.67	39.96	211

Table 4.1: Properties of the levers used in this chapter for measurements in PDMS oil, as determined from their Brownian motion in air.

PDMS oil

To accurately benchmark the experiment we require the probe-sample interaction to be well controlled, therefor the used liquid should have well known and stable viscous and dielectric properties. PDMS oil was chosen as a benchmark fluid, as it is a newtonian viscous fluid that is both non-conducting an non-disassociating with a viscosity comparable to water (Table 4.2). 5 cSt PDMS oil was supplied by Sigma Aldrich.

A 5 cSt kinematic viscosity with a density of 0.913 g/mL equates to a dynamic viscosity of $4.565{\cdot}10^{-3}$ Pas. The supplier indicates a possible variation in the viscosity of the supplied fluids of about 0.5 cSt.

5 cSt PDMS oil has a dielectric constant of 2.59. This value should be constant in the frequency range used in this work, but does slightly depend on temperature and moisture content. [130]

The index of refraction (n) of PDMS oil is 1.403, which affects the fiber optical detection method in two ways. It firstly increases the sensitivity by a factor of n by changing the effective wavelength of the laserlight inside the PDMS oil from $\lambda = 660$nm to $\lambda' = \frac{\lambda}{n} \approx 470$nm, as explained in chapter 2. Secondly the closer matching of the PDMS oil optical index to that of the silica inside the optical fiber ($n \approx 1.5$) significantly decreases the percentage of light reflected at the fiber-oil interface to only 0.1%, compared to 4% in air. This decreases the value of ΔI_0 and thus the sensitivity by a factor of 40, for a combined total decrease in sensitivity by a factor of 28. This decrease in sensitivity can be partially compensated by increasing the total laser power, though in total the sensitivity still suffers.

PDMS oil	5 cSt
Kin. Viscosity ν	4.5-5.5 cSt
Dyn. Viscosity η	$4.565 \cdot 10^{-3}$ Pas
Density ρ	0.913 g/mL
Refraction index n	1.403
Dielectric constant e_r	2.59

Table 4.2: Properties of the 5 cSt PDMS oil used as a benchmark liquid.

4.2.2 Capacitive excitation in PDMS oil

We will first demonstrate that capacitive excitation in PDMS provides us with the expected analytical transfer function. Using an excitation signal of $V_{AC} = 2V$ and $V_{DC} = 0V$, the probe was excited at a distance sufficiently close to the surface to obtain a signal.

Capacitive excitation provided a near analytical transfer function in 5 cSt PDMS oil (Fig. 4.1a). The resonant response of the system, though damped, is clearly visible. The amplitude and phase reponse are smooth functions over a 40 kHz range, both below and above the resonance frequency of about 22 kHZ. The amplitude and phase response can be directly fitted with their analytical description (Fig. 4.2), indicating a resonance frequency of some 21 kHz, a quality factor of about 2 and distance from the surface equal to some 7 µm. It will be confirmed in the following section 4.2.3 that this is indeed the correct distance from the surface.

The response not only followed the analytical description at the resonance, but over a broad frequency range. Such a clean resonant response is exceptional in AFM systems and difficult to obtain with more conventional forms of excitation. For comparison the same lever was excited using piezoacoustic excitation, both through the piezo-dither and the W-piezo that controls probe-fiber separation (Fig. 4.1b). The resonance of the lever is completely obscured by two

parasitic resonances at 7.5 and 15 kHz. These parasitic peaks were confirmed to be lever independent and make it impossible to use our homemade system with conventional piezo-acoustic excitation in this frequency range.

Determination of V_0

Before each measurement of the mechanical impedance $\mathcal{Z}(z)$, the surface potential term $V_0(z)$ was measured in a separate experiment to determine the size of the electrostatic gradient.

To determine $V_0(z)$ the system is excited using the first harmonic for which we can state

$$f_\omega = \frac{\pi\epsilon_0\epsilon_r R}{z} \cdot (V_{DC} - V_0)V_{AC} \tag{4.1}$$

The voltage V_{DC} is swept until the point at which $V_{DC} = V_0$ is found, at which $f_\omega = 0$ and $A_\omega = 0$ (Fig. 4.3a). The numerical value is determined by fitting the measured amplitude curves on both sides of the minimum with a 1st order polynomial, giving two zero-crossings of which the average is taken as V_0.

This measurement is repeated for varying separations z (Fig. 4.3b). The distance from the surface at each point was determined by fitting the strength of the driving force through equation (4.2), as will be explained in more detail in the following section. The found values were compared to the displacement of the scanner and found to be in agreement.

The found values for V_0 depended slightly on z in a linear fashion. A first order polynomial was fitted to the results and used for extrapolation of the result to smaller probe-sample separations not directly measured.

4.2.3 Methodology 1 - $\mathcal{Z}$ through the resonant properties

With the capacitive excitation in PDMS oil functioning as intended, the mechanical impedance of the interaction was determined using the first methodology described in chapter 3. The resonance frequency and quality factor of the AFM lever resonance are measured as a function of separation z and from which $\mathcal{Z}(z)$ can be calculated.

An AC voltage of 2 V was used to excite the lever while measuring on the second harmonic. Due to the relatively large amount of noise in the amplitude channel, the resonance frequency and quality factor were determined both by fitting the amplitude response and phase response (Fig 4.4). This provides two measures of $\mathcal{Z}$ that can be compared.

Determining ω_0 and $Q(z)$

The amplitude and phase response, as measured at each distance z, are fitted with

$$A(\omega, z) = \frac{1}{2}\frac{\pi\epsilon_0\epsilon_r R}{z'(z)}V_{AC}^2 \cdot \frac{1}{k_c}\frac{1}{\sqrt{\left(1 - \frac{\omega^2}{\omega_0(z)^2}\right)^2 + \left(\frac{\omega}{\omega_0(z)Q(z)}\right)^2}} \tag{4.2}$$

$$\phi(\omega, z) = \arccos\left(\frac{1 - (\frac{\omega}{\omega_0(z)})^2}{\sqrt{(1 - (\frac{\omega}{\omega_0(z)})^2)^2 + (\frac{\omega}{\omega_0(z)Q(z)})^2}}\right) \tag{4.3}$$

in which z', ω_0 and Q are the fitting parameters (Fig. 4.2). This provides us with two measurements of $\omega_0(z)$ and $Q(z)$, and one for $z'(z)$ (Fig. 4.5). ω_0 and Q as determined from the phase response were found to be a more reliable measurement as it contained less noise.

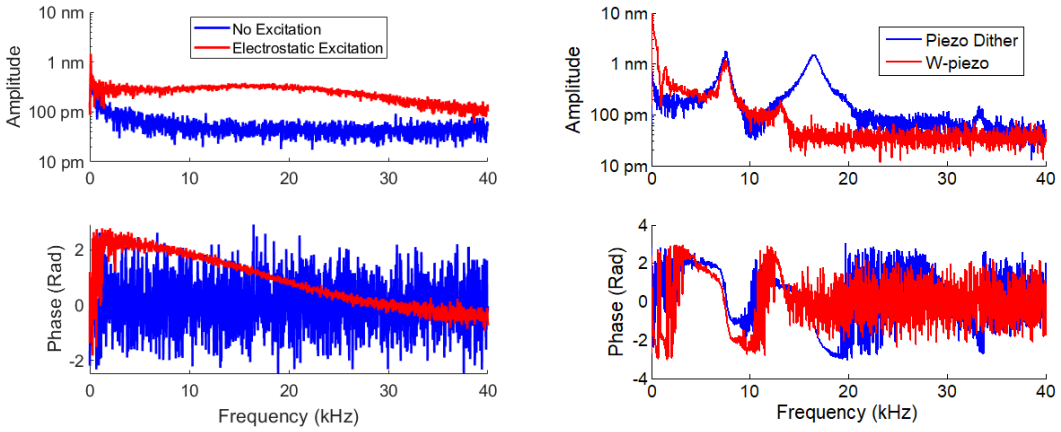

(a) (b)

Figure 4.1: Comparison of the amplitude and phase response in 5 cSt PDMS oil using (a) capacitive excitation and no excitation (b) piezoacoustic excitation using the piezo dither and the W-piezo that regulates probe-fiber separation. Capacitive excitation provides a smoothly varying transfer function that is devoid of parasitic peaks. In both cases where mechanical excitation is used, the lever response is obscured by parasitic resonances at 7.5 and 15 kHz.

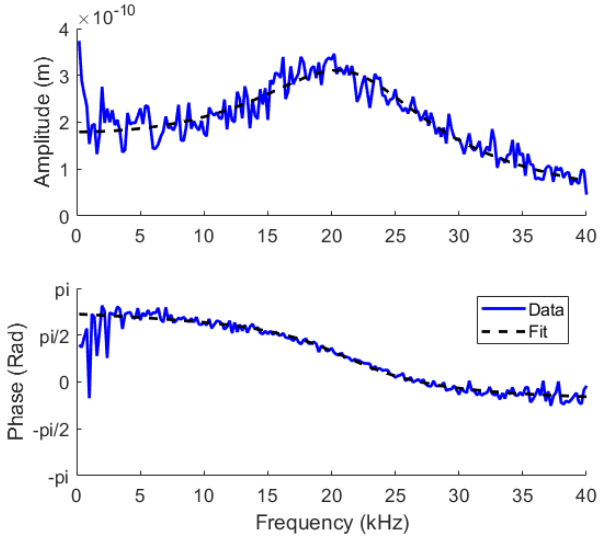

Figure 4.2: Amplitude and phase response as a function of frequency using capacitive excitation in 5 cSt PDMS oil using an excitation voltage of 2V. The measured curves are fitted with equations (4.2) and (4.3) to determine the excitation strength, resonace frequency and quality factor.

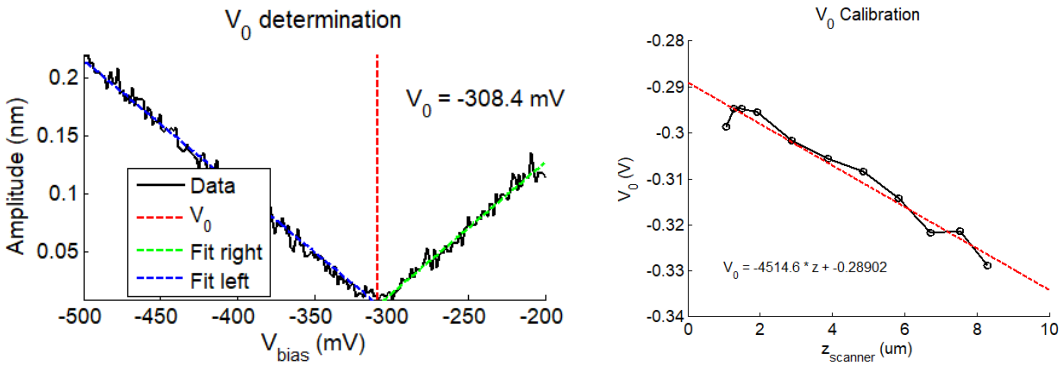

(a) (b)

Figure 4.3: (a) Determination of V_0 in 5 cSt PDMS oil. The amplitude is measured while sweeping V_{bias} to find the point at which $A_\omega(V_{DC} = V_0) = 0$. The numerical value is determined by fitting both sides of the minimum and taking the average of the zero crossing. (b) Variation of V_0 with probe-sample separation. To inter- and extrapolate to other values of z, the data is fitted with a line.

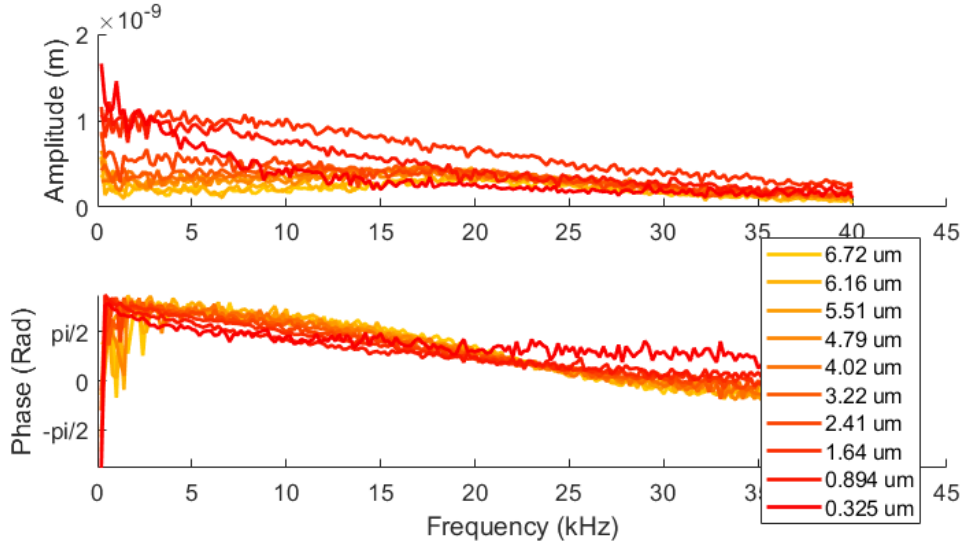

Figure 4.4: Measured amplitude and phase response at multiple distances from the surface, moving from yellow (far) to red (close). Closer to the surface the quality factor decreases, but the total measured amplitude increases due to the bigger driving force.

Data below 5 Khz were ignored in all fits as in this range the signal contains more noise, especially in $\phi(\omega)$.

Through the $z'(z)$ curve we verify that the excitation strength applied to the system corresponds to the expected theoretical value, in which case $z'(z) = z$ and the slope of the curve is unity. From the data we can see that this holds up for data points beyond the 300 nm closest to the surface. Fitting a first order polynomial to this data finds a slope of 1.064, and allows us to determine the zero of the electrostatic interaction, which in the curves is defined as 0 separa-

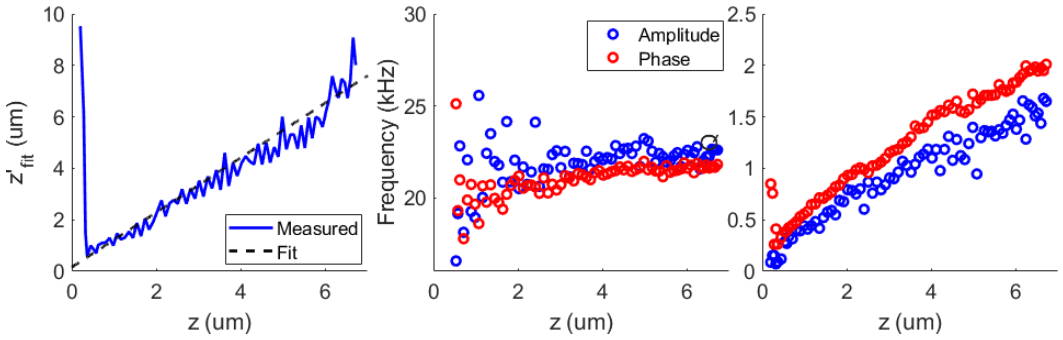

Figure 4.5: Fitting parameters as a function of probe sample separation, as measured using capacitive excitation in 5 cSt PDMS oil. The fitted distance from the surface as determined from the excitation strength is fitted with a line, which was found to be $z_{fit} = 1.064 \cdot z_{scanner}$. The zero crossing of the resulting line is taken as the 0 position. The resonance frequency and quality factor are fitted for each separation using both amplitude (blue) and phase (red) curves.

tion. Below 300 nm the excitation strength decreases significantly, likely due to the mechanical contact between an asperity on the colloid and the surface for these last two measuring points.

From the slope in the quality factor at large distances in figure 4.5 it is clear that there is significant residual interaction at the furthest separation from the sample. For a good calibration of the measurement the values found at this distance should saturate as it becomes independent of the probe-sample separation. While the value does not saturate, the average of the five data points furthest from the sample surface were used as calibration parameters ω_0 and Q due to lack of a better alternative.

Determining $\mathcal{Z}(z)$

As explained in chapter 3, the mechanical impedance of the interaction is determined through

$$Z'(z) = k \cdot \left(\left(\frac{\omega_0'(z)}{\omega_0} \right)^2 - 1 \right) \tag{4.4}$$

$$\frac{Z''(z)}{\omega_0} = k \cdot \left(\frac{Q \cdot \omega_0'(z) - Q'(z) \cdot \omega_0}{Q \cdot Q'(z) \cdot \omega_0^2} \right) \tag{4.5}$$

where $\omega_0'(z)$ and $Q'(z)$ are the fitted resonance frequency and quality factor, and ω_0 and Q are the resonance frequency and quality factor without interaction.

The found values for Z (Fig 4.6) show that the sensitivity on Z' is too low to accurately determine the expected electrostatic gradient. This is caused by the low quality factor, which make the fitting procedure insensitive to small shifts in the resonance frequency.

The measured dissipative interaction likewise does not find the theoretically expected values. While the correct $1/z$ scaling is found, there is a negative offset. This is explained by residual interactions, as the analysis demands $Z''(z) = 0$ at the starting distance of some 7 µm from the surface, while there still are residual interactions at this distance.

Fitting inverse of Z"(z)

A straightforward way of extracting the found viscosity and hydrodynamic zero position from the data is by plotting the inverse of the dissipative component $Z''(z)^{-1}$. Assuming that the

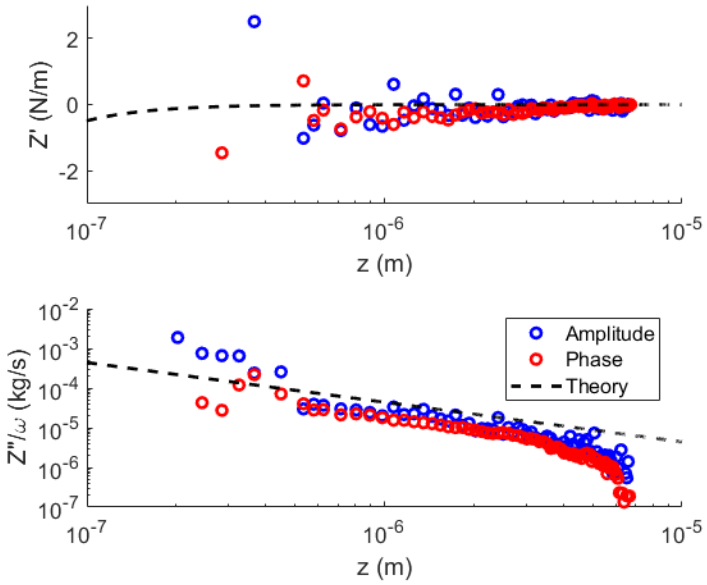

Figure 4.6: The two components of $\mathcal{Z}(z)$ as determined through equations (4.4) and (4.5) using capacitive excitation in PDMS oil. The measurement of $Z'(z)$ follows the electrostatic gradient as expected from the applied voltages, while the measurement of $Z''(z)$ finds the z^{-1} scaling expected from the Reynold's dissipation. The difference with the theoretically predicted values is likely due to residual interactions at the calibration distance of 5 µm from the surface.

dissipative interaction can be fully described by the Reynolds dissipative force, we can use the following expressions

$$\frac{Z''(z)}{\omega} = \frac{6\pi\eta R^2}{z - \Delta z} \tag{4.6}$$

$$\frac{\omega}{Z''(z)} = \frac{1}{6\pi\eta R^2} \cdot z - \frac{1}{6\pi\eta R^2} \cdot \Delta z \tag{4.7}$$

where Δz is the difference between the fitted zero position of the excitation strength $z'(z)$ and the zero position of the Reynolds force. As (4.7) has the shape of a first order polynomial $p(x) = ax + b$, this can be directly fitted to the inverse of the calculated values for $Z''(z)$ (Fig. 4.7). Data points within the first 300 nm of the surface were excluded from the fit, as within this range the excitation strength does not follow the analytical description.

The found value for the viscosity this way is $\eta = 0.0018$ Pas, which is roughly 2.5 times lower than the value of $\eta = 0.0046$ Pas indicated by the supplier. This disagreement is likely caused by the residual interaction at the calibration distance.

The difference in zero position Δz is found to be only +8.05 nm, which is very reasonable considering the low quality factor and resulting insensitivity to shifts in ω_0. A nanometric positive value is expected as the charges driving the capacitive excitation are buried below the surface oxide of the silicon.

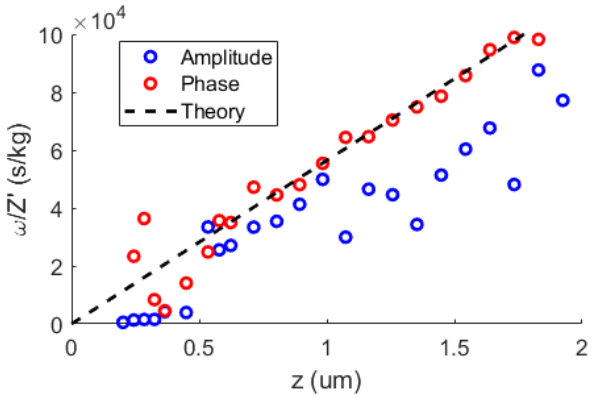

Figure 4.7: Plot of the inverse of $Z''(z)$ from both the amplitude and phase data, as determined from the variance in ω_0 and Q in PDMS oil using capacities excitation. The phase data is fitted with a line to determine the viscosity of the liquid, which is found to be 0.0018 Pas. Data within the first 300 nm was excluded from the fit.

Conclusions

It is clear that performing the measurement of $\mathcal{Z}(z)$ the 'classical' way by tracking the shape of the resonance under these conditions suffers from many limitations. While we have shown that the excitation strength follows theoretical considerations, the determination of $\mathcal{Z}$ leaves much to be desired.

Due to the low quality factor, the sensitivity to ω_0 is too low to measure the electrostatic gradient. Likewise, the large residual dissipative interaction between the probe and the surface at the calibration distance of 7 µm prohibits accurately determining the viscosity of the PDMS oil.

Due to the range of the scanner it is not possible to move further away from the surface for the calibration of the measurement. It would be possible to reduce the radius of the probe to decrease the lengthscale of the Reynolds dissipation, but it should be noted that this would also decrease the capacitive excitation strength. Alternatively a measuring method of which the sensitivity is less dependent on the quality factor of the lever could be used.

While there is some difference between the analytical description of the system and the experimental reality, these results demonstrate that capacitive excitation and the extraction of $\mathcal{Z}(z)$ at the resonance works on a conceptual level. The driving force is applied correctly and the resonant properties of the system can be extracted.

4.2.4 Methodology 2 - Amplitude-phase-distance data

Measurements using the second methodology that is described in chapter 3 were performed in 5 cSt PDMS oil as well. First the free parameters of the lever were determined by performing a calibration measurement at some distance from the surface and subtracting the theoretically expected probe-sample interaction. The amplitude and phase response is subsequently measured at a specific frequency as the probe-sample separation is decreases, after which the mechanical impedance $\mathcal{Z}$ is calculated from these observables.

Calibration

To determine the properties of the lever in absence of any interaction, the amplitude and phase response were measured under an excitation of $V_{AC} = 2$V and $V_{DC} = 0$V (Fig. 4.8) while far from the surface. The electrostatic and hydrodynamic interaction were subtracted using the procedure described in chapter 3 (Table. 4.3).

At the calibration distance of 16.17 µm, ω_0 is unaffected by the residual interaction, which is expected as the electrostatic gradient decays as z^{-2}. The Reynold's damping decays much slower as z^{-1} and at this distance is still damping the quality factor from its intrinsic value of 2.5537 to a value 1.57.

These intrinsic lever parameters were used to calculate the calibration parameters $F_r(z_0)$ and $\phi_\omega(z_0)$ at each frequency on which amplitude and phase data was measured through

$$\omega_0 = \sqrt{\omega_0'(z_c)^2 - \frac{k_{int}(z_c)}{m}} \tag{4.8}$$

$$\frac{m\omega_0}{Q} = \frac{m\omega_0'(z_c)}{Q'(z_c)} - \frac{\gamma_{int}(z_c)}{m\omega_0} \tag{4.9}$$

as derived in chapter 3.

Parameter	Fitted	Intrinsic
z (µm)	16.17	-
ω_0 (kHz)	25.17	25.17
Q	1.5737	2.5537

Table 4.3: Parameters fitted from the amplitude and phase data measured at 16.17 µm from the surface using capacitive excitation in PDMS oil with $V_{AC} = 2$V and $V_{DC} = 0$V. Substraction of the expected probe-sample interaction at this distance allow calculation of the intrinsic lever parameters.

Data channels

With the intrinsic parameters of the AFM lever determined, we can interpret the observables that will provide us with $\mathcal{Z}(z)$. To demonstrate the frequency independent nature of the measurement, amplitude and phase as a function of separation was measured at every 2 kHz interval between 4 and 30 kHz. For the sake of briefness, only the full data channels for the measurement at 20 kHz are presented (Fig. 4.9).

Curves are measured until the probe makes contact with the surface, visible through deflection of the lever in the W-piezo. This point is taken as the 0 position in all presented curves

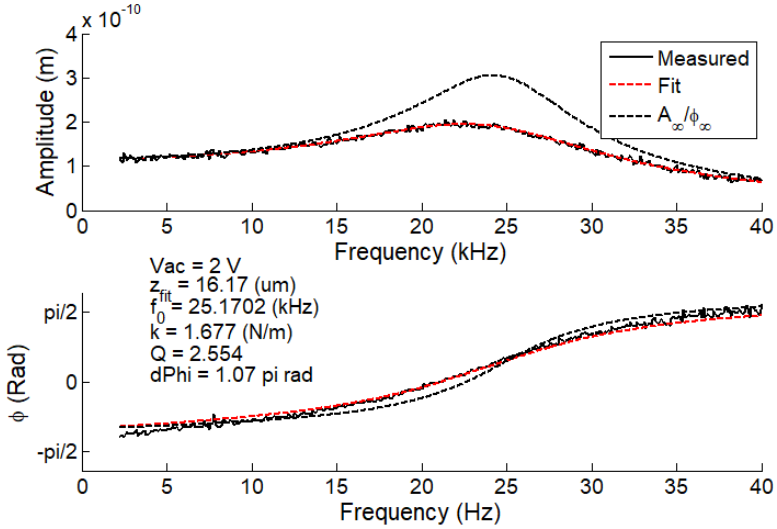

Figure 4.8: Calibration amplitude and phase data measured at 16.17 µm from the surface using capacitive excitation in PDMS oil with $V_{AC} = 2\text{V}$ and $V_{DC} = 0\text{V}$. The distance from the surface is determined by fitting the excitation strength (red dashes). The expected probe-sample separation is substracted to determine the calibration parameters (black dashes). The calibration parameters are plotted using the fitted excitation strength of 16.17 µm.

and used to determine the value of z in each point when calculating $n(z)$. $n(z)$ is subsequently determined from the amplitude curve and calibration parameters through

$$n(z) = \frac{1}{F_r(z_0)A_\omega(z)} \cdot \frac{1}{z} \tag{4.10}$$

where $F_r(z_0)$ is calculated from the intrinsic parameters of the lever as determined during calibration.

The components $Z'(z)$ and $Z''(z)$ are calculated using the equations derived in the previous chapter

$$Z'(z) = F_r(z_0)\left[n(z)\cos(\phi_\omega(z)) - \cos(\phi_\omega(z_0))\right] \tag{4.11}$$

$$Z''(z) = F_r(z_0)\left[n(z)\sin(\phi_\omega(z)) - \sin(\phi_\omega(z_0))\right] \tag{4.12}$$

where $F_r(z_0)$ and $\phi_\omega(z_0)$ are again determined from the calibration parameters.

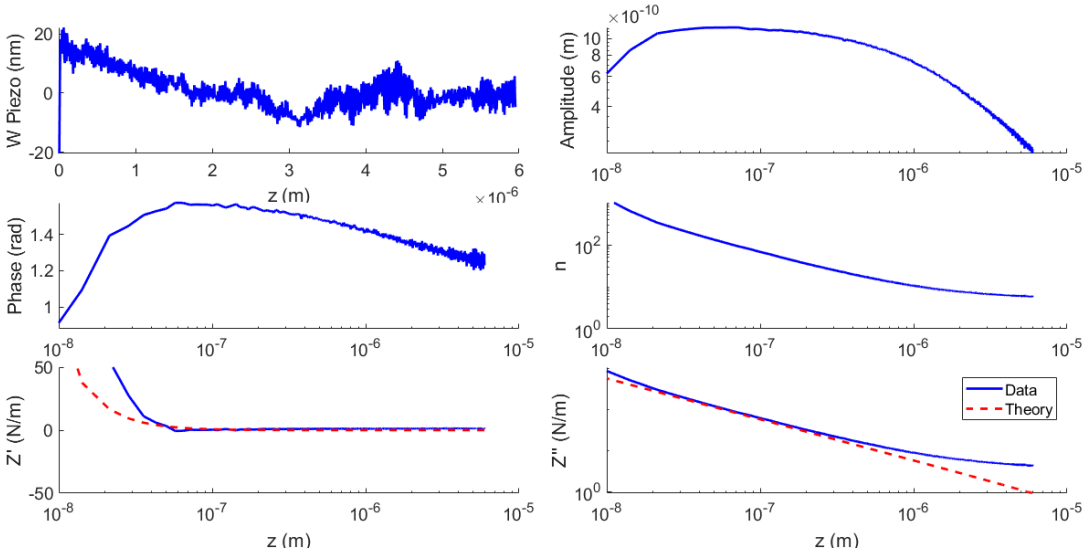

Figure 4.9: Deflection, amplitude and phase data measured at 22 kHz in PDMS oil using $V_{AC} =$ 2V and $V_{DC} = 0$V and corresponding calculated $n(z)$ and $\mathcal{Z}(z)$. The measurement of $Z''(z)$ closely follows the value predicted from the Reynold's dissipative force (red dashes), while below 100 nm $Z'(z)$ deviates strongly from the expected electrostatic gradient(red dashes).

Results for Z'(z)

As there is no additional conservative component to the probe-sample interaction aside from the gradient of the capacitive excitation force, the expected value for $Z'(z)$ is described by

$$Z'(z) = -\nabla f_0(z) = \frac{\pi\epsilon_0\epsilon_r R}{z^2}\left((V_{DC} - V_0)^2 + \frac{1}{2}V_{AC}^2\right) \tag{4.13}$$

where for the currently presented data $V_{DC} = 0$V, $V_0 \approx$ -0.3V and $V_{AC} = 2$V.

The found values for $Z'(z)$ deviate strongly from this expectation, as they vary with frequency, do not display the expected z^{-2} scaling and attain non-zero values at the calibration distance (Fig. 4.10). To quantify this deviation from the expected results, curves at each frequency were fitted on a lin-lin scale with a function of the form

$$Z'(z) = \frac{\pi\epsilon_r R}{(z - \Delta z_{Ele})^2} \cdot \left(V^2 + \frac{1}{2}V_{AC}^2\right) + dZ' \tag{4.14}$$

that describes the form of an electrostatic gradient. The fitting parameter are the zero position for the electrostatic gradient Δz_{Ele}, the potential difference V and a vertical shift dZ' introduced to accommodate the non-zero value at the calibration distance (Fig. 4.11).

From these fits it is apparent that the required voltages to produce the found results exceed multiple hundreds of volts (Fig. 4.11c). Such values are clearly unphysical, indicating that the deviation is the result of an error in the methodology. Likewise the offset per frequency shows a clear decreasing trend with frequency that is minimal around 25 kHz, the resonance frequency of the system.

Due to these indicators our current hypothesis is that this error in the measurement of $Z'(z)$ is due to a problem in the calibration of $\phi_\omega(z_0)$. While we currently see no direct way to confirm this hypothesis, it will be further substantiated in the following section by reproducing the found behavior in numerical simulations through introduction of a small error in $\phi_\omega(z_0)$.

For the application of the non-contact measurement this means that in its current form the conservative component of the mechanical impedance cannot be used to determine the transition length. The measurement of $Z'(z)$ appear to be too sensitive to errors in the calibration parameter $\phi_\omega(z_0)$.

Lastly the fitted values for the electrostatic zero were found to be surprisingly reasonable, with an average of value of -5.67 nm for well fitting curves. A slightly negative value should be expected as the zero position is taken in reference to the point of contact between the probe and the surface and the charges generating the electrostatic field are buried below the surface oxide of the silicon.

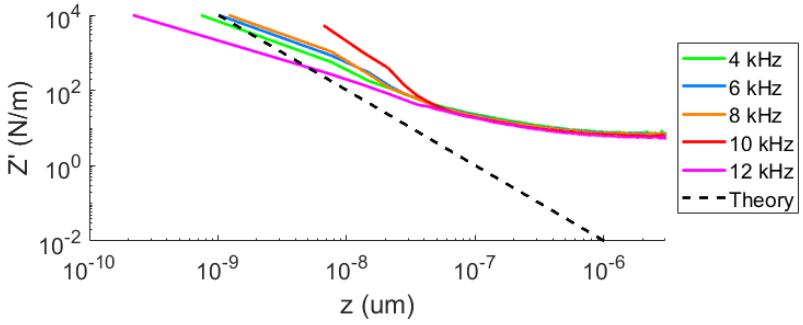

(a)

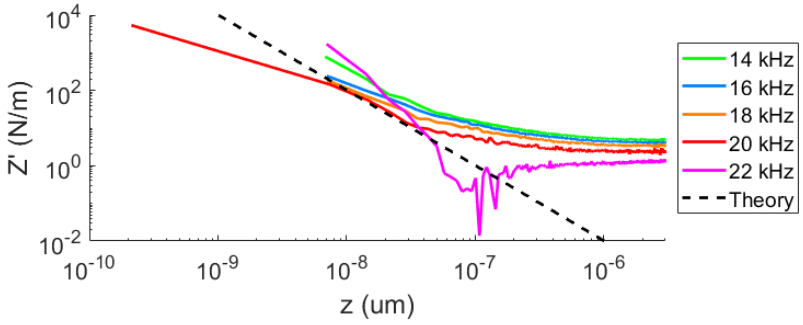

(b)

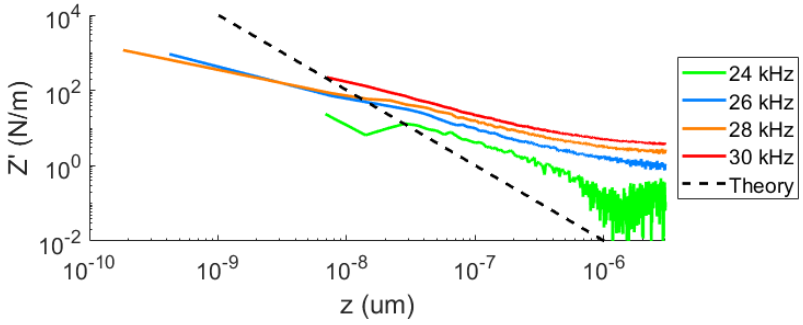

(c)

Figure 4.10: (a-c) Found values for $Z'(z)$ as measured at intervals of 2 kHz between 4 to 30 kHz using capacitive excitation in PDMS oil. The curves do not follow the values calculated for the electrostatic gradient through equation (4.13). Only close to the resonance frequency of 25 kHz do the curves approach the values from the electrostatic gradient expected under the applied voltages (black dashes). All measured curves take on a finite value at the calibration distance.

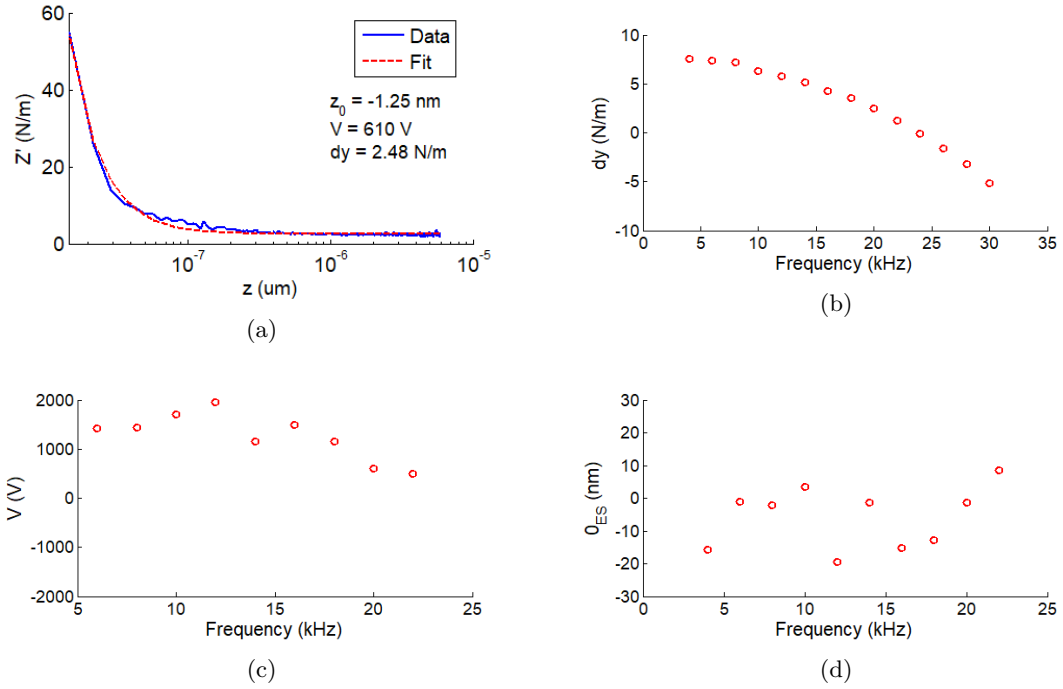

Figure 4.11: (a) Fitting of the $Z'(z)$ curve measured at 22 kHz using capacitive excitation in PDMS oil with the shape of an electrostatic gradient through equations (4.14). (b) Offset $dZ'(z)$ fitted for each frequency. The offset decreases with frequency and is smallest around the resonance frequency. (c) Applied voltage required to generate the measured result, which can be on the order of a 1000 V. This indicates the measured curves do not have a physical origin. Values exceeding 2000 V were omitted. (d) Zero position of the fitted electrostatic gradient. Even though the measurement of $Z'(z)$ deviate strongly from the expected electrostatic gradient, the zero position deviates only a few nanometers from 0.

Results for Z"(z)

In contrast to the determination of the conservative component $Z'(z)$, the found curves for the dissipative component $Z''(z)$ are close to the values expected from theory and consistent between the different explored frequencies (Fig. 4.12). While measurements at lower frequencies suffer from noise at large separations, above 10 kHz the found values closely follow the values predicted by the Reynold's dissipative force.

As explained for the classical measuring method in the previous section, a straightforward way of extracting the viscosity and hydrodynamic zero position is by plotting result as $Z''(z)^{-1}$ and fitting a first order polynomial (Fig. 4.13). The found values for the hydrodynamic zero above 10 kHz are distributed between -4 and -6 nm, with an average value of -4.38 nm (Fig. 4.13c). As such the distribution is very similar to the distribution found for the electrostatic zero in the previous section, and is not imcompatible with a silicon oxide layer of a few angstrom.

The viscosity values found this way above 10 kHz are consistent in between frequencies and have an average value of $5.2 \cdot 10^{-3}$ Pas, which is close to the range advertised by the supplier of $4.11 - 5.02 \cdot 10^{-3}$ Pas. (Fig. 4.13b) Below 10 kHz the found value is lower, possibly due to the worse signal-to-noise ratio at these frequencies.

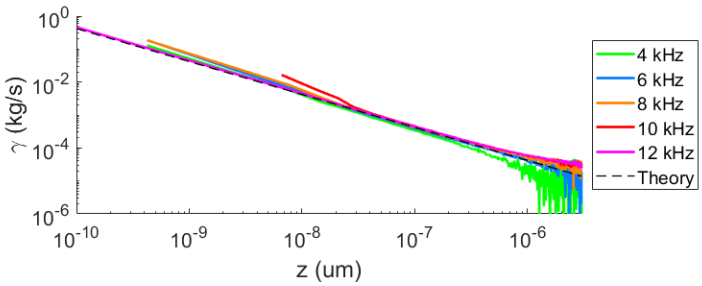

(a)

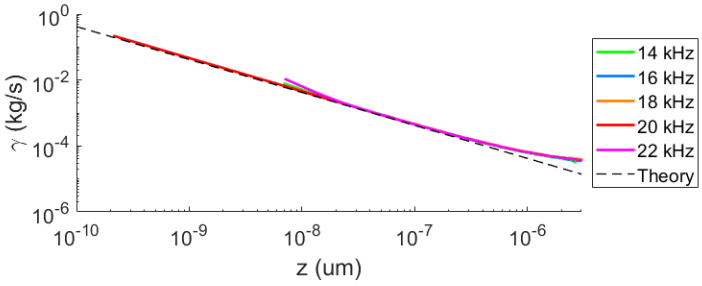

(b)

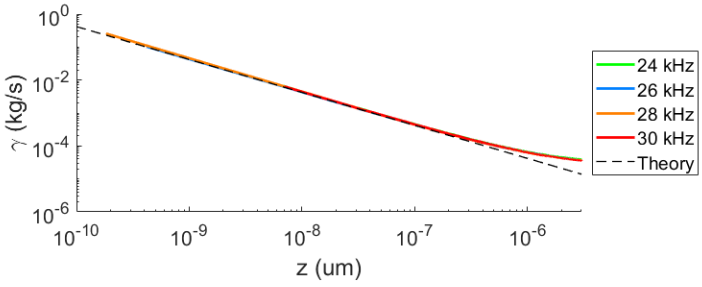

(c)

Figure 4.12: (a-c) Found values for $Z''(z)$ as measured at intervals of 2 kHz between 4 to 30 kHz using capacitive excitation in PDMS oil. In contrast to the measurement of $Z'(z)$, between 10 to 500 nm the curves closely follow the values predicted by the Reynold's dissipative force.

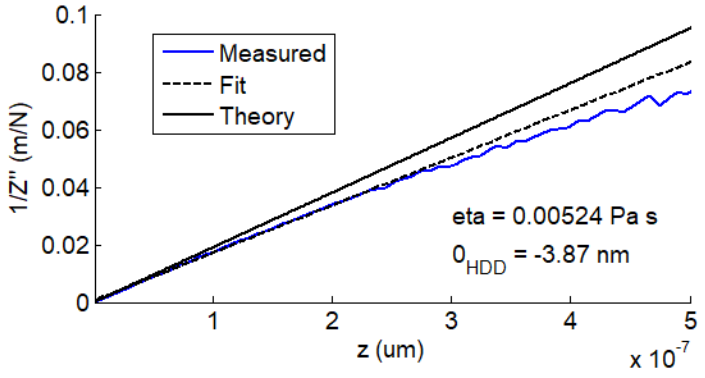

(a)

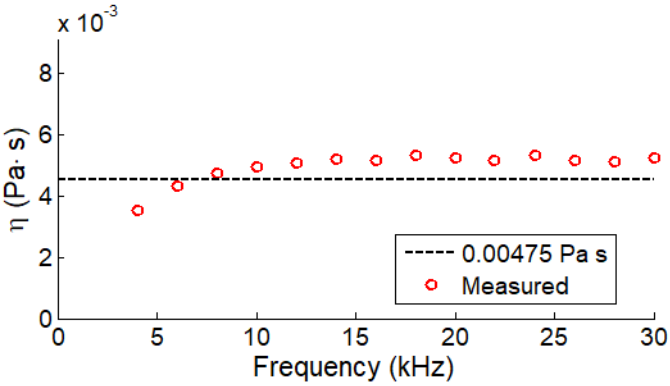

(b)

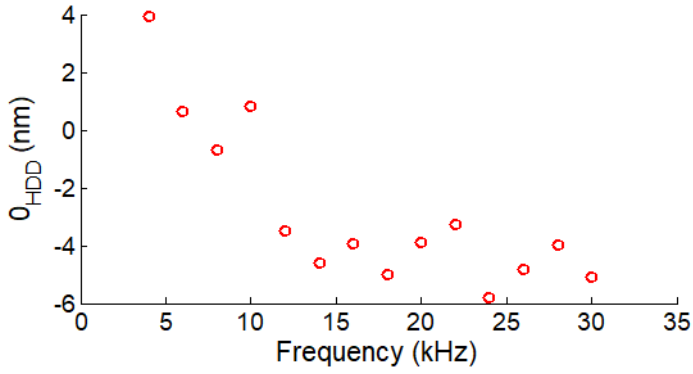

(c)

Figure 4.13: (a) Plot of $Z''(z)^{-1}$ as measured at 22 kHz using capacitive excitation in PDMS oil, fitted with a straight line on data within the 2 µm closest to the surface. (b) Fitted value for η per frequency. For frequencies below 10 kHz the viscosity is underestimated, while for higher frequencies provides a consistent value. (c) Fitted zero position for the Reynolds dissipative force. While measurements below kHz find positive values of a few nanometer, higher frequencies find a value of about -4 nm relative to the point of contact between probe and surface.

4.2.5 Conclusions

While there are some differences between the analytical description and the experiment in practice, the presented measurement in PDMS oil demonstrate that determination of the mechanical impedance using capacitive excitation is possible. We demonstrate that the dissipative part of the probe-sample interaction can reliable extracted over a broad range of frequencies.

The technique suffers from the difficulty that it has no direct access to the intrinsic resonant properties of the lever in absence of any interaction required for calibration. As an alternative the probe-sample interaction can be substracted from the measured response at large separations if the interaction is fully known at these distances.

Regardless, the conservative component of the interaction cannot be accurately determined, likely due to errors in the calibration of the parameter $\phi_\omega(z_0)$. This claim will be further substantiated in the following section using numerical simulations.

For the application of the non-contact measurement of mechanical properties in liquid this indicates that we should be able to accurately determine the dissipative component of the mechanical impedance up to a distance of 10 nm over a broad range of frequencies. This should be sufficient to determine the transition length in the 0.1 to 1 µm range, though the measurement will likely suffer in accuracy due to only one of the two components being available for fitting.

4.3 Numerical simulations

As demonstrated in the previous sections, the dissipative component of the interaction can be consistently determined between distances of 1 µm to 10 nm over a broad range of frequencies. The conservative part however displays strong deviations. We expect this is due to a high sensitivity to the calibration parameters. To substantiate these claims, the measurement was modeled in a numerical simulation to investigate the effect that small calibration errors on individual parameters can have on the found values for $\mathcal{Z}$.

These simulations indicated that due to numerical arguments, the measurement of $Z'(z)$ is highly sensitive to the calibration parameters $\phi_\omega(z_0)$, which due to the nature of capacitive excitation is difficult to determine. It is also sensitive to errors in $\phi_\omega(z)$ due to other numerical reasons.

4.3.1 Method

The numerical simulations were performed by generating a data using parameters representing the real system. As in the real measurement, a calibration curve is generated at a finite separation, from which the assumed probe-sample interaction have to be subtracted to find the intrinsic response of the lever. The generated data is analyzed using the procedure described in chapter 3 as normal. Calibration errors can be simulated by taking small differences between the parameters used to generate and analyze the data. Parameters were used that closely resemble the experiment presented in the previous section (Table 4.4).

Parameter	V_{DC} (V)	V_0 (V)	V_{AC} (V)	Q	f_0 (kHz)
Value	0	-0.3	2	2.55	25.23
Parameter	k (N/m)	R (µm)	η (Pa · s)	ϵ_r	z_0 (µm)
Value	1.67	22.06	$4.5{\cdot}10^{-3}$	2.59	10

Table 4.4: Set of parameters used to generate the numerical simulation data that closely resemble the parameters of the measurement in 5 cSt PDMS oil.

The probe-sample interaction was assumed to be fully described by

$$k_{int}(z) = \frac{\pi\epsilon_0\epsilon_r R}{z^2}\left((V_{DC}-V_0)^2+\frac{1}{2}V_{AC}^2\right) \tag{4.15}$$

$$\gamma_{int}(z,\omega) = \frac{6\pi\eta R^2\omega}{z} \tag{4.16}$$

The zero position for the electrostatic interaction and the hydrodynamic interaction were thus assumed to coincide with the physical surface of the substrate. Using these interactions, the amplitude and phase response at each separation is determined through

$$f_{2\omega}(z) = \frac{1}{2}\frac{\pi\epsilon_0 R}{z}V_{AC}^2 \tag{4.17}$$

$$A(z,\omega) = \frac{f_{2\omega}(z)}{\sqrt{(k_c(z)+k_{int}(z)-m\omega^2)^2+(\gamma_c(z)+\gamma_{int}(z))^2\omega^2}} \tag{4.18}$$

$$\phi(z,\omega) = \arccos\left(\frac{(\gamma_c(z)+\gamma_{int}(z))\omega}{\sqrt{(k_c(z)+k_{int}(z)-m\omega^2)^2+(\gamma_c(z)+\gamma_{int}(z))^2\omega^2}}\right) \tag{4.19}$$

These generated amplitude and phase curves are analyzed using the methodology described in chapter 3 and both $Z''(z)$ $Z'(z)$ can be calculated.

4.3.2 Results

When the same parameters are used to generate and analyze the data, the correct values for $\mathcal{Z}$ are found at any distance. This confirms that no mistakes were made in applying the methodology of the measurement in the numerical simulation.

The variation of the found results under a variety of calibration errors were simulated, including errors up to in 10% in k, R, η, ϵ_r and combinations of these parameters. Such calibration errors resulted in rescaling of the data on both the conservative and dissipative components, but did not reproduce the behavior found in the experiment.

To replicate the results found in the experiment, the calibration parameter $\phi_\omega(z_0)$ must be shifted by a small value, in this case chosen to be between -0.02 and 0.02 radians. Note that the size of this shift is much smaller than the change in $\phi_\omega(z_0)$ created by the substraction of the residual interaction at the calibration distance, which is on the order of 0.1 radians. This relatively small calibration error has large effects on the found curve for $Z'(z)$ (Fig. 4.14).

The power law scaling decreases and the curve takes on a finite value at the calibration distance, comparable to what is found in the experiment. The found curve for $Z''(z)$ remains virtually unchanged, which is likewise in agreement with the experiment. This effect remained consistent for varying frequencies, with the divergence from theoretical results occurring closer to the surface for higher frequencies (Fig. 4.15).

At first it might seem unexpected that a small calibration error has such a large effect on the conservative component while leaving the dissipative component virtually unchanged. The reason for this is found in the phase components of the equations for $\mathcal{Z}$: $\cos(\phi_\omega(z))$ for the conservative component and $\sin(\phi_\omega(z))$ for the dissipative. At a distance of about 10 nm to 1 µm from the surface, exactly the range that is most important for the non-contact determination of mechanical properties, we see that $\phi_\omega(z) \approx \pi$, and thus $\cos(\phi_\omega(z)) \approx 0$ while $\sin(\phi_\omega(z)) \approx 1$.

Using this approximation to rewrite our equations for the components of $\mathcal{Z}$, we find

$$Z'(z) \approx -F_r(z_0)\left[\cos(\phi_\omega(z_0)) + \frac{\nabla f_0(z)}{F_r(z_0)}\right] \tag{4.20}$$

$$Z''(z) \approx F_r(z_0)\left[n(z) - \sin(\phi_\omega(z_0))\right] \tag{4.21}$$

We can equally see that within this range for $Z''(z)$, $n(z)$ quickly exceeds values of 100, while $\sin(\phi_\omega(z_0))$ cannot exceed 1. Thus we can further approximate

$$Z'(z) \approx -F_r(z_0)\cos(\phi_\omega(z_0)) - \nabla f_0(z) \tag{4.22}$$

$$Z''(z) \approx F_r(z_0)n(z) \tag{4.23}$$

We can thus see that under these specific probe-sample interactions and within these distances from the surface, the measurement of $Z'(z)$ is predominantly determined by the calibration parameters. As such, a small error in the calibration parameter $\phi_\omega(z_0)$ has large effects on the values found.

As previously discussed, the nature of capacitive excitation makes it impossible to perform a calibration without residual interactions. These residual interactions must instead be subtracted from the calibration measurement to determine the intrinsic properties of the lever. Any imperfections in the assumed probe-sample interaction, such as a deviation in the viscosity or the relative permittivity of the liquid, will inevitably lead to small calibration errors in $\phi_\omega(z_0)$.

Additionally it should be noted that the $cos(\phi_\omega(z)) \approx 0$ term creates an additional numerical problem in the expresion for $Z'(z)$. It appears in the expression as a term $cos(\phi_\omega(z)) \cdot n(z)$, where the cosine is close to zero while $n(z)$ can be on the order of 10^4. In this multiplication of a small number with a much larger one, small errors in the determination of $\phi_\omega(z)$ can be magnified through $n(z)$ by multiple orders of magnitude.

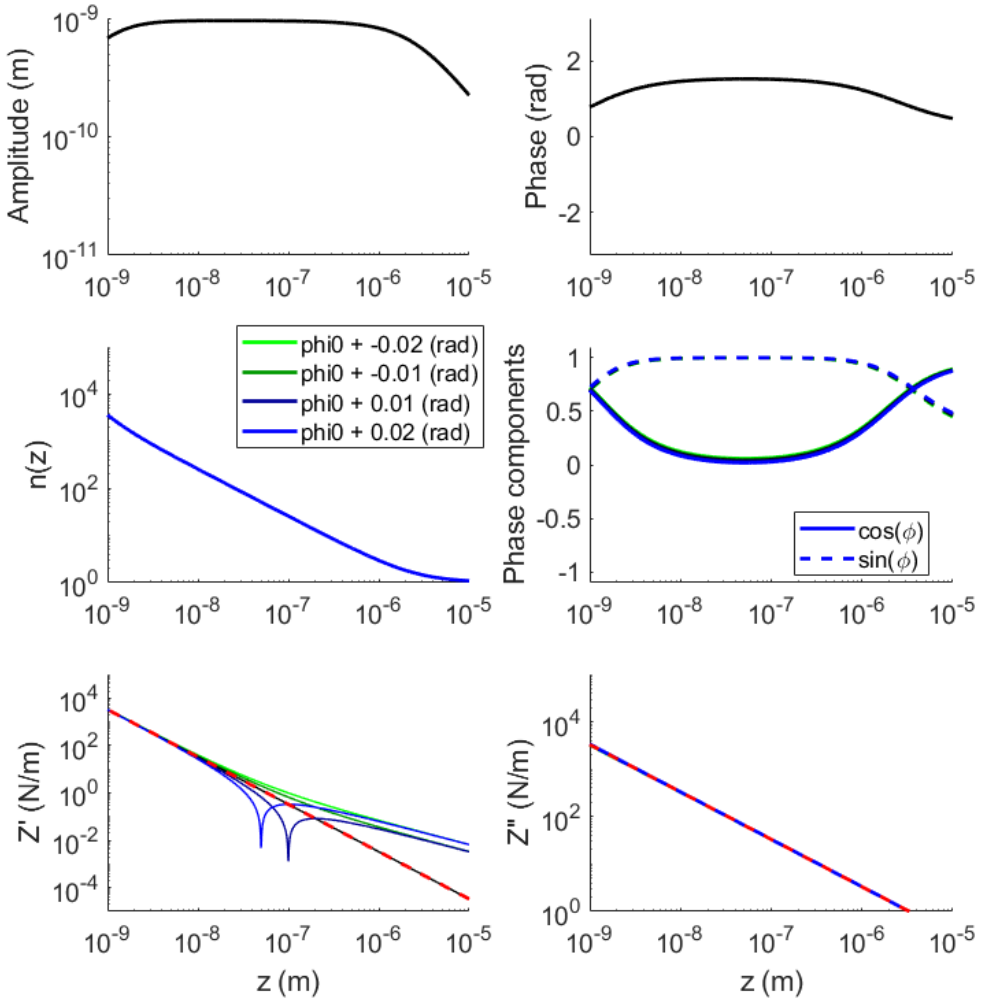

Figure 4.14: Numerically simulated data for capacitive excitation in liquid at $\omega = 0.5\omega_0$ using the parameters given in table 4.4. Black curves represent the case of perfect calibration, while the other curves include a small calibration error in $\phi_\omega(z_0)$ as indicated in the legend. These errors create large deviations in the calculated value for $Z'(z)$, qualitatively reproducing the scaling found in the experiment, while leaving $Z''(z)$ virtually unchanged.

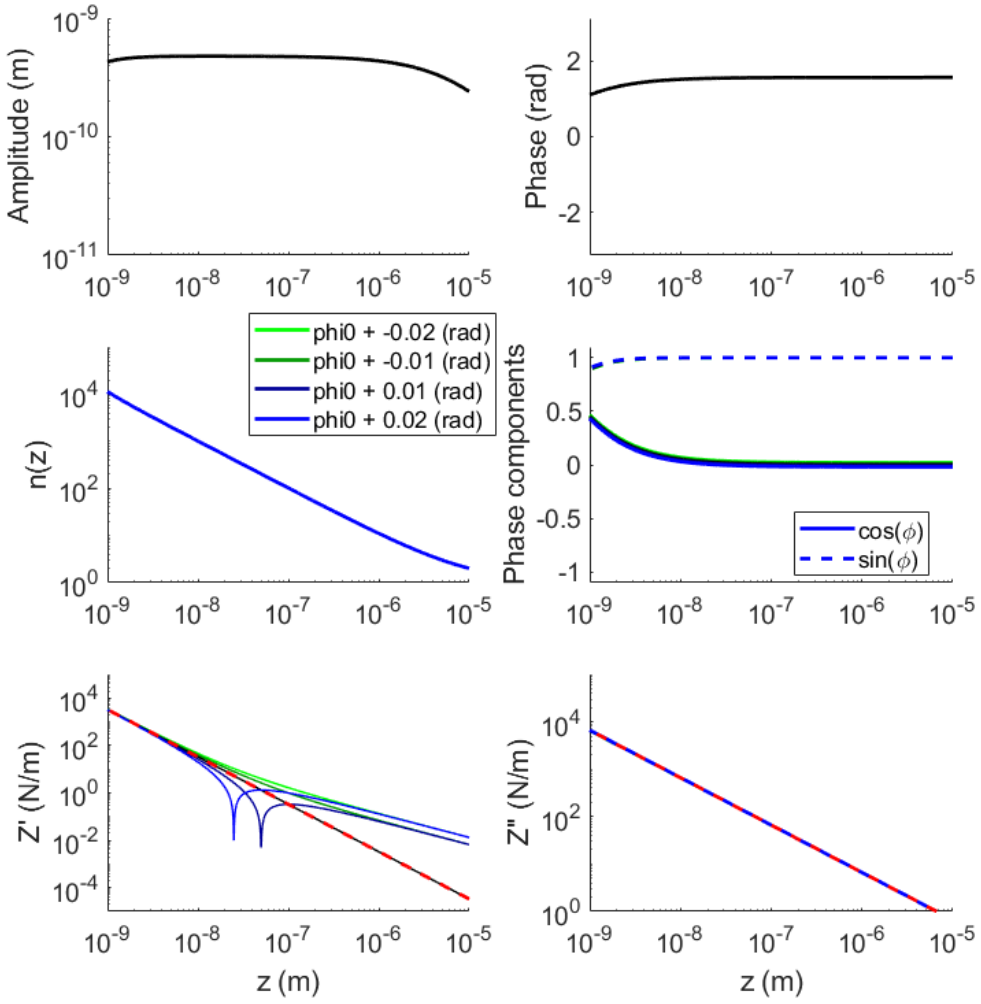

Figure 4.15: Numerically simulated data for capacitive excitation in liquid at $\omega = \omega_0$ using the parameters given in table 4.4. Black curves represent the case of perfect calibration, while the other curves include a small calibration error in $\phi_\omega(z_0)$ as indicated in the legend. These errors create large deviations in the calculated value for $Z'(z)$, qualitatively reproducing the scaling found in the experiment, while leaving $Z''(z)$ virtually unchanged.

4.3.3 Conclusions

The numerical simulations make clear why the determination of $Z'(z)$ from the observables $A_\omega(z)$ and $\phi_\omega(z)$ is so imprecise while the determination of $Z''(z)$ is accurate. The curve for $Z'(z)$ strongly depends on the calibration parameters $\phi_\omega(z_0)$, which due to the nature of capacitive excitation cannot be accurately determined. In addition to this, small errors in the $\cos(\phi_\omega(z))$ are multiplied by the large $n(z)$ term.

From these considerations we conclude that the difficulty in accurately determining $Z'(z)$ for this specific probe-sample interaction is inherent to the methodology. While improvements in the accuracy of the calibration and the overall sensitivity of the measurement may diminish these effects, it is unlikely that they will be completely resolved.

These numerical complications are a result of an unfortunate combination of capacitive excitation and the probe-sample interaction investigated. For other probe-sample interactions it is not a necessary truth that $\cos(\phi_\omega(z)) \approx 0$ and these deviations of $Z'(z)$ might be avoided.

4.A Measuring $\mathcal{Z}$ using piezo-acoustic excitation

As a precursor to the currently presented results, it was attempted to measure the mechanical impedance of the probe sample interaction using piezo-acoustic excitation on a commercial AFM. The results of this attempt are presented in brief form to substantiate the claim that piezo-acoustic excitation does not suffice when performing this measurement.

4.A.1 Materials

The measurements were performed on a commercial Bruker Dimension ICON AFM, made available by the CIME nanotech. The AFM has an optical beam deflection (OBD) detection system as explained in chapter 2.

Measurements were performed on a reticulated PDMS surface with a stiffness of about 2 MPa submerged in deionized water.

Colloidal AFM probes were used, created using the protocol described in section 2.8. The radius of the probe was determined before each measurement using optical microscopy. The stiffness of the lever was calibrated by measuring the Brownian Motion in water as explained in section 2.6.

4.A.2 Methods

Extracting the mechanical impedance from OBD data is not as straightforward as for the interferometric detection scheme. The position of the lever is not measured directly, but inferred from its deflection. If the base of the lever is moving significantly, as is the case for piezo-acoustic excitation in liquid, the measured deflection and the positional motion of the lever do not directly correspond to each other and a correction needs to be made. [131] Additionally, the motion of the piezo creates acoustic waves in the liquid that add an out of phase component to the driving force.

The methodology used to describe this complication is based on a publication by Maali et.al. [71] We describe the equation of motion for the lever end using the total driving force F_d through

$$m\ddot{x} + \gamma_c \dot{x} + k_c x = F_d \tag{4.24}$$

where γ_c and k_c are the dissipation and stiffness of the lever, respectively, and

$$F_d = (F_1 + iF_2)e^{i\omega t} \tag{4.25}$$

where the F_1 component is in phase with the base motion and the F_2 component is in phase quadrature. By combining these two equations, we express F_1 and F_2 in the measured motion of the lever when free from any interaction. Taking the ansatz $x(t) = Ae^{i(\omega t+\phi)}$ we find

$$F_1 = Ak_c \left[\left(1 - \left(\frac{\omega}{\omega_0} \right)^2 \right) \cos\phi - \left(\frac{\omega}{\omega_0 Q} \right) \sin\phi \right] \tag{4.26}$$

$$F_2 = Ak_c \left[\left(1 - \left(\frac{\omega}{\omega_0} \right)^2 \right) \sin\phi + \left(\frac{\omega}{\omega_0 Q} \right) \cos\phi \right] \tag{4.27}$$

with ω_0 the resonance frequency, Q the quality factor and k_c the stiffness of the lever.

If the amplitude of oscillation is small compared to the gradient of the interaction force, the interaction force can be linearised into a conservative ($-k_{int} \cdot x$) and dissipative ($-\gamma_{int} \cdot \dot{x}$) term. Writing out the instantaneous lever position $x(t) = d(t) + A_b e^{i\omega t}$, where $d(t)$ is the deflection of the lever and A_b the oscillating piezo displacement, our equation of motion including the interaction becomes

$$m\ddot{d} + (\gamma_c + \gamma_{int})\dot{d} + (k_c + k_{int})d = (F_1 + iF_2)e^{i\omega t} - (k_{int} + i\omega\gamma_{int})A_b e^{i\omega t} \tag{4.28}$$

Taking the ansatz $d(t) = Ae^{i(\omega t+\phi)}$ and some rewriting, we can separate the real and imaginary components. Defining the dimensionless ratios $\tilde{A} = \frac{A}{A_b}$ and $\tilde{F}_i = \frac{F_i}{F_d} = \frac{F_i}{k_c A_b}$ we find

$$\frac{\omega\gamma_{int}}{k_c} = \frac{\tilde{F}_1\left(1 + \tilde{A}\cos\phi\right) - \tilde{A}\left(\tilde{F}_2 + 1 - \left(\frac{\omega}{\omega_0}\right)^2\right)\sin\phi - \tilde{A}\frac{\omega}{\omega_0 Q}\left(\tilde{A} + \cos\phi\right)}{1 + \tilde{A}^2 + 2\tilde{A}\cos\phi} \tag{4.29}$$

$$\frac{k_{int}}{k_c} = -1 + \left(\frac{\omega}{\omega_0}\right)^2 + \frac{\tilde{F}_1\left(1 + \tilde{A}\cos\phi\right) + \tilde{A}\left(\tilde{F}_2 + \frac{\omega}{\omega_0 Q}\right)\sin\phi + \left(1 + \tilde{A}\cos\phi\right)\left(1 - \left(\frac{\omega}{\omega_0}\right)^2\right)}{1 + \tilde{A}^2 + 2\tilde{A}\cos\phi} \tag{4.30}$$

$$\tag{4.31}$$

Thus by determining F_1, F_2, A_b, k_c, ω and Q for our system and measuring A and ϕ as a function of probe-sample separation z, we determine $k_{int}(z)$ and $\gamma_{int}(z)$ at arbitrary frequency.

4.A.3 Results

The measured resonance curve of the lever was in large parts obscured by parasitic resonances (Fig. 4.16a). The visible part of the resonance was fitting using a harmonic oscillator model to extract the resonance frequency (5.6 kHz), piezo displacement (0.4 nm) and quality factor (3.4). Using these values the driving force per frequency was calculated through equation (4.26) (Fig. 4.16b).

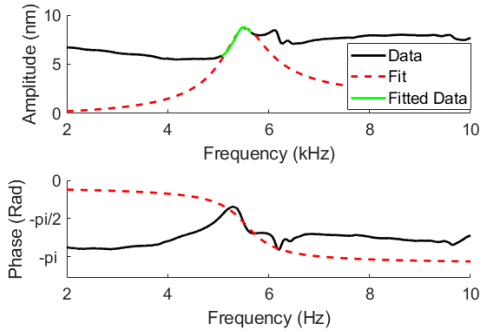

(a)

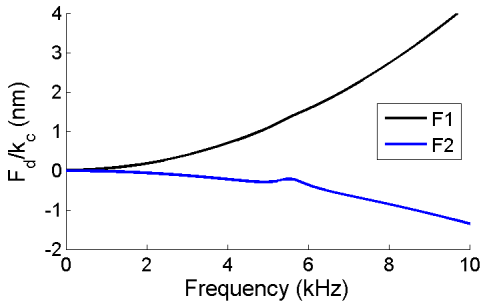

(b)

Figure 4.16: (a) Amplitude and phase response of the probe without interaction, measuring using piezo-acoustic excitation in deioinized water. (b) Driving force calculated from the fitted resonance frequency, quality factor and piezo displacement using equation 4.26.

Amplitude and phase data was measured at 250 Hz intervals between 5 and 6.5 kHz. For brevity only the data at 5.25 kHz is shown (Fig. 4.17). k_{int} and γ_{int} were caculated from the

measured amplitude and phase response as a function of separation using equations (4.29) and (4.30).

None of the resulting curves for Z' and Z'' followed the behavior expected for the non-contact measurement as presented in chapter 1. While the found values did saturate close to the surface for some frequencies, the scaling in the dissipative region (far from the surface) was found to be incorrect for all of the investigated frequencies (Fig. 4.18).

This demonstrates that due to the presence of parasitic resonances in the system, it is not possible to accurately determine the resonant properties of the lever under interaction with the surface, and that it is not possible to extract the mechanical impedance $\mathcal{Z}$ of the probe-sample interaction without removing such peaks from the system.

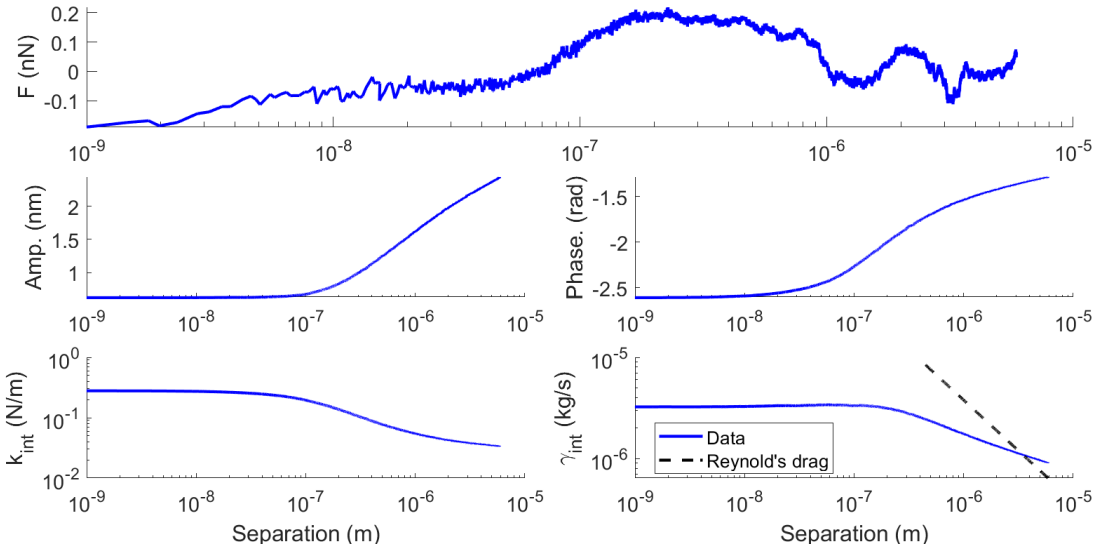

Figure 4.17: Force, amplitude and phase data measured as a function of probe separation at 5.25 kHz using piezo-acoustic excitation in deionized water. Using these values and equations (4.29) and (4.30), k_{int} and γ_{int} can be calculated. Neither curve follows the scaling expected from the non-contact measurement.

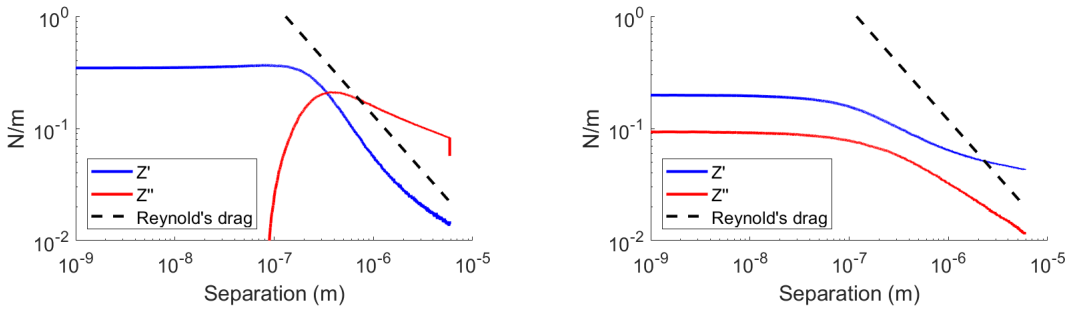

(a) (b)

Figure 4.18: Components of $\mathcal{Z}$ measured at (a) 5.25 kHz and (b) 5.5 kHz using piezo-acoustic excitation in deionized water. While the found values do saturate close to the surface in some cases, they do not follow the expected scaling.

Chapter 5

Capacitive excitation in deionized Water

Contents

5.1 Introduction

As indicated in the introduction to this manuscript, an important application of the non-contact determination of mechanical properties on soft condensed matter is soft biological matter such as cell tissue. As buffer fluids for biological tissue are water based, water is an especially important fluid to perform the measurement in. To further explore the possibilities of using capacitive excitation to perform a non-contact measurement of mechanical properties, it was thus attempted to use capacitive excitation in deionized water.

Water is not a dielectric liquid, but is conducting and has electronic properties that strongly depend on the dissolved ionic content. When charges are present on a surface in water it will attract dissolved ions of opposite charge that screens the electric potential. This leads to the formation of an electric double layer structure, where a layer of oppositely charged ions cover the surface, followed by a diffusive layer with an exponentially decaying combined potential. [132–134]

At first order we will attempt to ignore such surface effects and interpret the response of the system in water as-if it was a dielectric liquid. While the use of deionized water attempts to lend some credibility to this description, it should be noted that deionized water still has trace ionic contents. For probe-sample separations below a few hundreds of nanometers, the electronic double layer structures on both electrodes will interact and will require a more complicated description of the system.

We will show that, while we can excited the probe in deionized water using an AC electric field, the driving force does not follow the description for a dielectric liquid. It is thus not possible to perform a measurement of $\mathcal{Z}(z)$ using the measured amplitude and phase response at specific frequency. The shape of the resonance however is independent of the driving force, as explained in chapter 3, making it possible to obtain information on $\mathcal{Z}$ at the resonance frequency in water by measuring the change in ω_0 and Q the lever as a function of probe-sample separation.

5.2 Materials

Measurements were performed using similar materials as those in PDMS oil, with the key difference being the use of deionized water and a silicon substrate with a thermally grown oxide layer.

5.2.1 Colloidal probe

Two colloidal probes were used for the measurements in water presented in this section. Both were created using the protocol in section 2.8. The stiffness of both levers was determined by measuring their Brownian motion in air as explained in section 2.6 (Table 5.1). The sphere radius was determined using optical microscopy.

Measurement	R (µm)	k_c (N/m)	ω_0 (kHz)	Q
Excitation and Stability	22.85	3.88	43.38	344
Methodology I	22.59	1.713	39.71	304

Table 5.1: Properties of the levers used in this chapter per measurement, as determined from their Brownian motion in air.

5.2.2 Substrate

A [100]-orientation silicon wafer is used as a rigid substrate. This semiconductor has a p-type doping to ensure it is conducting, with a resistivity of 0.2 to 0.4 Ω/cm^2. The wafers used had a thermally grown oxide layer with a thickness of 400 nm as indicated by the supplier.

5.2.3 Deionized water

The water used in the experiment was MiliQ ultrapure water with a resistivity of 8.2 MΩcm. The properties of deionized water are listed in table 5.2.

The refractive index n of water is approximately 1.33, decreasing the effective wavelength of the laser light to $\lambda' = \frac{\lambda}{n} = 500\text{nm}$ and increasing sensitivity of the fiber optical detection system by a factor of n. As for PDMS oil, the closer matching between the optical index of the optical fiber glass and the liquid decreases the light reflected at the fiber-water interface to 0.3% compared to 4% for a fiber-air interface, reducing sensitivity of the measurement by a factor of 13. With these two contributions combined the sensitivity of the optical fiber detection system decreases by a factor of 10.

	Deionized water
Kin. Viscosity ν	0.89 cSt
Dyn. Viscosity η	$8.3 \cdot 10^{-4}$ Pas
Density ρ	1 g/mL
Refraction index n	1.33
Dielectric constant e_r	60-80
Resisitivity	8.2 MΩcm

Table 5.2: List of the properties of deionized water relevant to the presented measurement.

When measured using microwave waveguide interferometry, deionized water has a dielectric constant (ϵ_r) with a bulk value of 80 to 90 and a loss constant of 0.25 to 1 in the 10 to 100 kHz range. [135] The bulk dielectric constant decreases with the addition of ions, though it remains above 60. [136] As these values are more than 20 times higher than for PDMS, application of (4.1) would predict much a larger excitation strength in water than in PDMS oil.

However, these values found through microwave interferometry are insensitive to screening by ions present in the water. It is likely that the electric field generated by the charges in the conducting surfaces used in the experiment will be partially screened and a lower effective dielectric constant is found.

5.2.4 Electrochemisty in deionized water

As water is a conducting material and we are applying a potential difference, there is the possibility of electrons being liberated from the surface of the electrodes which can drive electrochemical reactions. Such reactions could occur in the water, or between the water and electrode material. The reactions most likely to occur are the splitting of water into oxygen and hydrogen, and the formation of silicon oxide on the silicon wafer. No reaction should take place on the colloidal probe as the combination of gold and water is chemically inert under the conditions explored.

Depending on the sign of the applied voltage, the splitting of water into hydrogen and

oxygen could occur on either electrode, following the chemical equation

$$2\,H_2O\,(l) \longrightarrow 2\,H_2(g) + O_2(g)$$

While the precise potential required for this reaction depends on the pH of the water, the minimal potential difference at 25^oC and 1 atm is -0.8277 V. [137] To minimize the possibility of electrolysis, the combined AC and DC component of the potential difference should remain below this value.

On the side of the silicon wafer it is possible to thicken the native oxide layer through the reaction

$$Si\,(s) + 2\,H_2O\,(l) \longrightarrow SiO_2(s) + 4\,H^+ + 4\,e^-$$

For which the minimal potential difference at 25^oC and 1 atm is -0.91 V. [137] To minimize the possibility of an uncontrolled increase of the local silicon oxide layer thickness, silicon with a thicker thermally grown oxide layer was used instead of a native oxide layer.

It should be noted that these considerations do not paint the whole picture. The preceding cases assume two conducting electrodes, while in our system the silicon wafer electrode is an isolator. This may increase the potential required to drive electrochemical processes. It was recently discovered that small gap sizes enhance the electrolysis of water due to overlapping of the electric double layers. [138] It is unclear what effect such phenomena have on the measurement. As such the numbers mentioned here should only be considered a framework to help interpret the measurement at hand.

5.3 Capacitive excitation in water

To investigate the effectiveness of capactive excitation in water, the AFM lever was excited using both the first and second harmonic. It is attempted to interpret these results using the description for dielectric fluids as described in chapter 3.

While ideally voltages below 0.8 V would be used to avoid electrochemistry, such low excitation strengths did not always create sufficient excitation to accurately determine the lever response. Thus for the first demonstration of the amplitude and phase response on the first and second harmonic, higher excitation voltages were used.

After these measurements, a white residue was visible on the silicon surface in a shape featuring the shape of the probe, likely resulting from electrochemical reactions. The precise nature of this residue was not further investigated. No such residue was visible after measurements where the total applied voltage remained below 0.8 V.

5.3.1 1st Harmonic

The amplitude signal produced on the first harmonnic of the excitation was found to be unstable (Fig. 5.1a). The measured amplitude would achieve a stable value when an AC voltage is aplied, but fluctuate significantly as frequency is varied. While higher AC voltages did produce a larger amplitude response, the found values could inconsistently fluctuate over an order of magnitude when varying frequency.

A possible explanation for this inconsistent behavior may be the dependency of the driving force f_ω on the DC potential between the two surfaces. Trace ions in the water may intermittently screen the applied potential and create an inconsistent driving force.

5.3.2 Determination of V_0

As for the measurements in PDMS oil, it was attempted to determine V_0 as a function of probe-sample separation by sweeping V_{DC} and following equation 4.1 finding the point at which $V_{DC} = V_0$ and thus $A_\omega = 0$. An excitation voltage of $V_{AC} = 2V$ was applied, sweeping V_{DC} over a range of 1 V each 500 nm increment of separation z (Fig. 5.1b).

It was found that while the amplitude curve does exhibit a minimum, no point with $A_\omega = 0$ exists for all values of z. Only when within 500 nm of the sample surface does A_ω tend to zero for a value of $V_{DC} = 0.3V$. It should further be noted that the slope of $A_\omega(V_{DC})$ is not symmetric around the minimum and saturates for values of $V_{DC} - V_0$ exceeding 0.7 V.

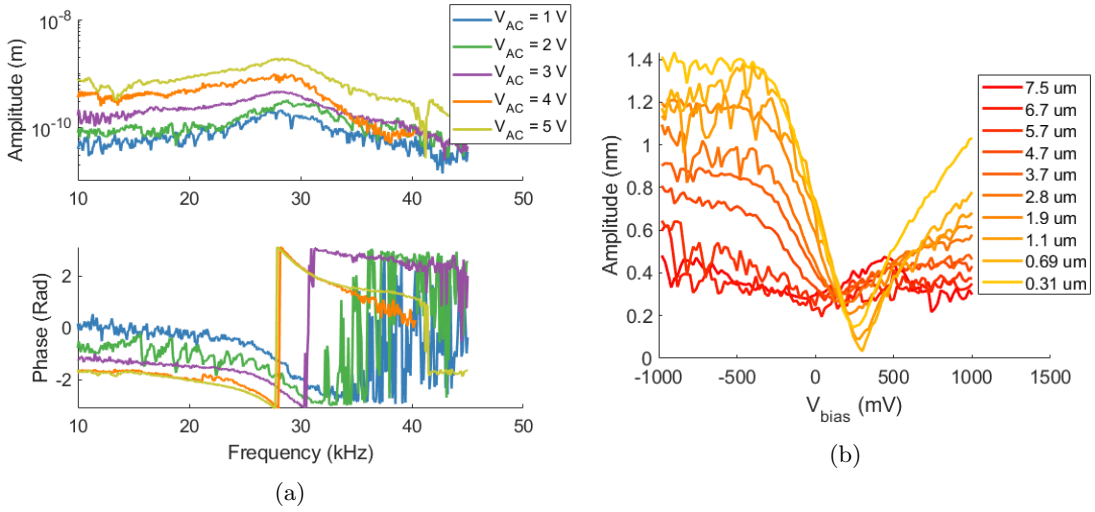

(a) (b)

Figure 5.1: (a) Measured amplitude and phase response for various excitation strength while exciting using the first harmonic in deionized water. Both the measured amplitude and phase curves demonstrate non-smooth behavior. (b) Measured amplitude at the resonance frequency as a function of V_{bias} for various probe-sample separations. In contrast to the case of dielectric liquids, the curves do reach $A_\omega = 0$ for all probe-sample separations.

It is clear that while the probe can be excited, equation 4.1 does not generally hold for capacitive excitation in water using the first harmonic. The model of a capacitor filled with a dielectric medium breaks down for water and at best may hold in the limit of small separations and small voltages.

5.3.3 2nd Harmonic

Despite the erratic behavior of the amplitude response on the first harmonic, the response for the second harmonic was relatively well behaved (Fig. 5.2a). While there were fluctuations in the measured amplitude, the resonant response of the lever is clearly visible. In contrast to the 1st harmonic, the phase response followed the analytical description regardless of the excitation voltage used.

The measured amplitude at the resonance frequency as a function of excitation strength followed the V^2 scaling expected for capacitive excitation using the second harmonic. A small drift in the phase response is visible, likely due to a shift in the resonance frequency from the increasing electrostatic gradient.

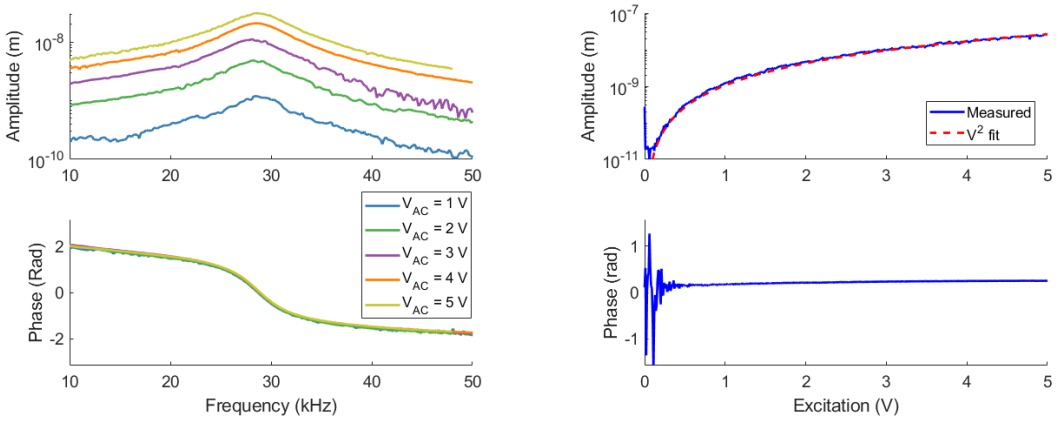

(a) (b)

Figure 5.2: (a) Measured amplitude and phase response in deionized water for various excitation strengths as measured on the second harmonic. (b) Measured amplitude and phase response on the second harmonic as a function of excitation strength close to the resonance frequency. The amplitude response follow the expected V^2 scaling.

5.4 $\mathcal{Z}$ through resonant properties

The consistent results for the excitation using the second harmonic indicate that the problem with using the first harmonic lies with the V_0 potential term. Using the second harmonic the resonant properties of the lever are clearly measurable, allowing for investigation of the mechanical impedance of the interaction at the resonance frequency as a function of probe sample separation z.

To prevent electrochemical reactions from affecting the measurement, an AC voltage of 0.7 V was used while the DC component was left at 0. The amplitude and phase response was swept at 100 nm intervals until the probe made contact with substrate, as indicated by deflection of the lever.

From the measured amplitude and phase response (Fig. 5.7b) we can immediately see that the driving force decreases as a function of separation z. Close to the surface the amplitude response of the lever at resonance becomes too small to be measurable. As we will see this is caused by both a decreasing driving force and increasing viscous damping.

Taking into account the dielectric properties of the thermally grown 400 nm suface oxide layer, the measured amplitude and phase curves were fitted using

$$A(\omega) = \frac{1}{2}\frac{\pi\epsilon_0 R}{(\tau/\epsilon_{SiO_x} + z/\epsilon_r)}V_{AC}^2 \cdot \frac{1}{k_c}\frac{1}{\sqrt{\left(1-\frac{\omega^2}{\omega_0^2}\right)^2 + \left(\frac{\omega}{\omega_0 Q}\right)^2}} \tag{5.1}$$

$$\phi(\omega) = \arccos\left(\frac{1-(\frac{\omega}{\omega_0})^2}{\sqrt{(1-(\frac{\omega}{\omega_0})^2)^2 + (\frac{\omega}{\omega_0 Q})^2}}\right) \tag{5.2}$$

Here τ is the thickness of the thermally grown silicon dioxide layer of 400 nm and ϵ_{SiO_x} its dielectric constant of about 3.6. [139] R is the probe radius, k_c the lever stiffness and V_{AC} the applied excitation voltage. The separation z is determined from the displacement of the scanner

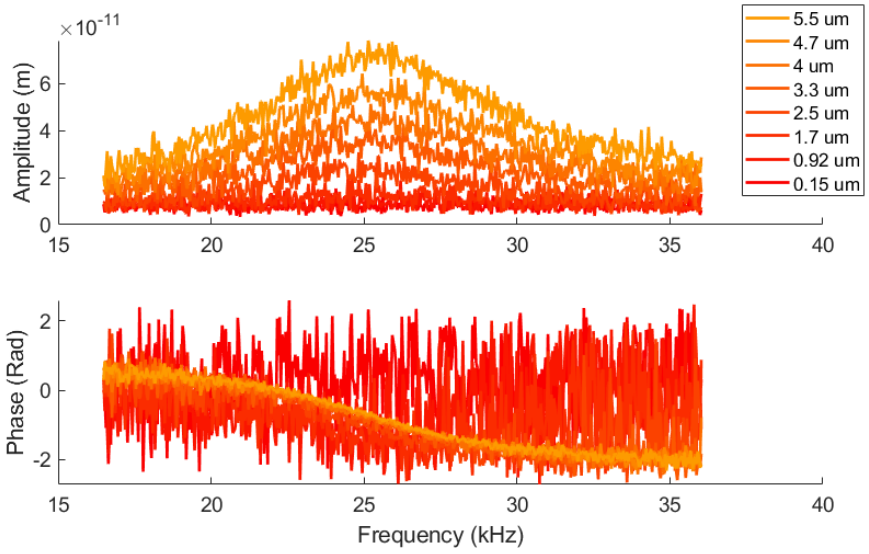

Figure 5.3: Amplitude and phase data measured at varying probe-sample separations in deionized water using capacitive excitation at the second harmonic with $V_{AC} = 0.7V$ and $V_{DC} = 0V$. The excitation strength diminishes for with decreasing probe-sample separation, with the amplitude response completely dissapearing below the noise floor for separations smaller than about 2 µm.

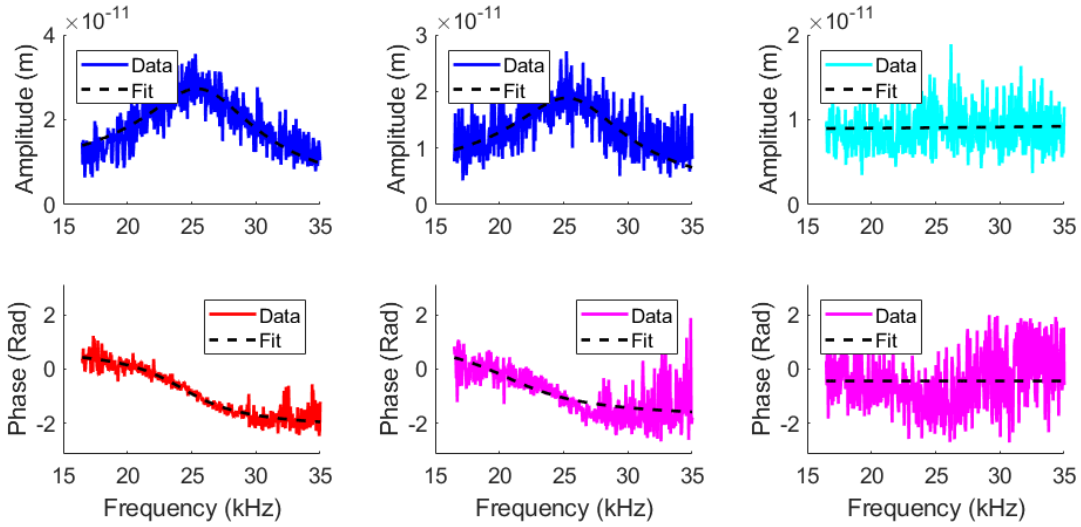

(a) (b) (c)

Figure 5.4: Fitted amplitude and phase data as measured using capacitive excitation in deionized water at a distance of (a) 2.7, (b) 2.3 and (c) 0.9 µm from the surface. At large distances (a) both amplitude and phase can be properly fitted with equations (5.1) and (5.2). Below 2.7 µm of separation (b) the measured phase contains too much noise to be properly fitted and the resulting values for Q and ω_0 are not accurate, while the amplitude is still usable. Below about 1.5 µm of separation both curves do not fit well.

with the zero position being the point of contact as determined from the static deflection of the lever. The relative permittivity ϵ_r, resonance frequency ω_0 and quality factor Q are used as fitting parameters.

Due to the low excitation strength at small separations, the measured amplitude response of the lever becomes too small in comparison to the measuring noise for accurate fits. As a consequence of this the fitted phase equally includes a lot of noise. This effectively defines three regimes: Far from the surface where both amplitude and phase can be fitted (Fig. 5.4a), an intermediate region where the phase contains too much noise for fitting but the amplitude can still be used (Fig. 5.4b), and finally a region close to the surface where the lever response dissapears below the noisefloor (Fig. 5.4c). Note that these three regimes are presented as determined by eye and their precise position is not absolute.

Due to this the fitted parameters (Fig. 5.5) are presented in four colors. The parameters determined from the measured amplitude are presented in blue while those from the measured phase are presented in red. When the quality of the fit becomes too low to guarantee an accurate value the parameters are instead presented in cyan and magenta for amplitude and phase respectively.

The strength of the driving force was found to be much lower than expected from the bulk dielectric properties of water, fitting $\epsilon_r = 1$ at large separations decreasing by an order of magnitude over 5 µm of distance while approaching the surface. This decrease in excitation strength is unexpected, as the screening of the electric field due to free ions in the water is expected to decrease for small probe-sample separations.

The quality factor saturates at the furthest probe-sample separation of 5.5 µm, indicating that there should be no calibration problems due to residual interactions.

As the surface charge V_0 in water is not known, it is not possible to determine the expected electrostatic gradient. The values found for $Z'(z)$ (Fig. 5.6) are close to zero for larger separations, but increase slightly when approaching a separation of 1 µm.

The found values for $Z''(z)$ at larger separations are below what is expected from the bulk viscosity of the liquid, but for small probe-sample separations approaches the values predicted from the Reynold's viscous damping. It is noteworthy that within 1 µm for the surface, where the fitting of the amplitude curve appears to lose meaning, the fitted values still match the predictions from the Reynold's viscous force.

The results demonstrate that capacitive excitation can be used to determine the mechanical impedance of the probe-sample interaction in deionized water using AFM. While there still is some discrepancy between the theoretical modeling and experimental reality, the AFM lever can be sufficiently excited using the capacitive excitation method to determine the variation of its resonant properties.

5.4.1 Stability over time

The dielectric properties of water depend on ionic content which can to change over time as ions from the environment enter the deionized water. Due to this increasing ionic content, it is expected that the driving force will decrease over time as the ions screen more of the electrostatic potential. To investigate this screening and the stability of the measurement over time, the resonant properties of the lever were measured at approximately constant probe sample separation for 50 hours (Fig. 5.7b).

Within the first hours of the experiment the reference phase in the system shifted by $\pi/2$ for unclear reasons (Fig. 5.7a). Most of the shift occured within the first hour and the drift rate decreased notably after 6 hours. Note that such a frequency independent shift does not effect the determination of the quality factor as presented in the previous section.

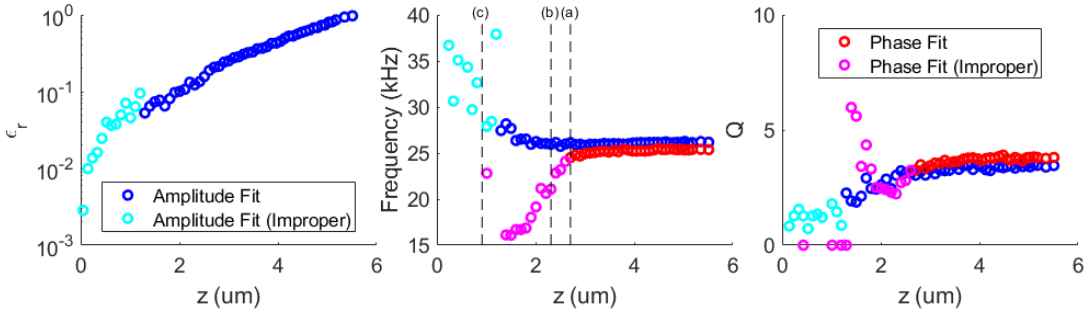

Figure 5.5: Parameters exctracted from the measured amplitude and phase using capacitive excitation in deionized water. Well fitting data is presented in red and blue circles, while poorly fitting data is presented in magenta and cyan circles. The strength of excitation indicates a relative permittivity of 1 at large separations, which steadily decreases to 10^{-1} while approaching the surface. Both the quality factor and resonace frequency saturate for large saturations, indicating no residual interactions at these distances. The positions at which figures 5.4(a-c) are measured are indicated with dashed black lines.

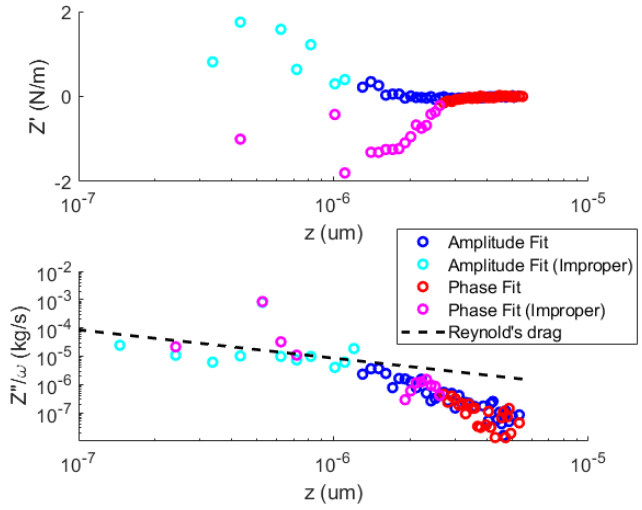

Figure 5.6: Values for $Z'(z)$ and $Z''(z)$ found from ω_0 and Q as determined from the measured amplitude data using capacitive excitation in deioinized water. These curves demonstrate that it is possible to extract the mechanical impedance at resonance from the amplitude and phase curves measured in liquid using capacitive excitation. As V_0 is not known, it is not possible to calculate the expected electrostatical gradient. The value found for $Z''(z)$ is slightly too low at large separations, but approaches the value predicted by the Reynold's force for smaller separations.

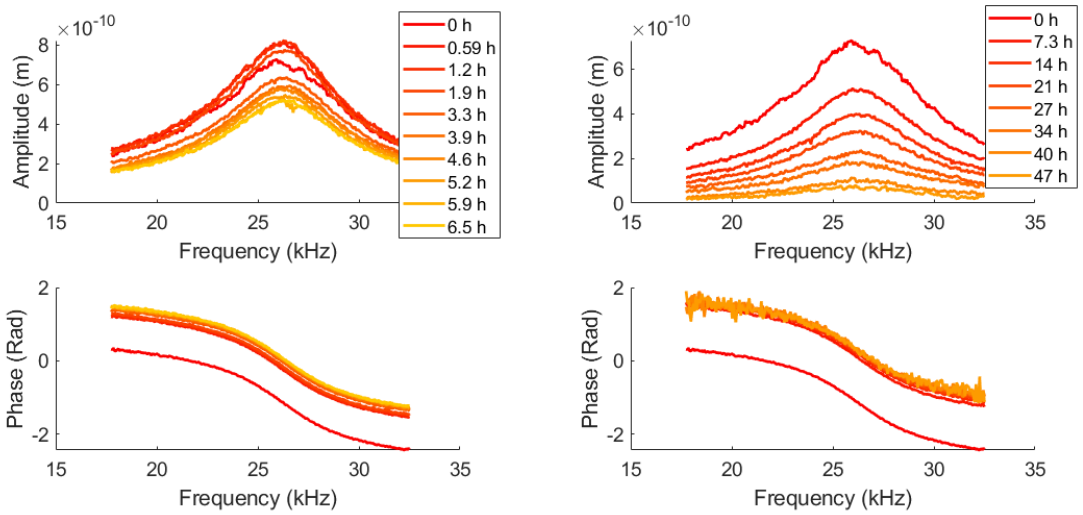

(a) (b)

Figure 5.7: Amplitude and phase measured using capacitive excitation in deionized water with $V_{AC} = 0.7V$ using the second harmonic while at the same scanner position over 50 hours. (a) The phase response shifts by a value of $\pi/2$ in the first 6 hours, but remains stable after this period. (b) The excitation amplitude diminishes slowly over the 50 hour measuring period.

The excitation strength was found to vary over time in three regimes (Fig. 5.7). Within the first 30 minutes the driving force increased slightly, after which this trend reversed and it decreased by a third over a 5 hour period. This was followed by a slower decline over the remaining 50 hours of the measurement, at the end of which the excitation strength had decreased by an order of magnitude.

It is suspected that the decrease in excitation strength is the result of the ionic concentration in the water increasing over time. As more ions enter the water the electrostatic potential is increasingly screened, decreasing the excitation strength.

As the PID controller that maintains constant probe-fiber separation became unstable at the end of the measurement, it was not possible to estimate the distance from the surface at which the measurement was performed by moving into contact. Due to this ϵ_r could not be determined for the measurement and the amplitude response is presented in arbitrary units.

Interpreting these results is made somewhat difficult by the fact that the setup was not designed to maintain a stable position over such long periods of time. As determined in section 2.5.5 the drift in the setup is on the order of 1 nm per minute, which could amount to a drift of 3 µm over 50 hours.

While in principle a drift in position of the probe could change the excitation strength, it is not likely that this explains the currently presented result. As previously demonstrated the probe-sample separation must decrease to reduce the excitation strength. Such a decrease implies an increase in the Reynolds viscous damping and decreasing quality factor, which is not measured. Due to this it is more likely that the decrease in excitation strength is caused by screening of the electric potential by a slowly increasing ionic content.

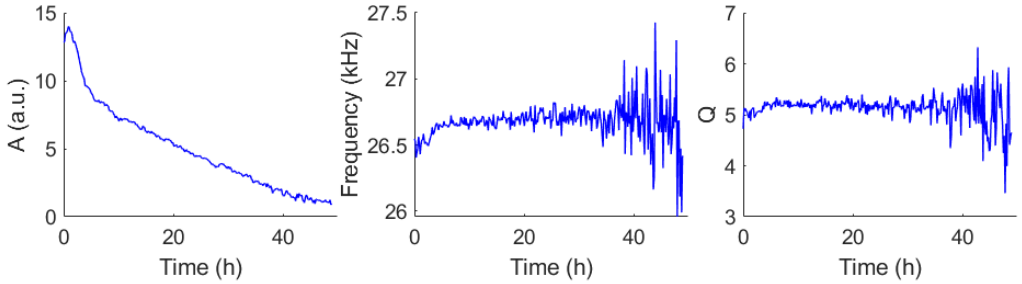

Figure 5.8: Amplitude, resonance frequency and quality factor measured over 50 hours in water using capacitive excitation with $V_{AC} = 0.7V$ using the second harmonic. The amplitude is presented in arbitrary units as the probe-sample separation is unknown. The resonance frequency and quality factor shift slightly in the first 6 hours but remain stable after. The noise in the values increases as the measured amplitude diminishes.

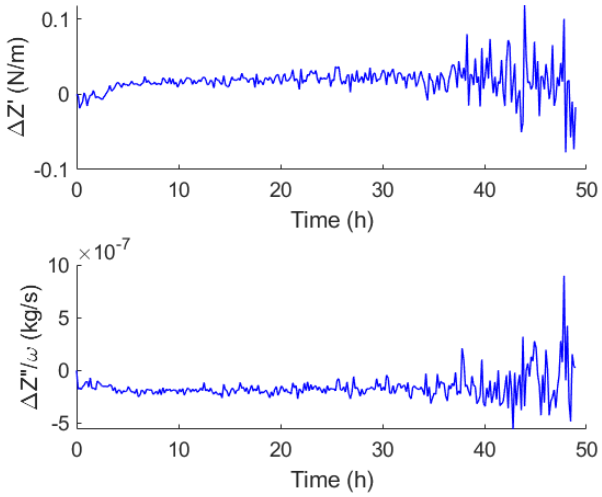

Figure 5.9: Variation in $\mathcal{Z}(z)$ over 50 hours in deionized water using capacitive excitation with $V_{AC} = 0.7V$ using the second harmonic, as determined from the variation in ω_0 and Q using equations (4.4) and (4.5). After a slight shift in the first 6 hours, the measured value remains stable. The noise on the measurement increases over the 50 hour period as the measured amplitude diminishes.

5.5 Conclusions

We have demonstrated that capacitive excitation of an AFM probe in deionized water is possible. When measuring on the first harmonic of the excitation signal, the measurement suffers from stability problems. This is likely due to the V_0 surface potential term which does not follow the usual scaling for a dielectric liquid.

Measuring on the second harmonic of the excitation signal does provide a transfer function with a shape close to the analytical description and a driving force $f_{2\omega} \propto V_{AC}^2$. The effective dielectric constant corresponding to the driving force is much smaller than expected from bulk values, obtaining a value of 1 at a distance of 5 µm and decreasing further for smaller probe-sample separations.

$\mathcal{Z}$ can be determined from the shape of the resonance, but like the measurement in PDMS oil, the sensitivity on the conservative component too low to accurately determine the electrostatic gradient. At the same time the dissipative component underestimates the value expected from theoretical considerations.

Additionally the excitation strength was found to vary over time and decrease slowly on long timescales. This is likely due to the ionic content of the water increasing over time, as ions from the air diffuse into the water.

Based on these results it will be difficult to perform a non-contact measurement of the elastic modulus of soft condensed matter in water using capacitive excitation in its current form. As demonstrated, using the first methodology the sensitivity for $Z'(z)$ is too low and $Z''(z)$ does not provide the expected values.

Improving this sensitivity would require a way to increase the quality factor the lever, which may be difficult due to the use of colloidal probes. Using higher stiffness levers would be another possibility, though the stiffness of 2 N/m used in the currently presented results is already on the high end of what is commercially available.

Application of the second methodology using in PDMS oil, measuring the amplitude and phase response at a specific frequency, requires quantitative description of the driving force. This would require a quantitative model for the electrostatic potential at each separation, including a quantitative description of the sample surface state including the electric double layer structure. These surface forces depend strongly on the ionic content in the water, and would require strict control of this parameter.

Chapter 6

P-NIPAM Polymer Brushes

Contents

6.1 Introduction

Stimulant responsive substrates are surfaces with properties that can change reversibly through control of an external parameter such as pH, temperature, light exposure, etc. One class of such materials is the polymer brush, created by grafting stimulus sensitive polymer chains on a surface. By exposing these grafted chains to a certain stimulus, the conformation of the polymer chains will change, altering the properties of the functionalized surface. Such surfaces have previously found application in the designs of nanofluidic valves and chemical gates. [140, 141]

Poly(N-isopropylacrylamide), or p-NIPAM, is a commonly studied thermosensitive polymer. [142–144] At room temperature it is hydrophilic and solvable in water, where its chains will hydrate and take a swollen conformation. Above its lower critical solvation temperature (LCST) of about 32°C, the hydrogen bonds on the chain are suppressed, the chains become hydrophobic and will phase separate from the surrounding water. This causes the polymer to collapse into a globular form. [145, 146]

By grafting p-NIPAM polymer chains onto a substrate it is possible to create thermoactive surfaces. If this grafting is done at sufficient surface density, the chains are forced into an extended configuration creating a brush like structure. [147] As a brush, the LCST of p-NIPAM does not vary significantly from the bulk value. [148] Below the LCST the swollen chains create a hydrophilic surface, while above the LCST they will phase separate from the liquid creating a hydrophobic surface. As the LCST is close to physiological temperatures, p-NIPAM brushes have attracted interest for bio-medical applications. [149]

To quantify the surface properties of p-NIPAM polymer brush functionalized surfaces, they have been previously investigated using force sensors, including the SFA [150, 151] and AFM. Previous AFM investigations will be shortly summarized in the next section to provide context to the presented results.

For this work we investigate p-NIPAM polymer brush surfaces at room temperature by measuring the interaction force between a sharp probe and the sample as a function of the separation distance, commonly called a 'force-distance' measurement. We report on a long range adhesive interaction between brush and probe in deionized water that extends up to multiple microns. Strains of the polymer attach to the probe upon contact and are pulled away from the surface upon retraction, creating a bridge of polymer strains between probe and surface. While such behavior has been previously found close to the LCST, it is not yet reported below the LCST. Additionally, previously unreported rupture events were found to occur upon retraction, where elastic energy is stored in the polymer strains until the applied force breaks the bonds between the probe and the attached polymer chains.

In addition to the main force-distance measurements the polymer brush surface, it has been investigated using amplitude modulation AFM (AM-AFM). In these techniques the behavior of the AFM lever as an harmonic oscillator is used to investigate the interaction between probe and surface as a function of separation. The polymer brush surface was also imaged in air and in deionized water using AM-AFM. While these measurements did not lead to new insights on the polymer surface, they are included for completeness.

6.1.1 Investigations of p-NIPAM using AFM

p-NIPAM brush surfaces of varying thicknesses (τ) have previously been investigated by comparing force-distance curves above and below the LCST, usually using soft silicon-nitride levers with sharp probes. Below the LCST a reversible repulsive interaction is found upon approaching the surface. [154–156] This repulsive force upon compression is attributed to steric repulsion

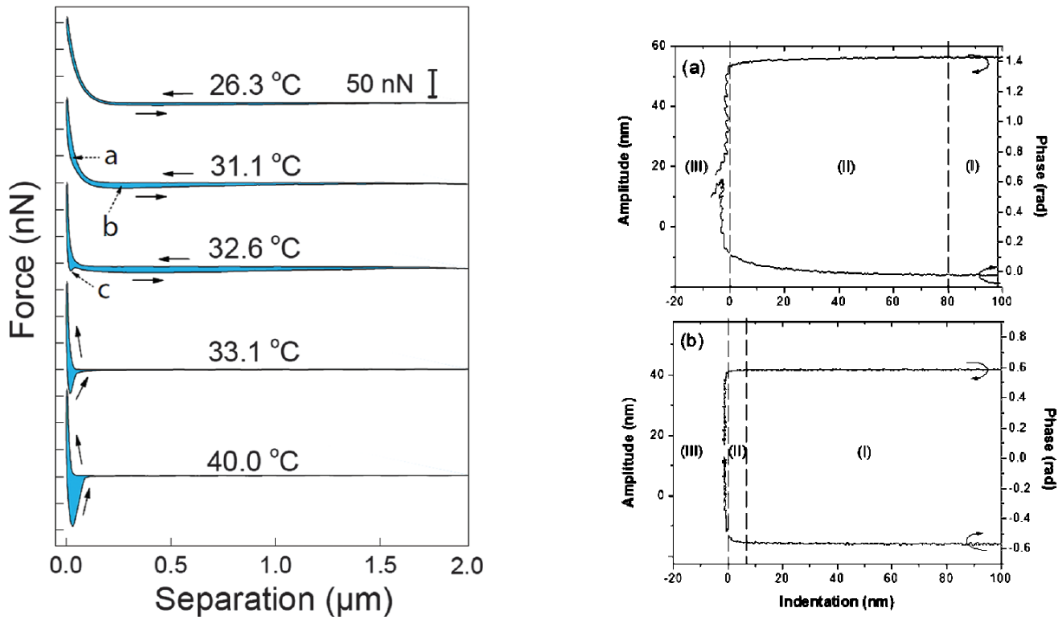

Figure 6.1: (a) Amplitude-phase-distance measurement on a dense p-NIPAM polymer brush. When above the LCST, the length of the weakly interacting region decreases by a factor of 10. Taken from [152]. (b) Force-distance data as a function of temperature. A reversible repulsive interaction is measured below the LCST, while an adhesive interaction is measured below it. Close to the LCST an intermediate state is measured, with tip-sample adhesion persisting beyond a micron of separation. Taken from [153]

between the p-NIPAM polymer strains. [157]

For low-density grafts, an attractive interaction is found upon approach, interpreted as p-NIPAM strains attaching to the probe, pulling probe and surface together through entropic forces. The strength of this force increases with grafting density, but disappears for high density brushes. [147]

For dense brushes above the LCST the interaction remains fully repulsive upon approach, though the apparent stiffness of the brush increases. [158] Upon retraction an adhesive interaction between probe and brush is measured with an adhesive force of some 50 nN, persisting to some 300 nm from the sample. [153, 159].

A single study measured amplitude-phase-distance (APD) curves in liquid, using a free oscillation amplitude of about 60 nm. [152] Below the LCST a region of weak repulsive interaction was found, extending to twice the expected swollen polymer length (Fig. 6.1b). Upon further compression a region of strong repulsive interaction was found. Qualitatively similar behavior was found above the LCST, but the length of the weakly interacting region decreased by a factor 10. Damping of the probe in the weakly interacting region was found to decrease as function of temperature while transitioning over the LCST.

Lastly, force-distance curves were measured using golden colloidal probes while for varying temperatures close to the LCST. [153] These measurements demonstrated a continuously changing swelling ratio between 20 to 40°C. The transition from reversible repulsion to adhesion

was also clearly demonstrated, revealing an intermediate state with strong adhesion between polymer and the gold sphere (Fig. 6.1a). This adhesive interaction extended up to multiple microns from the surface, indicating the existence of a 'polymer bridge' between probe and surface. This result was reproduced using silica colloidal probes. To explain this behavior it is proposed that close to the LCST the p-NIPAM-probe interaction is stronger than the p-NIPAM - p-NIPAM interaction, while above the LCST the p-NIPAM - p-NIPAM interaction dominates.

6.2 Methods

To perform both the force-distance and the dynamic measurements, a BRUKER Dimension Icon (Fig. 6.2a) was used, made available by the CIME Nanomonde. This commercially available optical-beam deflection AFM was equipped with a 'Dimension Direct Drive Tapping' fluid cell. To measure in liquid a meniscus is created between the fluid cell and the sample surface (Fig. 6.2b). The laser reaches the lever through an optical window.

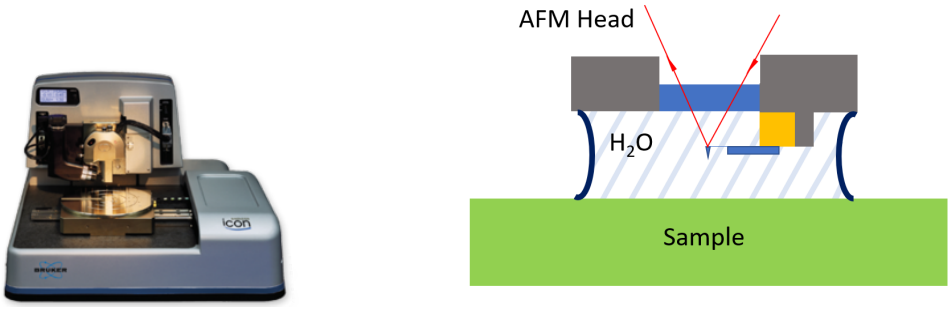

(a) (b)

Figure 6.2: (a) BRUKER Dimension ICON AFM. (b) Overview of the liquid cell. A capillary of deionized water is created between the AFM head and the sample.

BRUKER silicon-nitride MSNL probes were used for most force-distance measurements, which feature pyramidal tips with varying front (15°), rear (25°) and side-angles (22.5°), a nominal tip radius of 2 nm and a stiffness between 0.07 and 0.6 N/m.

For a higher lever stiffness, BRUKER RTESP probes were used. These silicon probes have a nominal stiffness of 5 N/m, slightly sharper side angles for the tip (17°) and a bigger nominal tip radius of 8 nm.

For imaging and APD curves, silicon BudgetSensor Tap300 probes were used, featuring a pyramidal shape with varying angles along the cantilever axis (20-25°), on the side (25-30°), and at the apex (10°) a nominal tip radius below 10 nm, a stiffness of 40 N/m and a resonance frequency in air around 400 kHz.

Before each measurement the sensitivity of the photo detector was calibrated by measuring the lever response in contact with a silicon wafer. The stiffness of the lever was subsequently determined by measuring the thermal motion of the lever in water. [120]

Deflection of the lever d is measured as a function of piezo displacement z, which is related to a force through the stiffness of the lever. To remove contributions from imperfect centering of the photodiode as well as misalignment in the z-piezo, a second order polynomial fit of the first 100 measuring points is subtracted from the deflection data. To determine the true tip-

sample separation D, the deflection of the lever is added to the z-piezo displacement through $D = z - \frac{d}{k}$.

All measurements were performed in a climatized room with a constant temperature of 20 °C. The AFM is situated in an acoustic isolation hood to minimize acoustic noise and maintain a constant temperature.

6.3 Materials

6.3.1 PNIPAM Polymer Brush Samples

The p-NIPAM polymer brushes were created on silicon wafers through surface-initiated Atom Transfer Radical Polymerization (ATRP). ATRP is a 'grafting-from' technique, in which the polymer chains are polymerized directly onto the surface. This is in in contrast to 'grafting-to' techniques, in which the chains are first polymerized in solution and grafted onto the surface.

The surface initiated ATRP protocol used for the results presented in this manuscript is based on a previously published methodology. [151, 160, 161] In rough overview of the three step process, the silicon surface is first hydroxylated, after which 3-Aminopropyl triethoxysilane (APTES) can be grafted onto it. The APTES then acts as an ATRP initiation site from which the p-NIPAM polymeriation is performed (Fig. 6.3). For the sake of briefness, only the high level steps are indicated. A more detailed description including the quantities of the chemicals used can be found elsewhere. [162]

Polymerization protocol

The [100] orientation silicon wafers are rinsed in ethanol and water before being placed in a plasma cleaner where they are exposed to a 0.4 mBar water vapour plasma for 6 minutes. This yields a clean and highly hydroxylated wafer surface.

The hydroxylated wafer is then submerged in an APTES solution for 1 minute. The NH_2 groups of the APTES are then derivatized by immersing the surface in a solution of 2-bromo-2-methylpropionyl bromide (BMPB) and tri-ethylamine (TEA) in dichloromethane (DCM) for 1 minute. This creates a surface of exposed C–Br bonds which are the initiator sites for the ATRP reaction.

While not used in the current work, it is possible to obtain lower surface density brushes by immersing the APTES covered wafers in a solution of propionyl bromide (PB) and TEA in DCM. The PB passivates a fraction of the amine-groups by terminating them with a PB molecule, which is not active in the ATRP step that follows.

Finally the p-NIPAM brushes were polymerized using the 'activators regenerated by electron transfer' (ARGET) ATRP technique. The wafers are submerged in a solution of NIPAM in ultrapure water mixed with small quantities of $CuBr_2$ and the complexing ligand PMDETA. The polymerization is then allowed to proceed for a certain amount of time, usually between 2 minutes and two hours. The longer the polymerization is allowed to take place, the longer the p-NIPAM strains become and the thicker the polymer brush will be.

To remove any weakly physisorbed polymer chains from the brush surfaces, the samples were left to soak for 24 hours in deionized water at room temperature, after which they were dried with nitrogen.

Samples created through the protocol described above, without the PB termination step, feature a high grafting density of $\sigma \approx 0.5$ chains/nm^2 which guarantees a brush-like structure. [162]. Three p-NIPAM polymer brsuh sample were created with varying ATRP polymerization

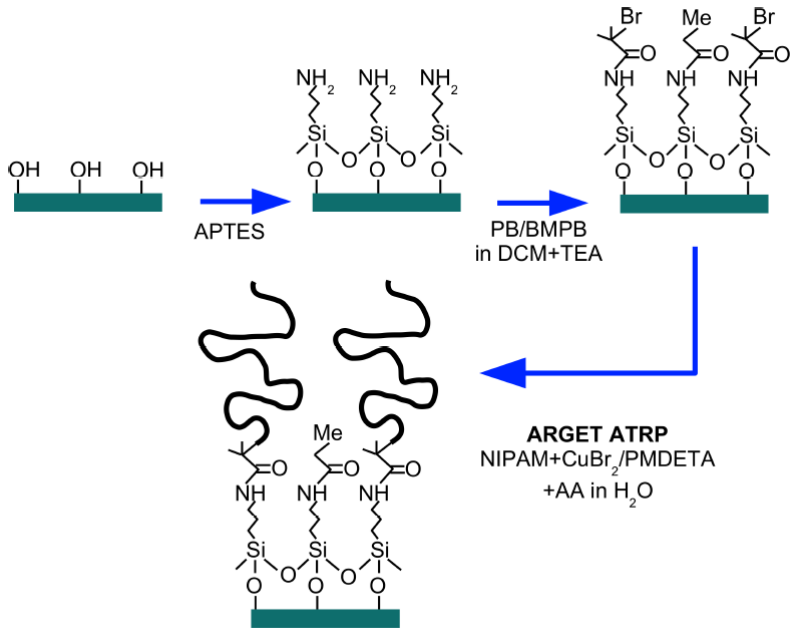

Figure 6.3: Overview of the three step ATRP process. The hydroxylated wafer is covered in APTES, which is derivatized in a solution of BMPB and TEA in DCM, creating C−Br bonds, from which the ATRP creates the grafted p-NIPAM strains. Though not used in the current work, surface density can be controlled by passivating a fraction of the initiator sites with a PB molecule, which is inactive to ATRP.

times. Through ellipsometry these samples were found to have a dry thicknesses of 73, 120 and 150 nm.

For the measurements in liquid a meniscus of Milli-Q deionized water was created between the sample surface and the AFM head.

6.4 Results

6.4.1 Force-distance data

A distinct interaction profile (Fig. 6.4) was found when measuring force-distance curves in deionized water below the LCST with soft ($k_c \approx 0.035$ N/m) SiN levers. On approach a fully repulsive force is found, starting at some 500 nm from the surface, in agreement with previous samples of similar thickness (Fig. 6.1a, curve). In contrast to previous publications, an adhesive force is measured upon retraction with a maximum on the order of 500 pN, and persisting up to multiple microns of tip-sample separation.

The overall profile is one of an attractive force that, after achieving the maximal adhesive force, decreases slowly as a function of tip-sample separation. This is possibly explained by multiple van der Waals bonds forming between probe and the polymer chains when the probe penetrates the brush. As the probe is retracted from the brush, the polymer chains are pulled out of the brush surface, creating a polymer bridge between the sample surface and the probe.

As the separation distance increases, chains will detach from the probe, lowering the adhesive force.

Previously unreported rupture events with a nominal strength of 100-200 pN are visible throughout the retraction. In these events elastic energy is stored in one or more polymer chains, which is released when the elastic energy exceeds the strength of the bond between the chain(s) and probe. The final rupture event in figure 6.4 has a rupture force of 400 pN while storing energy over a distance of 700 nm, indicating an effective stiffness for the polymer chain on the order of $k_{pol} \approx 5 \cdot 10^{-4}$ N/m, significantly lower than $k_c \approx 3.5 \cdot 10^{-2}$ N/m for the lever. The variance in rupture strength is attributed to a varying number of binding sites between probe and chain. A particularly well connected chain might reach 400 pN, while most ruptures remain below 200 pN. This would indicate that with sufficient time resolution it could be demonstrated that the rupture event are composed of a multitude of smaller rupture events, one for each bond breaking. The time resolution of the currently presented data was however insufficient to make such claims.

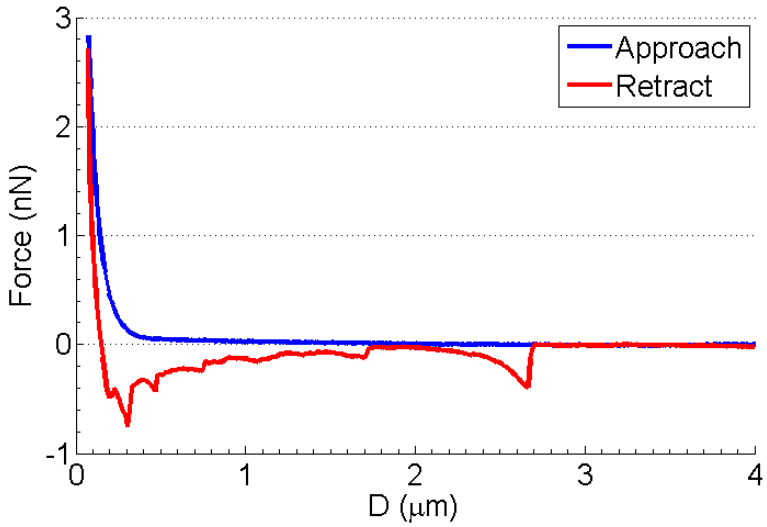

Figure 6.4: A representative force curve as measured on a 120 nm p-NIPAM polymer brush surface. On approach a repulsive force associated with compression of the brush is measured. On retraction an adhesive interaction persisting up to the contour length of the polymer chains is found. Rupture events are visible at multiple locations with strengths up to 500 pN.

To investigate the effect of brush thickness on this interaction, force-distance curves were measured on samples of 73, 120 and 150 nm thickness in an environment of deionized water using sharp SiN $k_c \approx 0.035$N/m levers (Fig. 6.5, a, c, e). For each sample, at least 10 curves were measured on a single location and the distance between point of separation from the surface and full detachment was determined (Table 6.1). The crossing of the zero upon retraction was taken as the point of separation.

A positive correlation between sample thickness and detachment length was found, with the detachment length being of the order of the contour length of the polymers. This is in agreement with the adhesive interaction being the result of the polymer chains connecting with the probe.

As previously reported experiments used levers of both silica and silicon nitride, the mea-

τ (nm)	l_D (µm)	σ (µm)
75	1.59	0.104
120	1.76	0.076
150	2.36	0.203

Table 6.1: Average detachment length (l_D) and its standard deviation for each p-NIPAM brush sample in deionized water. Averages were taken over at least 10 repeated force curves on a single location.

surements were repeated with silicon probes. Due to the material properties of silicon, silicon probes tend to be stiffer than those made of SiN. The stiffness of the probes used for the currently presented data, at $k_c \approx 8$ N/m, was a factor 300 higher than that of the SiN probes ($k_c \approx 0.035$ N/m. Due to this stiffness difference, the force sensitivity is much lower as the lever deflects less for a given force. Due to this smaller deflection, the Z-distance over which a certain force is reached when pulling on a polymer chain is also reduced by a factor of 300.

Regardless of these considerations, rupture events were still visible (Fig. 6.5 b, d, f). Due to the lower force sensitivity, the measurements are more susceptible to drift and noise, which makes it difficult to evaluate the longer ranged decaying adhesive force.

To investigate possible viscoelastic behaviour of the p-NIPAM polymer brush, force-distance measurements were performed at varying approach speeds between 0.25 and 16.4 µm/s. Curves were taken on a single location to avoid effects of sample heterogeneity (Fig. 6.6). Averages were taken over >10 curves to minimize rupture events. It is remarkable that for this set of data, despite the averaging, a single rupture event close to contact remained reproducible for all the cruves. No difference in the tip-sample interaction was found except increased drag from the lever in the liquid, apparent from a constant positive/negative deflection on approach/retract.

6.4.2 Amplitude and phase data

The amplitude and phase of the oscillation were measured on the 120 and 150 nm thick polymer brushes (Fig. 6.7). Measurements were done both in air and deionized water, with the measurements in water preformed at room temperature below the LCST.

In air, with the brush in a collapsed state, the oscillation amplitude of the probe decreases from full to 0 over a distance of 42.75 nm. At 40 nm from the surface, a small negative phase shift is visible, indicating an attraction dominated interaction between tip and sample. Closer to the surface it becomes positive, indicating a repulsion dominated interaction, consistent with the time-averaged deflection profile. Further reversal of the phase shift while in contact with the sample bears no physical significance, as the amplitude in this region is close to zero.

In deionized water, where the brush is in its extended state, the decrease in the amplitude signal starts at some 190 nm from the surface for the 120 nm thick sample and 300 nm from the surface for the 150 nm thick sample. From the phase response of the probe we can determine that the interaction is always in a repulsion dominated regime (positive phase shift). In contrast to air, there is no adhesion dominated region, which is consistent with the measured deflection profile.

Note also that the APD-curves in liquid, measured with stiff ($k_c \approx 40$N/m) levers, are fully reversible and exhibit no polymer bridging. There is a factor 2 difference in time averaged force between the two samples, but these values should be interpreted with some care as it is difficult to accurately calibrate the stiffness of such stiff levers in liquid. Due to the high stiffness of the levers the amplitude of the Brownian motion in the first mode is very small.

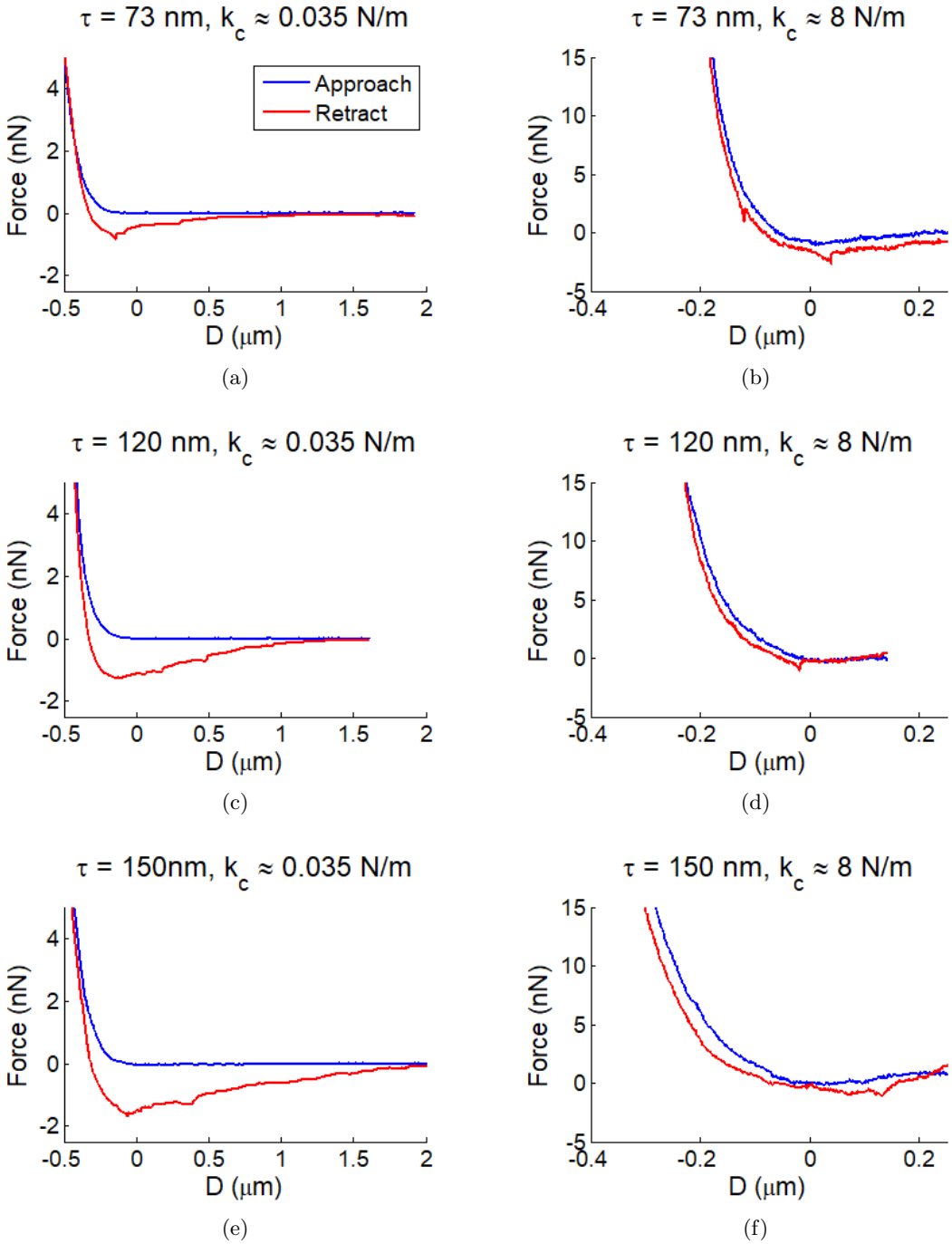

Figure 6.5: Deflection curves as measured on p-NIPAM polymer brush samples in deionized water. Thickness of the sample (τ) and stiffness of the lever (k_c) are noted in each graph. Note that the D axis is not the same for both stiffnesses and the point of contact is taken as 0.

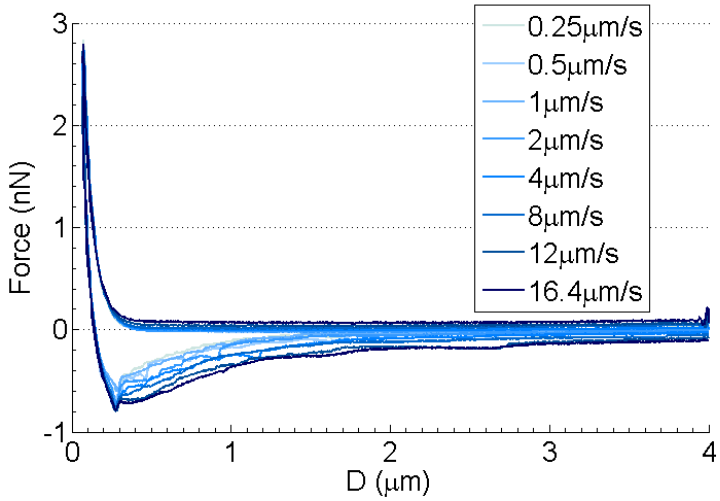

Figure 6.6: Force-distance curves as measured on 150 nm p-NIPAM brush for varying approach velocities. Averages were taken over >10 curves to minimize rupture events. No correlation between approach velocity and adhesive strength is visible. For higher approach velocities the hydrodynamic drag of the lever becomes visible.

6.4.3 AM-AFM imaging

To investigate the homogeneity of the sample surface in air and liquid below the LCST, it was imaged using amplitude modulation AFM (AM-AFM). (Fig. 6.8). In air the brush surface has a RMS roughness of 1.689 nm over 1 x 1 µm and features holes with a depth of at least 10 nm.

Imaging the surface in deionized water was found to be difficult. While no holes were visible, streaking occurred over the sample (Fig. 6.9a). This behavior is reminiscent of the instability that can occur in the lever motion when there are two branches of z-positions that comply with a given amplitude setpoint. [163] Significantly increasing or decreasing the setpoint did however not prevent the streaking. Additionally the amplitude-phase-distance curves showed no discontinuities in the amplitude channel, which is normally indicative of this instability occurring.

It was attempted to use AFM image processing software (Gwyddion) to remove the streaking which was somewhat effective (Fig. 6.9b). The RMS roughness of the resulting surface was found to be 1.480 nm over a 1 x 1 µm area which is comparable to previously found values. [164] Despite the presence of streaking, this value is slightly lower than the value found in air, likely due to the absence of holes in the surface.

6.5 Discussion

We propose that the polymer bridging behavior originates from multiple polymer strains attaching to the tip upon contact, and detaching from the tip upon retraction; a 'polymer bridge' connecting the tip and substrate. While retractingthe lever, the polymer chains pull the lever towards the surface. Detachment of individual chains creating rupture events. As rupture events are visible at different distances from the surface, it is clear multiple polymer strains are attached to the probe.

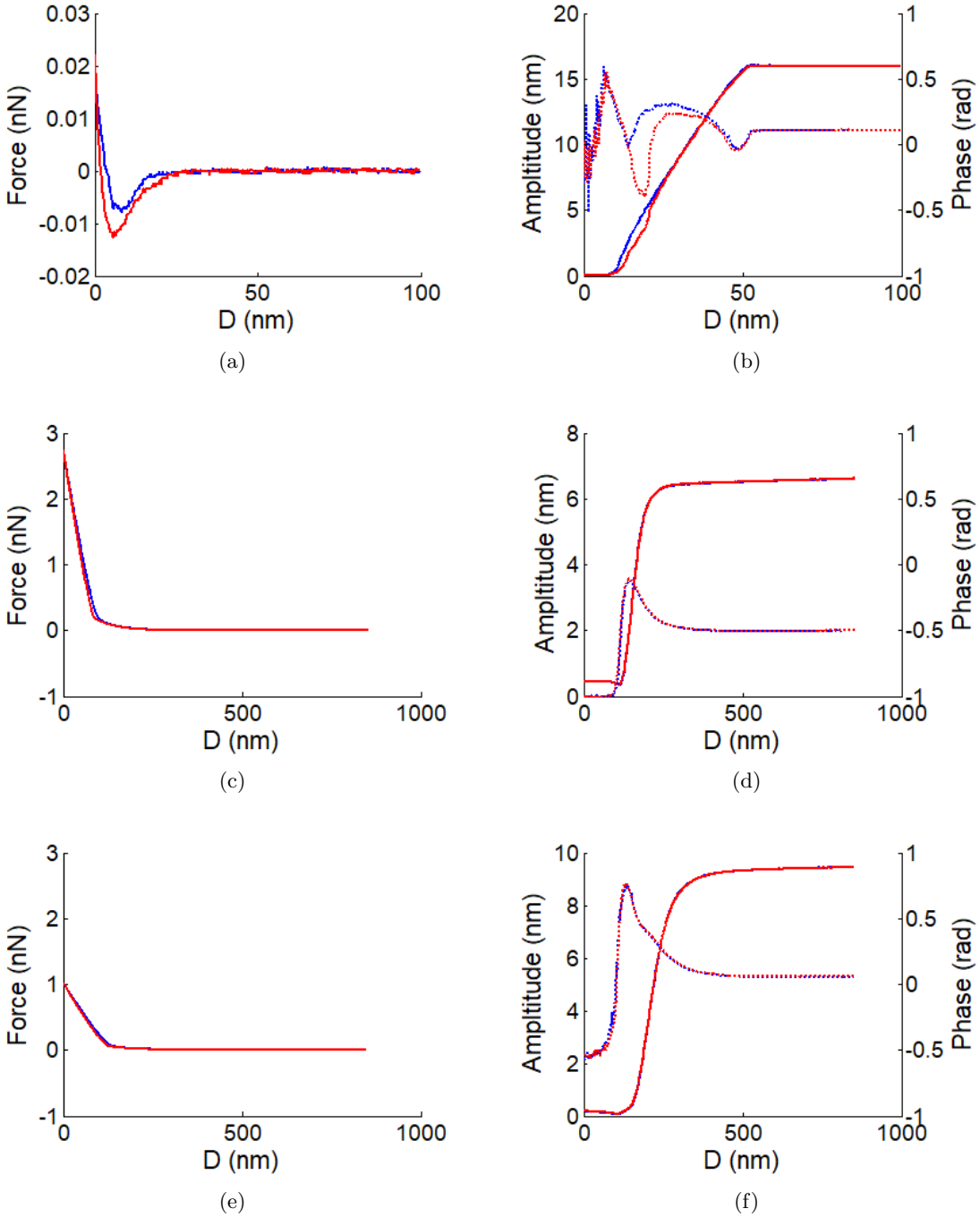

Figure 6.7: Time averaged deflection, amplitude and phase curves for 150 nm thick p-NIPAM polymer brush in Air (a, b), 120 nm thick p-NIPAM polymer brush in deionized water (c, d) and 150 nm thick p-NIPAM polymer brush in deionized water. (e, f)

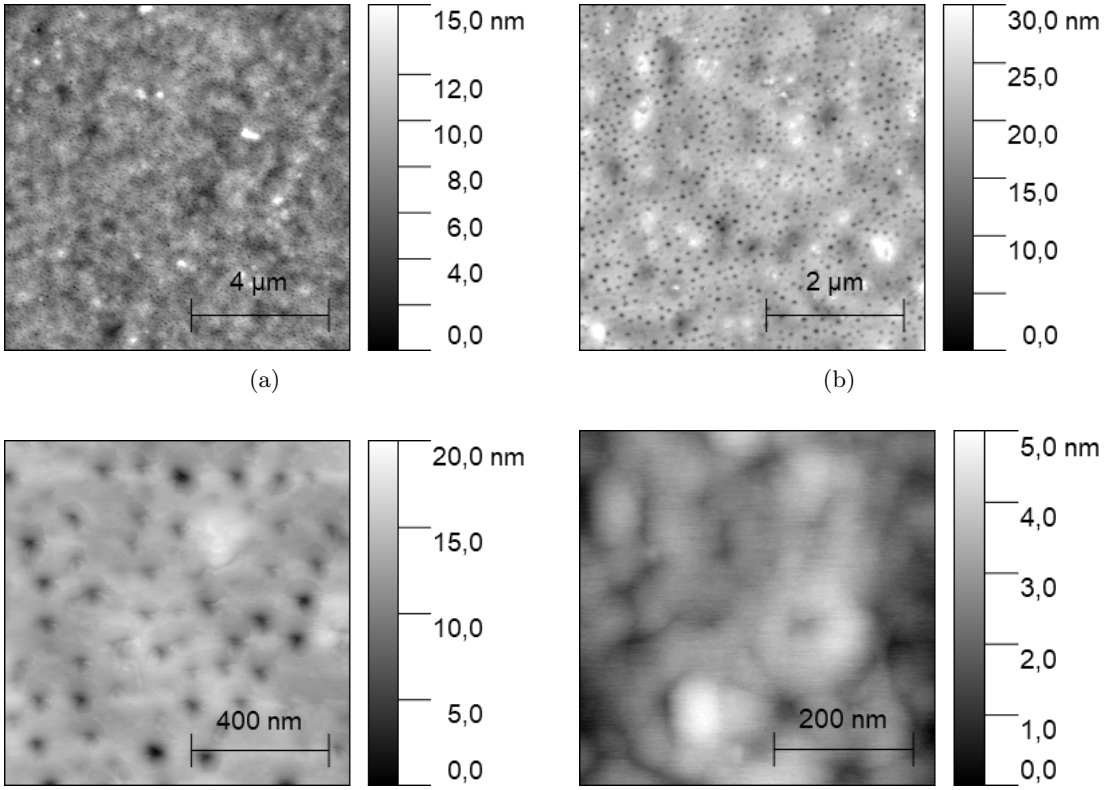

Figure 6.8: Surface of a 150 nm polymer brush as measured with AM-AFM in air.

The overall behavior of the tip-sample interaction upon retraction shows a decaying profile. Normally this behavior is associated with the probe experiencing sliding friction upon retraction out of the material. In our case however, this behavior is visible up to microns outside of the brush material, meaning it cannot be simple sliding friction between the probe and the brushes. It could be the polymer chains slowly slide of the probe, or it is friction between between the attached polymer chains and the rest of the brush that creates this decaying adhesive force.

6.5.1 Polymer bridging below the LCST

Interestingly, this behavior has been previously reported on p-NIPAM polymer brushes by Yu et.al., but only close to the LCST. [153] In our case the measurements were performed at room temperature, well below the LCST.

We hypothesize that the answer may be found in the LCST itself. While the LCST was found to be similar for bulk and brush polymers, it is unclear how it depends on parameters such as pressure. It is possible the penetration of the probe into the polymer brush creates a local buildup of water pressure in the brush, as the water does not have sufficient time to drain. This increased pressure could possibly temporarily lower the LCST below room temperature, facilitating the connection of the p-NIPAM strains to the probe. While this would explain how the strains and probe can connect below the LCST, it does not explain why the strains remain connected upon withdrawal of the probe from the brush.

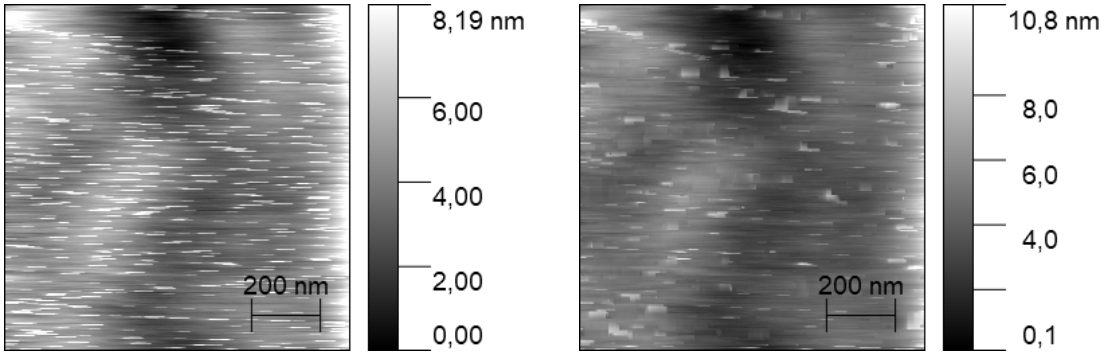

(a) (b)

Figure 6.9: **a)** Surface of 120 nm p-NIPAM brush in deionized water. Streaking is visible throughout the surface, making it difficult to determine the RMS roughness of the sample. **b)** Streaking removed through Gwyddion. 1.480 nm RMS over 1x1 um.

However, it must be noted that while the experimental room in which the measurements were performed was at room temperature, we have not directly measured the temperature of the liquid. While the light source of the AFM was turned off before experiments to prevent heating of the sample, it cannot be excluded that the sample is not heated to the LCST due to residual heating of the AFM system. It should be noted that previously reported results required a heating stage to attain temperatures at or above the LCST. [153]

6.6 Conclusions

In summary, we have found previously unreported polymer bridging below the LCST for sharp probes on p-NIPAM polymer brushes grafted by surface-initiated ATRP on silicon, which despite similar previously published experiments as of the current date has not been reported. In addition we report rupture events up to 400 nN occurring at multiple positions during retraction.

An import requirement to solidify the result is performing the experiment in a temperature controlled environment. This would also allow for further investigation of the properties of the polymer bridge as a function of temperature.

The controlled formation of the polymer bridge in addition to the dynamic measuring techniques proposed in chapter 3 would allow a novel way to investigate the inter-polymer mechanics, such as the sliding friction between polymer strains. By measuring the mechanical impedance of the polymer bridge for varying frequencies, more could be learned about the visco-elastic properties of this system.

Chapter 7

Quick clay

Contents

7.1 Introduction

Soil is the top layer of the earth, which consists of a mixture of organic matter, mineral and liquids. Due to the large variance in soil composition found around the world, many different types of soil can be classified. When considering the solid soil components this classification is generally done by mineral particles size. In this frame, 'clay' is defined as any mineral particle with an effective diameter below 2 µm, though some equally small minerals, such as gypsum, quartz and carbonates, are generally excluded from this category as they have special chemical properties.

Research into the mechanical properties and the microstructure of clays has a long history. The first proposed models for its structure and inter particle bonds date back to 1925. [165,166] It is an important soil type that is widely found in nature and has found use in many industrial applications as a ceramic ingredient, adhesive, filler, anti-friction agent, coating for paper, and more. [167,168]

A subtype of clays, called 'sensitive' or 'quick' clays, is prone to undergo a solid to liquid phase transition when disturbed. Deposits of this material in the northern hemisphere have previously been responsible for landslides, leading to large scale damage and loss of life. The precise microstructural mechanism for this transition is still poorly understood.

Although nearly a century has passed since the first models for the microstructure of clay were proposed, experimental determination of the precise structure is still an open area of research. [169–171] Recently, a publication by Deirieh et.al. questions the experimental procedures used in historical publications in the field, that were fundamental to developing the currently accepted textbook models for the microstructure of clay. [172]

The key difficulty in determining the microstructure of clay is performing measurements in its natural water saturated state. The conventional microscopic techniques that achieve the required resolution, such as scanning electron microscopy, are not liquid compatible. The historical solution to this problem was performing low-temperature microscopy on plunge frozen clay samples. This rapid freezing procedure ideally leads to vitrification of the water in the clay material, allowing investigation using Cryo-SEM without altering the clay microstructure.

In this chapter we present exploratory measurements into the mechanical properties and microstructue of sensitive clays using AFM, a technique that as of yet has not been widely adopted in the field. AFM is liquid compatible, and it allows exploration of the clay microstructure in its natural water saturated state. Additionally, AFM can be used to perform micro- and nanoindentation measurements, which gives acces to the local mechanical response of the clay material. We believe AFM can make important contributions to key questions in the field of clay geology.

First, a short overview of previous work on the (sensitive) clay microstructure will be provided. Secondly, the results of our exploratory measurements on the material will be presented. Lastly, we will discuss the capabilities of AFM measuring techniques to contribute to open questions in the field.

7.2 The microstructure of clay

Most of the sub 2 µm diameter particles found in soils are clay particles, generally consisting of silica and gibbsite sheets (Fig. 7.1a). These sheets have large aspect ratios, with a width and length on the order of microns, but a thickness of only a couple of nanometers. In many cases the behavior of aggregate particles is determined by solid-solid friction. In the case of clay however, due to the combination of small particle sizes and large aspect ratios, the mechanical response is determined by particle-particle interactions instead.

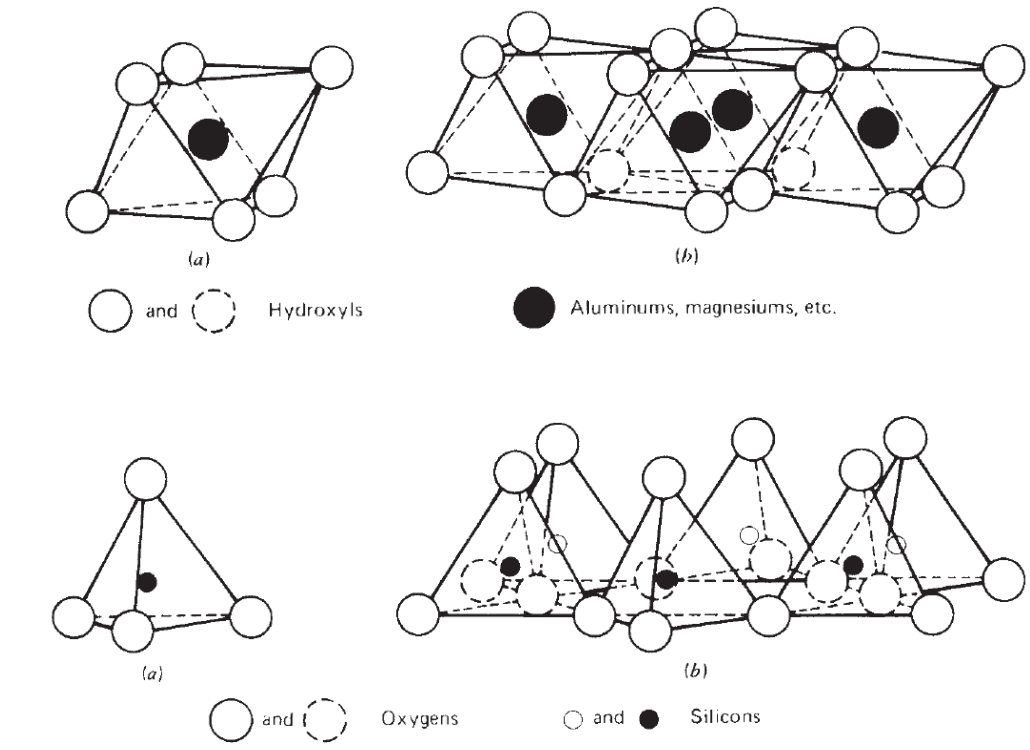

(a)

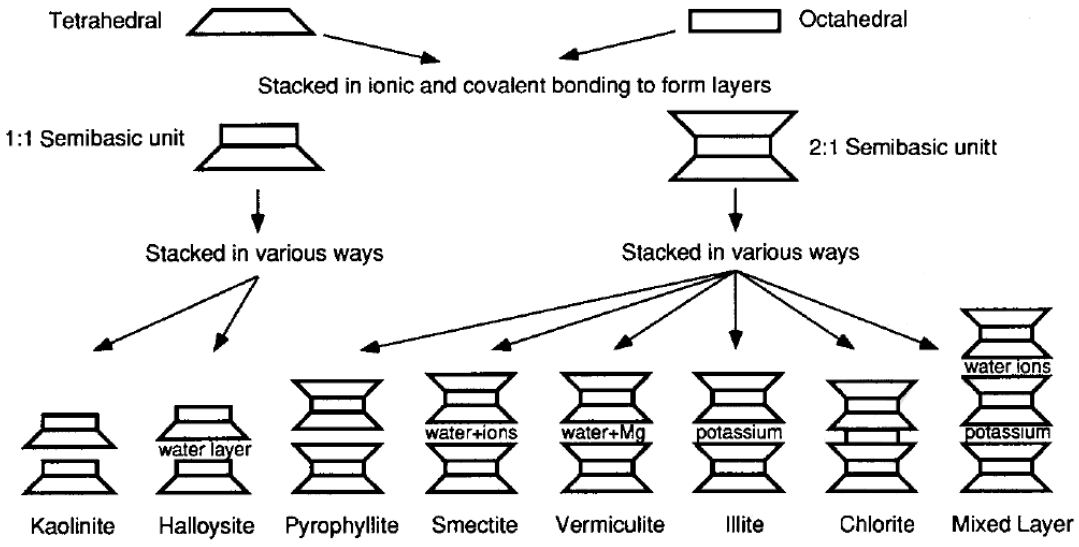

(b)

Figure 7.1: (a) Unit cell and structure of gibbsite and silica sheets. (b) Stacking of octahedral gibbsite and tetrahedal silica semibasic units into various clay minerals. Taken from [173].

These interparticle interactions lead to face-face stacking of clay particles. Stacked silica and gibbsite sheets create semibasic units, in which a gibsite sheet is covered with a silica sheet on one or both sides. The sheets are strongly bonded through primary valence type bonding. [173] These semibasic units can subsequently form many different clay minerals, differentiated by the type of interaction connecting them. The configurations most commonly found in clay are those of kaolinite, illite and montmorrilonite (Fig. 7.1b), in which the connections are mediated by hydroxyls, potassium ions and hydrogen bonds respectively.

Natural clays can have a large volume fraction of water contained in pores in the structure. While this volume fraction can be difficult to measure directly, the fraction by weight can be up to 50%. Considering the silica particles are 2 to 3 times as dense as water, this leads to an estimation of a volume fraction of 50 to 75 % water. Due to this large water fraction, the particle-particle interactions are not only sensitive to structure and composition of the mineral, but also to the pore water chemistry of the surrounding water. The ionic content plays an important role in the type and strength of the inter-particles bonds, as free ions can screen electrostatic contributions from the surface charges present on the clay particles.

The varying minerals have different specific surface areas and surface charge distributions, which is generally anisotropic, varying between the face and edge sides of the mineral. Additionally, atoms in the sheet lattice can be displaced by Al^{+3} and Mg^{+2} ion, creating an internal charge deficiency which likewise contributes to electrostatic inter-particle interactions. Due to this, clay minerals can also be categorized by their cation exchange capacity (CEC), a measure of how many cations can bind to the surface. Minerals with a large CEC are generally more sensitive to pore water chemistry.

While the composition of clays is generally well understood, its structure is still an open field of discussion. Historically, there have been three competing models: A cardhouse structure consisting mostly of edge-edge and face-edge connections between mineral particles, [174–177] a honeycomb structure of face-face contacts supporting water pores [165,178,179], and a stabilized gel structure due to electrostatic repulsion between particles. [180, 181]

As optical microscopy techniques have insufficient resolution to resolve the microscopic scale of the microstructure, an alternative was found in cryo-electron microscopy. SEM techniques are usually performed in vacuum and thus incompatible with water, while the clay microstructure collapses when the water is removed from the material. A solution was found in plunge freezing the water saturated clay samples to solidify the microstructure. The rapid freezing of the clay material causes the water to vitrify and the clay microstructure to remain intact. Investigations using this technique reported the existence of a closed-cell honeycomb structure dominated by face-edge and face-face contacts between the clay particles, which became the textbook model for the description of the clay microstructure. [182–188]

A recent publication by Deirieh et.al. has reopened this discussion. [172] They state that the sample sizes used in previous investigations were too large for efficient plunge freezing and the cooling process will not fast enough to fully vitrify the water. As such they indicate that the reported honeycomb structure is not the natural clay microstructure, but a result of the water expanding during crystallization. They compare cryo-electron microscopy images on plunge frozen and high pressure frozen (HPF) clay samples, the latter being a more recent technique that is suitable for vitrifying sample of sizes up to 200 µm. They report that while the plunge frozen clay material did feature the honeycomb structure, the HPF samples featured clay particles and their aggregates in a randomly oriented structure. The textbook honeycomb model for the natural microstructure of clay may thus be incorrect.

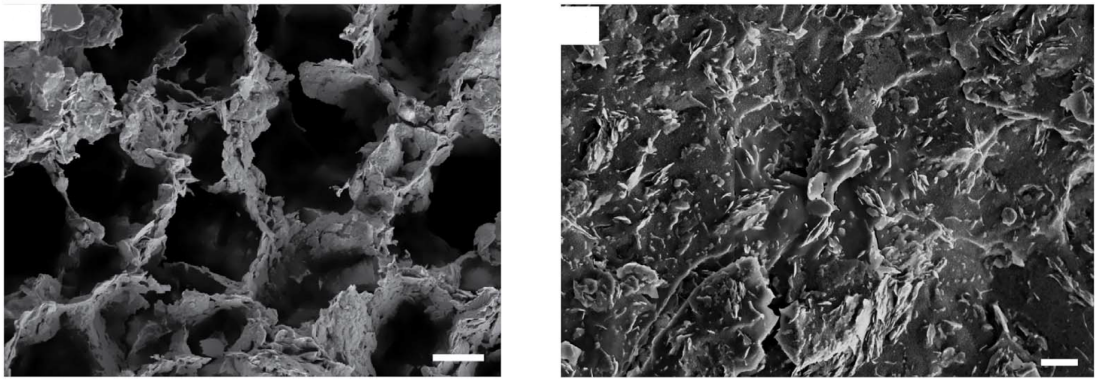

(a) (b)

Figure 7.2: (a) Cryo-SEM image taken on plunge frozen clay. Scalebar 2 µm. (b) Cryo-SEM image taken on HPF frozen clay. Scalebar 1 µm. Taken from [172].

7.2.1 Quick clay

Sensitive clay, or 'quick clay', is a substype of clay that can undergo an irreversible solid-to-liquid phase transition when sufficiently disturbed. Large natural deposits of this subtype are found in the northern hemisphere, specifically in Canada, Scandinavia and parts of Russia. When unintentionally disturbed, the sudden liquefaction of large masses of sensitive clay can create landslides, which threaten local life and infrastructure. As such it is important to understand the precise nature of this behavior. Currently, the microstructural origin of this phenomena is poorly understood.

In its undisturbed state quick clay can carry some load. Macroscopic tests on natural samples extracted in Sweden were found to have an undisturbed strength in the 30-100 kPa range. [189] When the load surpasses a threshold, the material partly or fully liquefies and loses most of its strength (Fig. 7.3a).

On the macroscale, sensitive clays are characterized by their sensitivity, the ratio between the undisturbed S_{up} and disturbed S_{ur} strength $S_t = \frac{S_{up}}{S_{ur}}$. [165] Note that clays become quick clays not because their undisturbed strength is high, but because their disturbed strength is low. The transition from undisturbed to disturbed is irreversible and the disturbed material cannot be reconstituted. Some sensitivity can be regained artificially through flocculated sedimentation and subsequent leaching in a geotechnical centrifuge. [191]

It was previously determined that sensitive clays have a large open structure, consisting of aggregated stacks of clay minerals and large water filled pores, allowing for a total water content well above the liquid limit (Fig. 7.3b). [173, 192]

The currently most accepted hypothesis for the formation of sensitive clays was proposed in 1966 by Pusch. [190] It poses that clay deposits originally formed in a highly saline environment. This caused flocculation of the clay particles as a porous, open structure. The clay was subsequently leached by melting glacial water, weakening the inter particle bonds due to the changing pore water chemistry, and leaving a highly porous microstructure sensible to collapse. The leaching of potassium (K^+) from the illite in the clay can convert the mineral into a vermiculite or montmorillonite structure, which are both very weakly bonded. The leaching of ions from the structure reduces the screening of the electric double layer as well, making inter-particle interactions more repulsive, which weakens the structure.

Up until recently it was not possible to reliably reconstitute sensitive clays and natural clay

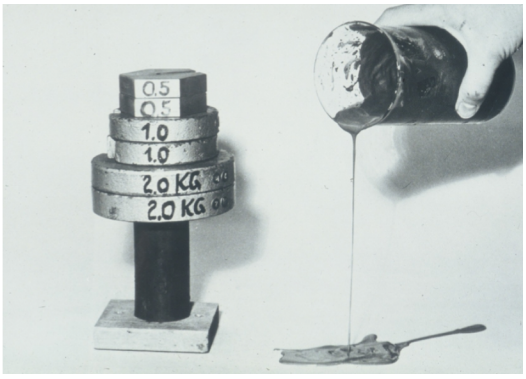

(a)

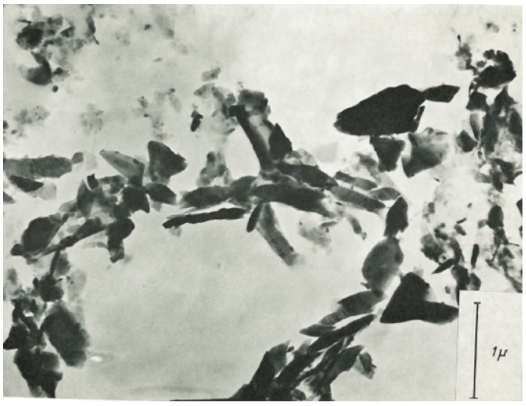

(b)

Figure 7.3: (a) Undisturbed quick clay can carry some load, but if this load surpasses a threshold the material liquefies. Courtesy of Chalmers University of Technology, Sweden. (b) Early SEM images of a slice of quick clay. The material contains a network of large pores that in its natural state are filled with water. [190]

.

samples had to be extracted to perform experiments. The precise composition of these natural samples is not well controlled, as most natural soils have no clean clay fraction and are mixed with larger silt particles that have a size of 2 to 63 µm. This severely limits the possibility for precise quantification of how different mechanisms in the clay microstructure contribute to the emergence of sensitivity in clay materials.

7.2.2 Clay and AFM

From the previous considerations, it is clear that there is a need for an experimental technique that can resolve the microstructure of water saturated clay without the need of extensive sample preparation. We believe the AFM platform can contribute here. Surface characterization of soft materials in liquid by AFM is a well developed field of research, specifically in the context of cell-biology [193–195]. Additionally, AFM force-indentation measurements can be used to extract the mechanical response to compression at interaction lengths from nanometers to microns. As the clay particles are structured at a micrometric lengthscale, indentation using probes with nanometric sharpness allows investigation of the material at the level of individual clay particles, while using micrometric probes sufficiently larger than individual particles allows investigation of the structure as a whole.

Force-distance measurements have been previously performed to investigate illite-illite particle adhesion, demonstrating that high salt concentration can screen attractive inter particle interactions [196]. More recently, strong Hofmeister effects were found between montmorillonite particles and a mica surface, where the repulsive interaction strength depends on the cation species present in the solvent in a specific series. [197] No direct investigation of the water saturated clay surface using AFM has been published up till now. The work presented here is an exploration of the contributions AFM can bring to the investigation of the clay microstructure.

7.3 Methods

The clay samples were investigated both in dry and water saturated state using multiple AFM measuring methods. Topographic images of the dry clay surface were made using amplitude modulation AFM (AM-AFM) to visualize its micro structure. Attempts to use AM-AFM on the water saturated clay failed, likely because the material cannot sustain the pressures that are applied to the surface during scanning. Force Volume Mapping, in which the applied pressure can be controlled at the pixel level, was found to be an effective alternative to visualize the microstructure.

As a first step to explore the complex mechanical behavior of the clay, nano- and microindentation measurements were performed on both dry and water saturated samples with conical and colloidal indenters. While the probe is in contact with the surface, the measured sample indentation as a function of applied normal force can be interpreted through the frame of contact mechanics. As a first rudimentary method for quantifying the clay material properties, we relate the measured pressure as a function of indentation to estimates of the bond density and energy within the clay microstructure.

7.3.1 Nanoscope Wizard 4

AFM measurements were performed using a JPK NanoWizard 4 (Fig. 7.4a), a commercially available optical beam deflection AFM. To perform AFM measurements in water, the cantilever is mounted on a glass block that is lowered into the liquid (Fig. 7.4b). The laser reaches the lever through the glass block and due to the small glass-lever distance, any changes in the optical path due to the optical properties of the liquid are minimized.

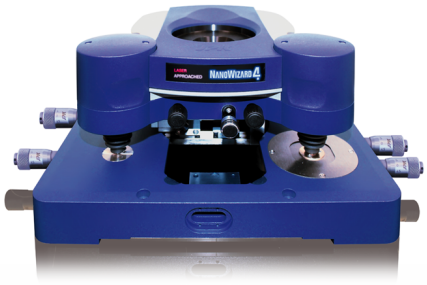

(a)

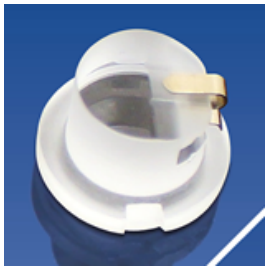

(b)

Figure 7.4: (a) JPK NanoWizard 4 (b) Cantilever holder for measurements in liquid.

Calibration of the AFM

Precise calibration of the AFM system is important when quantifying the mechanical properties of a material with force-indentation measurements. Any error in the calibration of the lever stiffness or the photodiode-sensitivity will lead to improper scaling of the force axis. Both values are also used to determine the deflection of the lever, which is added to the z piezo-displacement to determine real probe-sample separation. Precise calibration of the lever stiffness is not always straightforward, with best-practices having errors of up to 5 %.

For measurements in air the photodiode sensitivity was calibrated by measuring the deflection of the lever in contact with a rigid object. When confined between the AFM head and a

rigid surface, the deflection of the lever and corresponding change in photodiode voltage are equal to the movement of lever base piezo. Assuming the extension of the piezo is well calibrated, the sensitivity of the photodiode can be determined. The stiffness of the lever can then be determined by measuring the brownian motion of the lever in air, as previously described in section 2.6.

Calibrating the lever stiffness in water is a more complicated affair due to practical limitations. As the difference in optical properties of water and air change the angle of deflection at the glass interface, the position of the laser on the lever will change when moving from one environment to the other. This alters photodiode sensitivity and dry calibration values cannot be used in liquid. While in principle the previously described calibration protocol could be repeated in liquid, calibration of the photodiode sensitivity through contact on a rigid surface is practically unfeasible. The height difference between the clay sample and the silicon wafer substrate is too large. As such an alternative calibration method was used.

The stiffness of the lever was first determined in air. After submerging the cantilever in liquid and realigning the laser, the Brownian motion of the lever in liquid is measured. The photodiode sensitivity is then set, such that the stiffness of the lever in liquid matches the value previously determined in air. This method is not optimal, as the effective stiffness of the lever depends on the position of the laser which will inevitably not be exactly the same in liquid as in air. Although this does not affect the main conclusions of this chapter, it should be kept in mind when evaluating the numerical data presented.

7.3.2 Probes

As it of interest to investigate the material response above and under lengthscale of the clay microstructure, both conical and colloidal probes were used for force-distance measurements. While the conical probes are sensitive to the clay particles at the nanoscale, the colloidal probes measure a laterally averaged response over multiple microns of material. Conical probes were also used to image the microstructure of the clay, as colloidal probes lack the required lateral resolution.

Conical probes

For the force-distance measurements and force-volume mapping using conical probes, NT-MDT CSG10 'Golden Series' silicon probes were used. These probes feature a conical tip with a nominal tip radius of 6 nm. The levers had a stiffness between 0.5 and 0.05 N/m, with a resonance frequency around 30 kHz.

For AM-AFM imaging, stiffer NT-MDT NSG01 probes were used. These feature the same tips as the CSG10 probes (conical tip, $R \approx 6$ nm), but with a lever stiffness around 4 N/m and a resonance frequency of 125 kHz.

Colloidal probes

The colloidal probes were created using the protocol described in chapter 2, though no metallic coating was applied as a conducting surface is not required. Spherical silica beads with a radius of 30 µm where glued to the end of the MikroMasch CSC37 base levers. The final probes had a stiffness of about 1 N/m, with a resonance frequency of about 6 kHz in air. The precise radius of each colloidal probe was determined before each measurement using a calibrated optical microscope.

7.3.3 Imaging

Two imaging techniques were used to investigate the clay material. The dry clay in air, with a material stiffness on the order of MPa, amplitude modulation AFM (AM-AFM) [60, 198] proved to be an effective technique to determine the clay surface topography.

With this technique the AFM lever is used as an harmonic oscillator by excited it with an sinusoidal signal through a piezoelectric element. The properties of this harmonic oscillator are then measured as a function of probe-sample separation. The amplitude response of the oscillator will continuously decrease for smaller probe-sample separations due to an increasing probe-sample interaction, which can be used as a gauge of the separation. Through the use of a PID controller, the system can be locked on a certain amplitude setpoint and associated probe-sample separation. By subsequently moving the probe over the sample material, a topographic map of the surface can be traced. This a relatively fast AFM imaging technique, as for each pixel only the amplitude signal and piezo position have to be measured, which can be done in a couple of milliseconds.

AM-AFM was attempted on the submerged clay samples as well, but no stable amplitude setpoint for the PID controller could be found. We expect this is due to the fragility of the material in water. An alternative was found in Force Volume Mapping (FVM), in which a full force-distance measurement is performed at each pixel of the image up to a predefined force setpoint. This allows for the collection of all information associated with a force-distance measurement, including sample indentation as a function of normal load. The collecting of such a large number of force-distance measurements is however a time consuming process, with scanning times for a 256x256 pixel image being on the order of multiple hours.

7.3.4 Compacting of the microstructure

As indicated in the introduction of this manuscript, force indentation data gathered using AFM is normally interpreted through a contact mechanical model that at minimum approximately describes the mechanical behavior of the investigated material. Due to the fragility of the clay microstructure, no such model exists for the currently presented data. To nevertheless relate the measured force-indentation data to the properties of the material, we propose to interpret the pressure with which the material opposes indentation as the bond energy density required to break down the microstructure.

We model the clay microstructure as a network of platelets, held together by inter-platelet bonds. At each platelet-platelet interface, many such bonds are distributed over the surface area on which the two platelets are connected. As will be clear from the force curves measured with conical and spherical indenters, each time the probe enters the material we destroy part of the microstructure by breaking many such bonds between the silicon platelets. This results in compacting of the microstructure into a much denser structure of tightly packed platelets. To interpret the gathered data we propose that the work performed by the probe equals the energy required to break all the bonds within the volume of broken microstructure. Here we ignore the work required to expel water from the microstructure, though we expect these contributions to be small due to the open structure of the clay.

While we do not know the precise energy ϵ_b associated with each bond, we make some order of magnitude estimates. The bonds must be stronger than k_bT or else the material would thermally break down, putting a lower limit on the bond energy of about 0.025 eV. Likewise, the bonds are certainly weaker than covalent bonding, setting an upper limit of about 1 eV and giving us a bond energy ballpark of $0.025\text{eV}<\epsilon_b<1$ eV. The same estimate can be made for the density of bonds ρ_b, as they are certainly less dense than the atomic lattice at $1/\text{nm}^3$ and denser than the platelet-platelet structure $1/\mu\text{m}^3$, giving us limits of $1/\text{nm}^3<\rho_b<1/\mu\text{m}^3$.

If breaking each bond requires an energy ϵ_b [J] and the average density of bonds in the material is ρ_b [m^{-3}], the energy fE_V [J] required to break all the bonds in a volume element dV is determined by

$$\frac{dE}{dV} = \epsilon_b \rho_b \tag{7.1}$$

The instantaneous energy required to break these bonds is directly related to the amount of new microstructure that is broken

$$\frac{dE}{dt} = \epsilon_b \rho_b \frac{dV}{dt} \tag{7.2}$$

The instantaneous work W[J] performed by the probe can be directly measured, and equals

$$\frac{dW}{dt} = F \cdot \frac{dx}{dt} = F \cdot \nu \tag{7.3}$$

Where ν [m/s] is the speed of indentation. Assuming all this work is utilized in breaking the bonds in the material, we can equate $\frac{dW}{dt} = \frac{dE}{dt}$ and find

$$F\nu = \epsilon_b \rho_b \frac{dV}{dt} \tag{7.4}$$

Assuming perfect contact between probe and surface, we can relate the volume of material to be broken down at each instant of time to the surface area of interaction between the probe and the material $S(\delta)$ [m^2], which depends on the indentation depth δ and the geometry of the probe.

$$\frac{dV}{dt} \approx S(\delta)\frac{d\delta}{dt} = S(\delta)\nu \tag{7.5}$$

Combining these equations we find

$$F\nu \approx \epsilon_b \rho_b S(\delta)\nu \tag{7.6}$$

which allows interpretation of $\epsilon_b \rho_b$ as a pressure $P(\delta)$ [N/m^2] through

$$\frac{F(\delta)}{S(\delta)} = P(\delta) \approx \epsilon_b \rho_b \tag{7.7}$$

Thus by measuring the pressure exerted by the material on the probe during indentation, we can estimate the bond energy density within the material.

In an AFM indentation experiment, $F(\delta)$ is directly measured. Through the geometry of our probe and assuming the material surface to be an infinite half plane, we can determine the surface of interaction $S(\delta)$ for the cone-plane and sphere-plane geometries used

$$S_{cp}(\delta) = \pi \tan(\alpha)\, \delta^2 \tag{7.8}$$

$$S_{sp}(\delta) = 2\pi R \delta \tag{7.9}$$

Note that this determination of $S(\delta)$ ignores surface roughness, which for clay can be on the order of multiple µm peak-to-peak. Due to this it is expected that the surface area will be overestimated for small indentations, leading to an overestimation of the pressure.

Added volume contributions

In the description provided above, the material of the broken microstructure is essentially assumed to disappear, which does not correspond to reality. As the microstructure collapses it creates a much denser layer of clay platelets that surrounds the indenting probe. As the stiffness of the platelets is much closer to that of the probe than that of the surrounding microstructure, we propose to include this layer as an effective increase of the probe size. This increase in size of the probe increases the interaction area to a bigger $S'(\delta)$ and the total indentation to a larger value δ'. In effect we assume that the probe and this additional dense layer retain the geometrical shape of the probe.

To determine the size of this denser layer of platelets surrounding the probe, we propose that its volume V_{layer} equates to the volume of material displaced by the probe V_{probe}. In this denser layer, all the water is expelled and only the platelets remain, thus we multiply by the volume fraction α of platelets in the material, which is on the order of 0.25-0.33.

$$V_{layer} = V_{ind} \cdot \alpha \tag{7.10}$$

By adding the volume fraction of the displaced material we increase the displaced volume by

$$V_{tot} = V_{layer} + V_{ind} = (1 + \alpha) \cdot V_{ind} \tag{7.11}$$

For the used cone-plane and sphere-plane geometries, again assuming the material surface to be an infinite half plane, the amount of material displaced at an indentation δ equates to

$$V_{cp}(\delta) = \frac{\pi}{3} \tan(\alpha)^2 \cdot \delta^3 \tag{7.12}$$

$$V_{sp}(\delta) = \frac{\pi\delta^2}{3} (3R - \delta) \tag{7.13}$$

In the case of the cone, we assume conical angle to remain unchanged and can directly find a new indentation depth which we can use to express $S'(\delta)$

$$V_{cp,tot} = \frac{\pi}{3} \tan(\alpha)^2 \cdot \delta'^3 = (1 + \alpha) \cdot \frac{\pi}{3} \tan(\alpha)^2 \cdot \delta^3 \tag{7.14}$$

$$\delta' = \sqrt[3]{1 + \alpha} \cdot \delta \tag{7.15}$$

$$S'(\delta) = \pi \tan(\alpha) \delta'^2 = \pi \tan(\alpha) \sqrt[3]{1 + \alpha} \cdot \delta^2 \tag{7.16}$$

For the spherical geometry the situation is more complicated, as both the indentation depth and the radius of the probe will change due to the addition of layer. As for the conical case we state

$$V_{sp,tot} = \frac{\pi\delta'^2}{3} (3R' - \delta') = (1 + \alpha) \cdot \frac{\pi\delta^2}{3} (3R - \delta) \tag{7.17}$$

Both R' and δ' have to be expressed as a function of δ. From geometrical arguments we can state $R' - R = \delta' - \delta$. After replacing R' in the equation above and some permutations, we find

$$\frac{2}{3}\pi\delta'^3 + \pi\delta'^2(R - \delta) = (1 + \alpha) \cdot \left(\pi\delta^2 R - \frac{\pi}{3}\delta^3\right) \tag{7.18}$$

which has to be solved numerically (Fig. 7.5). With $\delta'(\delta)$ known, R' is calculated through $R' - R = \delta' - \delta$.

For both geometries the addition of this dense layer increases the surface of interaction and thus decreases the measured pressure. In the experiment we measure $F(\delta)$ and compute $P(\delta) = F(\delta)/S'(\delta)$ for each probed indentation. It should be noted that due to the small volume fraction of platelets in the clay microstructure, even for large indentations the contribution from this effect to the total surface of interaction is small.

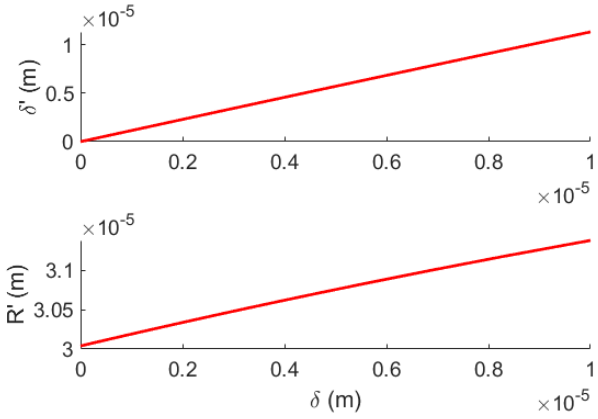

Figure 7.5: Numerical solution to equation (7.18) for $R = 30.04$ µm, the size of the probe used during indentation with colloidal probe. Values are presented for indentations up to 10 µm.

Fitting procedure

Due to the inhomegeneous nature of the clay samples, force-distance measurements often produce data that is difficult to interpret. This is especially true for data from conical probes, which are sensitive to local variation within the clay microstructure. Some care has to be taken while applying the model to ensure the resulting values retain physical sense.

Some force-distance measurements included events where larger parts of sample material was displaced. Should such events be included in the fit, the pressure exerted by the the material will be underestimated due to the resulting drop in force versus indentation. All such curves were excluded from further considerations, which creates a bias towards the more stable segments of the material.

A second experimental difficulty is the large variation in the measured data. For the water saturated clay samples this was faced by collecting a large amount of force-distance curves. A grid of 32x32 measurements was collected, equating to a data set of 1024 force-distance curves for each investigated probe type and approach speed. Instead of comparing the properties of individual curves, the dispersion of a property within the dataset was used as a basis of comparison.

In AFM measurements it can be difficult to precisely determine the point of contact between probe and surface. This is partly because the probe-sample separation cannot be measured independently of the lever deflection and partly due to phenomena such as the 'jump-to-contact'. This makes it difficult to determine which data points in each curve should be included when quantifying the interaction with the surface. Manual determination of this point is unfeasible due to the large amount of force-curves required to obtain statistically significant data.

The point of contact was thus determined by finding the first point that exceeds a small force value above the baseline, usually on the order of 0.5 nN. As the point of contact determined this way will be slightly behind the real point of contact, this leads to an underestimation of the interaction surface area and subsequent overestimation of the pressure at small indentations. At larger indentations the contribution from this error decreases and more accurate values are found.

7.4 Materials

The clay samples were a naturally sensitive clay, extracted using a 50 mm diameter Swedish STII piston sampler, from a depth of 6 to 9 meters at the test site of Utby in the region of Gothenburg, Sweden. [199] The main clay mineral for clay from this site is illite, but it also contains chlorite, quartz, feldspar and calcite. [200] Previous investigations of material from this site found sensitivities of 25 to 35. [201].

7.4.1 Clay sample preparation

Disks of clay were created by cleaving a rod of extracted soil material using an steel wire. No further preparation was performed. The clay samples meant for dry measurements were left to dry naturally over multiple hours. The samples destined for measurements in a water saturated state were stored in a layer of deionized water. Leaching with deionized water has been found to leach ions from the clay material, which will severely weaken the clay structure. [189]

Some measurements were attempted on disks that had been cleaved the day before the measurement and left to dry for a day before submerging them in water. AFM measurements proved to be difficult on these samples as an oily residue released from the sample and deposited on the AFM optical window. Disks cleaved on the day of the measurement did not have this problem. It is unclear whether the residue was a result of the drying and rehydrating of the sample, or a property of these specific clay disks.

7.5 Results on dry clay in air

7.5.1 AM-AFM

The dry clay surface was imaged using AM-AFM (Fig. 7.6), both before (Fig. 7.6a) and after (Fig. 7.6b) force-distance measurements were performed. The dry sample material featured a RMS roughness of 822.5 nm over a 50 by 50 µm area. The total difference between maximal and minimal height of the investigated area was 6.2 µm, close to the limit of what the AFM can resolve.

The dry clay surface showed clear deterioration after force-distance measurements were performed. Holes with a radius of multiple microns were visible at the locations of measurement (Fig. 7.6b, red circles). Horizontal streaks are visible in the post-force-measurement image as well, indicating deterioration of the tip geometry. As the sample material is expected to be softer than the probe, it is unlikely that the tip was damaged and is probably caused contamination of the tip with sample material.

7.5.2 Force-distance measurements

To investigate the heterogeneity and stiffness of the clay material, force distance measurements were performed on the clay samples on multiple sites using conical and colloidal probes. The different probes allow us to investigate the material response both above and below the lateral length-scale of the microstructure. The varied behavior of the force-distance measurements will first be quantitatively described, after which the extracted pressure profiles will be presented.

Conical tips

Force-distance measurements were performed on 17 sites on the dry clay material. Care was taken to maintain a minimal distance of 1 micron between each site to exclude the possibility

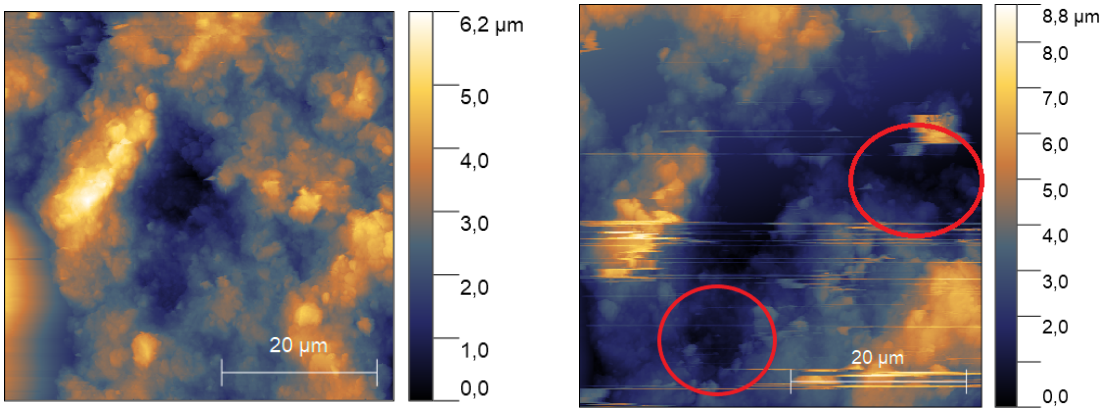

(a) (b)

Figure 7.6: AM-AFM height map taken on clay samples in air before (a) and after (b) force-distance measurements. Before force-distance measurements, the sample had an 822.5 nm RMS roughness over 50x50 microns. The site for the force-distance measurements is indicated in red. The trough at this location has deepened as the material deteriorates under the force-distance measurements.

of interfering measurements. Ten repeated curves were measured at each location.

The measurements revealed complex behavior of the clay material under compression (Fig.7.7). Some curves showed clean hard contact between the probe and sample (Fig. 7.7a), reminiscent of force-distance measurements performed on silicon wafers. Upon retraction the probe adheres onto the sample until the pulling force exceeds the bond strength and snap-off occurs. A slight shift in the distance axis is visible between approach and retract curves while in contact, which is caused by relaxation in the z-piezo in open-loop operation and does not represent the response of the material.

Many force curves did not show clean contact behavior, but revealed erratic behavior as the probe indents the material. A roughly linear response may be measured at first, but after applying sufficient force, the sample material is displaced and the measured force saturates or drops (Fig. 7.7b). This is usually followed by a return to a roughly linear response as the probe comes into contact with more stable material.

In some curves a more gradual response is measured upon first compression of the material, which slowly rises into a stronger resistance to indentation (Fig. 7.7c). This is associated with the displacement of weaker parts of the microstructure until a a more resistant region is reached.

Repeated measurements on the same location clearly demonstrates the compacting of the material (Fig. 7.7d). With each repeated curve, the point of first contact moves deeper into the material as it is compacted by the probe. This effect is largest for the first few curves, after which the compacting behavior diminishes. It becomes increasingly harder for already compacted material to be further compacted.

Pressure profiles

The pressure as a function of indentation was determined using the model described in section 7.3.4 (Fig. 7.8). Due to underestimation of the interaction surface area the found pressure diverges for small indentations, but reaches the MPa scale at maximum indentation.

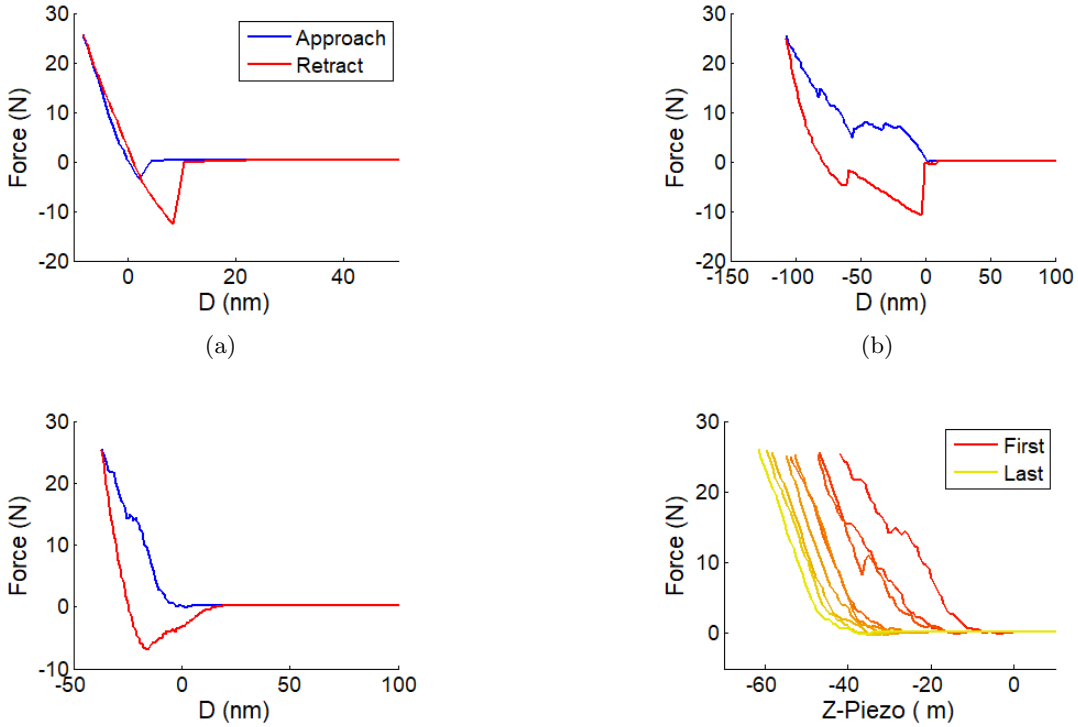

Figure 7.7: Force-distance measurements on dry clay samples in air using conical probes. (a) 'Clean' force-distance measurement. The difference between approach and retract curves in contact is due to open-loop operation of the z-piezo. (b, c) 'Messy' force-distance measurements. If the probe applies a sufficient force the sample material is displaced, indicated by decreased or even negative slope in the force. (d) Repeated measurements on the same location, displaying a compacting of the sample material. Subsequent curves show less material displacement, and the point of contact moves further into the material.

Note that not all data reaches a stable value at the maximum indentation and some caution should be taken with interpreting the obtained value. Likewise 10 repeated curves were taken at the same location, thus the values obtained do not represent undisturbed material.

Each curve was attributed an average pressure value by taking the mean of the 10% of data at the highest indentation (Fig. 7.9). The found values were distributed between 10 kPa and 1 GPa with a log-normal fitted mean of 501 MPa.

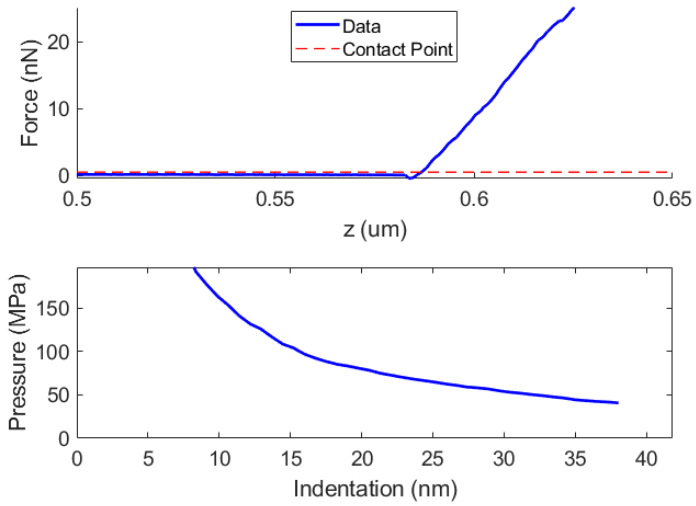

Figure 7.8: Force curve and corresponding pressure profile as measured using a conical indenter on a dry quick clay sample in air. The contact point is determined through a 0.5 nN setpoint. At small indentations the pressure profile diverges due to underestimation of the interaction surface area, but reaches a constant value at higher indentations.

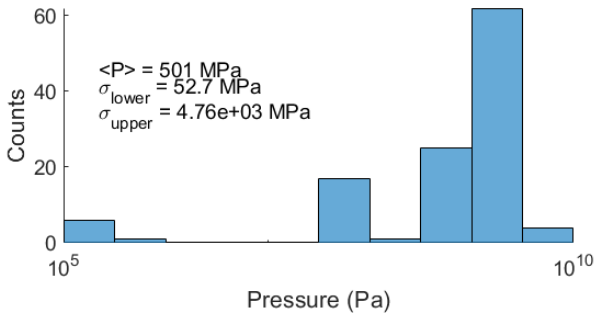

Figure 7.9: Distribution of the average pressure reached at 10% of maximum indentation using conical indenters on dry quick clay samples in air. The distribution is fitted with a log-normal distribution with a mean of 100 MPa and lower and upper standard deviations of 11.1MPa and 1 GPa respectively.

Colloidal probes

Additional indentation measurements were performed on the dry clay samples using colloidal probes with a radius around 30 µm. These were performed at 15 different locations, repeating 10 measurements each time for a total of 150 curves. The radius of the interaction surface for a colloidal probe can be estimated as $a = \sqrt{2R\delta}$, with R the radius of the probe and δ the indentation depth, both in meters. For a 30 µm probe indenting 100 nm, this gives a length a of approximately 2.5 µm. Care was taken to retain a minimal distance between measuring sites of 3µm.

The resulting force-distance curves demonstrate more consistent behavior compared to those measured for conical probes (Fig. 7.10). A long range attractive interaction was found both while approaching and retracting from the sample (Fig. 7.10a). The attraction roughly increased in strength with a D^{-1} scaling, which is equal to that of an electrostatic coupling for a sphere-plane condensator. As such we expect this attractive interaction is the result of electrostatic coupling between charges trapped on both surfaces.

For the majority of curves this was directly followed with hard contact with the surface (Fig. 7.10b). On one site more complex behavior was found. At first contact between the probe and the surface the attractive interaction disappears and a lower attractive force is measured, followed by ringing of the lever (Fig. 7.10c, 7.10d). This is followed by second shorter ranged attractive interaction with weaker strength, after which hard contact with the surface follows.

A possible explanation for this behavior is transfer of material from the surface to the probe upon first contact, which partly equilibrates the charge difference between probe and sample. While the transfer of mass and momentum from the surface to the tip could explaining the presence of ringing, it is unclear why this behavior would be reproduced upon subsequent approaches.

On some sites, repeated force-distance measurements display a decreasing attractive interaction strength per measured curve (Fig. 7.11a), possibly due to equalization of the charge difference between probe and sample or adherence of sample material to the probe.

In contrast to the conical probe measurement, no compacting of the sample material is visible when indenting the dry clay surface with colloidal probes (Fig. 7.11b). This is against expectations, as while the interaction area is bigger than the microsctructure in the lateral directions, this is not true in the normal direction. Compacting of the microstructure in the normal direction should still be visible.

Pressure profile

The pressure per indentation was calculated as explained in section 7.3.4 (Fig. 7.12). As no compacting of the microstructure was visible in the force-distance data, the pressure was calculated without the addition of additional volume due to breaking of the microstructure. The interaction surface was simply taken as $S(\delta) = 2\pi\delta R$.

Some care should be taken when interpreting the found values. The maximally achieved indentation is on the order of 40 nm, much lower than the micrometric roughness of the surface. This makes it probable that only part of the probe touching the surface, and the interaction area is defined by the geometry of the surface instead of the geometry of the probe. Due to this, the interaction area $S(\delta)$ may be significantly overestimated. As such the found pressure does not saturate in any of the measurements, but does reach the order of kPa at maximal indentation.

The average pressure over the 10% of data at the deepest indentation was averaged to determined a single pressure value for each measurement (Fig. 7.13). The resulting values span from 100 Pa to 10 kPa, with a log-normal mean of 2.41 kPa.

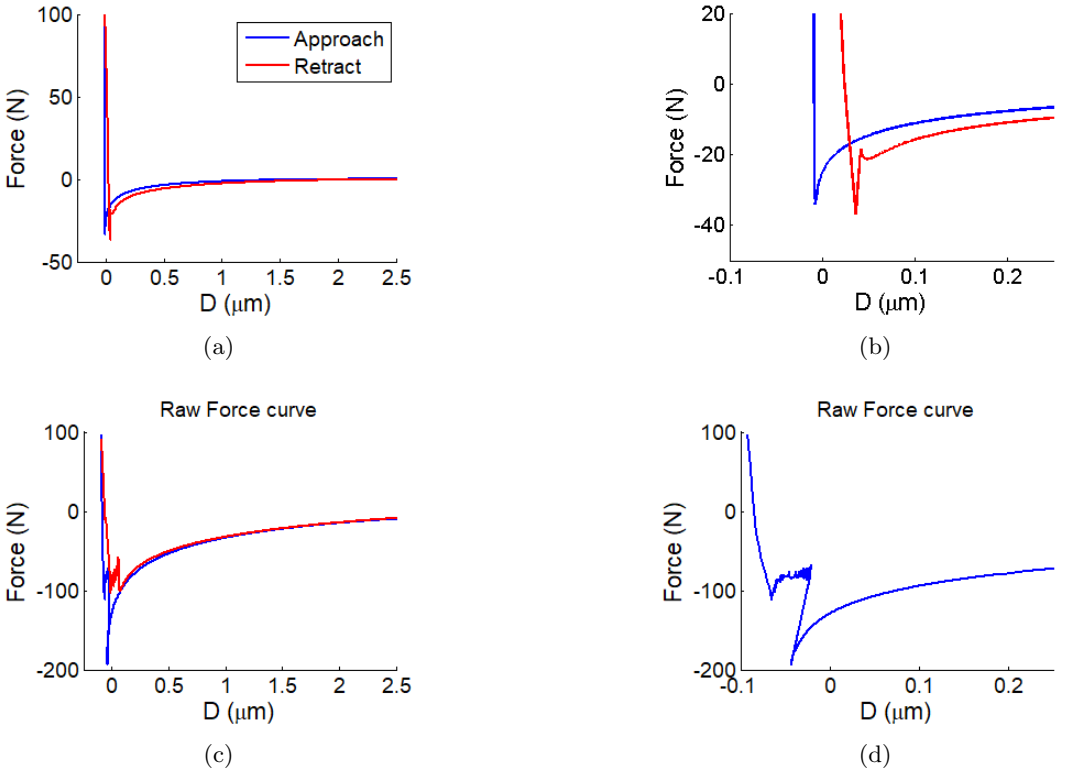

(a) (b) (c) (d)

Figure 7.10: Force-distance measurements on dry clay samples in air using colloidal probes. (a) An attractive interaction that increases for decreasing separation, followed by contact with the sample. (b) close-up of the contact area in (a). (c) Measurements displaying more complicated behavior. (d) close-up of the contact area of (c). The attractive interaction abruptly disappears Close to the surface, followed by ring-down. A subsequent weaker attractive interaction is visible, followed by contact with the surface.

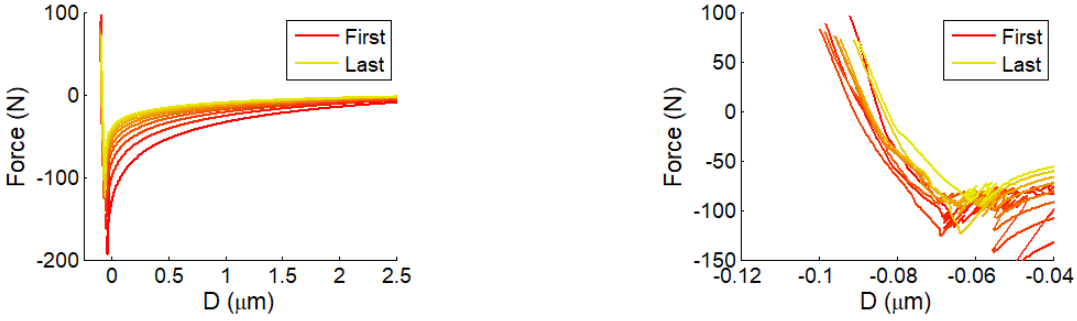

(a) (b)

Figure 7.11: Repeated force-distance measurement performed on dry quick-clay in air at the same location using colloidal AFM probes. (a) The long range attractive interaction diminishes in strength for subsequent measurements. (b) Response in contact remains consistent for subsequent measurements. No compacting of the material or increase in resistance is visible.

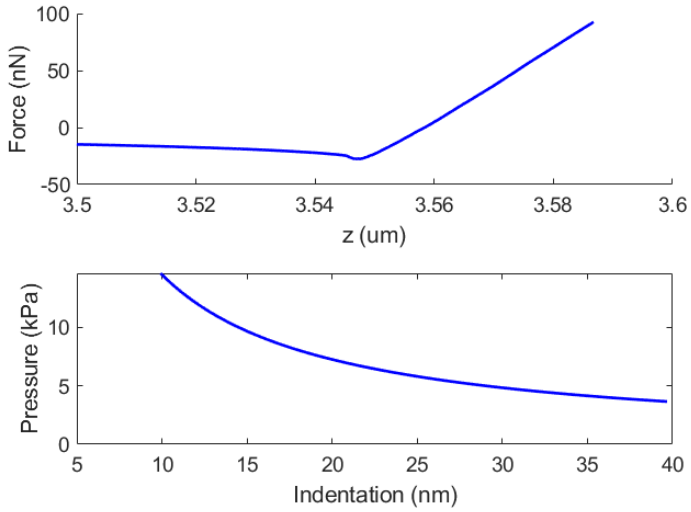

Figure 7.12: Force curve and corresponding pressure profile as measured using a colloidal indenter on a dry quick clay sample in air. The contact point is determined by taking the last local minimum. At small indentations the pressure profile diverges due to underestimation of the interaction surface area.

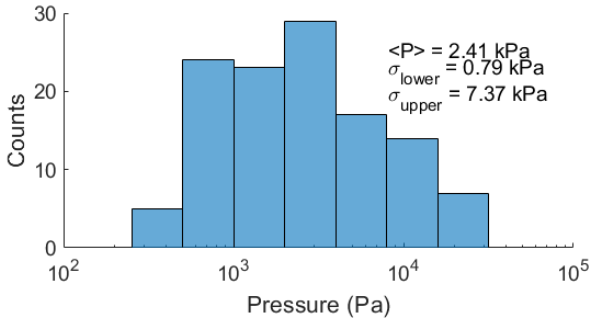

Figure 7.13: Distribution of fitted average pressures at maximum indentation as a function of approach speed, for force-indentation curves as measured on dry clay surface using colloidal indenters in air. The distribution is fitted with a log-normal distribution, finding an average pressure of 2.41 kPa with lower and upper standard deviations of 0.79 and 7.37 kPa.

7.6 Results for clay in deionized water

While the measurement on the dry sample surface make an interesting benchmark for comparison, it is not the natural water saturated state of the material as it is found in the soil. For this reason it was attempted to perform force-distance measurements and image the surface topography of the clay samples submerged in water.

As the pore-water chemistry in the clay microstructure is sensitive to the ionic content, one would ideally submerge the samples in water with ionic content identical to the water found in the clay pores. Determining this content and recreating it in water is however beyond the scope of this manuscript. In order to still submerge the samples in a well defined liquid, deionized water was used.

Performing all the measurements in deionized water comes at the cost of leaching the natural ionic content out of the clay samples. The removal of these ions reduces the screening of electrostatic interactions, significantly weakening the clay material. The results presented in the following section should thus be seen as a "worst-case" scenario. If clay samples could be submerged in such a way that their natural properties are preserved, the material would likely demonstrate a stronger resistance to indentation.

7.6.1 Force volume mapping

Imaging the surface using AM-AFM proved to be difficult. In AM-AFM the amplitude setpoint, usually expressed as a percentage of the free amplitude, determines the interaction strength between sample and probe. If the setpoint is too high, there is not sufficient signal for the PID controller to accurately track the surface. If it is set too low, high forces will be exerted on both the sample and probe, leading to deteriorated sample surfaces and broken probes. For the submerged quick clay surface it was not possible to find a suitable amplitude setpoint, which we suspect this is due to the fragile nature of the material.

An alternative solution was found in Force Volume Mapping (Fig. 7.14). By measuring a full force-volume curve up to a predefined force-setpoint for each pixel, an image of the surface topography can be reconstructed.

The surface of the water saturated clay is similar to that of the dry clay, though the investigated area had a surface roughness of 1.543 µm RMS over a 50x36 µm area, which is higher than that found for dry clay (0.822 µm RMS over 50x50 µm). The top 14 µm of the imaged area was excluded to avoid imaging artifacts affecting the roughness statistics.

The surface did not feature any structural order and no hexagonal structure is visible. This would be in agreement with claims of [172], but it should be noted that the spatial resolution of the measurement is too low to make definite claims. Force volume mapping with higher spatial resolution is possible, but was not attempted.

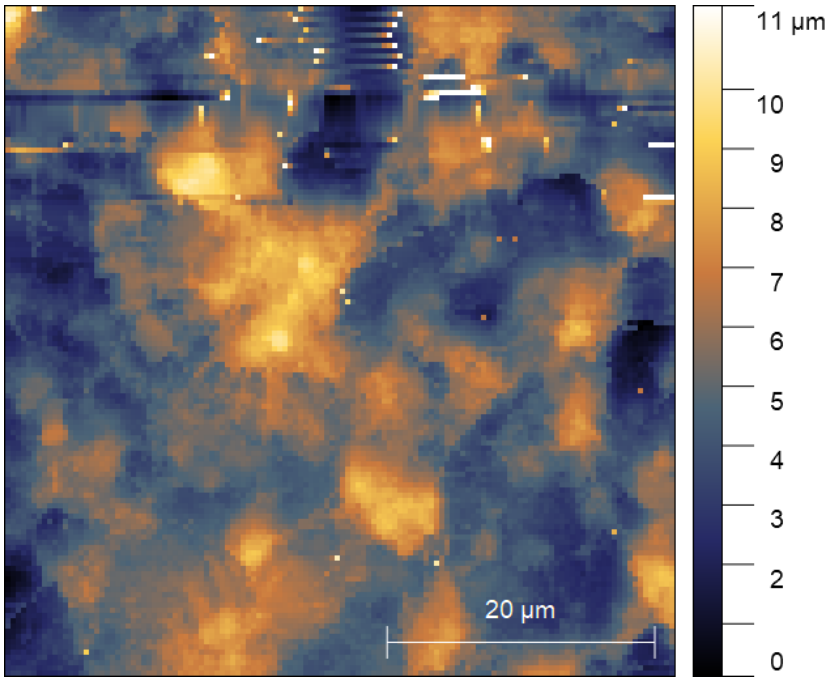

Figure 7.14: FVM height map taken on a clay sample in distilled water using a 4 nN force setpoint. The surface structure of the material is clearly visible. The RMS surface roughness of of the bottom 75% of the map is 1.543 µm over a 50 x 37 µm area.

7.6.2 Force-distance measurements

A large number of force-distance measurements were performed on the saturated clay material. The measurements were performed at various approach speed in an attempt to probe viscoelastic behavior of the material in the available speed range of 1 to 50 µm/s.

As with the dry samples, force-distance measurements were performed using both conical and colloidal probes. Probe-sample interactions on the saturated quick clay partly displayed the same behavior as found on the dry clay, though the material was found to be much more compliant.

Conical probes

The force-distance measurements using conical probes displayed varied behaviour (Fig. 7.15). In some cases a 'clean' transition to stiff contact with the surface was found (Fig. 7.15a), quantitatively comparable to the curves measured on the dry clay surface. In other this was preceded by a region of more compliant material (Fig. 7.15b), while in some cases no stiff contact was reached after a micron of indentation (7.15c). This demonstrates that the material is heterogeneous with spatially varying material properties.

Displacement of sample material was visible for many of the curves (Fig. 7.15d), indicated by the measured force suddenly dropping to a lower value after exerting a certain loading force on the probe. Repeated force-distance measurements on the same location clearly demonstrated compacting of the clay surface (Fig. 7.16), as was the case for the dry clay. The point of contact moved progressively further in the z-direction with each measurement, while the frequency of material displacement decreased for subsequent approaches. As the weaker bonds in the material are broken and more malleable material is displaced, a local structure more resilient to further probing remains.

To determine a distribution of the pressures exerted by the material on the probe, maps of 32 by 32 indentation measurements were performed at 1, 5, 10 and 50 µm/s. Each measurement was performed on a new location sufficiently far removed from previous measurements to make sure the newly probed material was undisturbed. For the conical probes an interdistance of 1 µm was chosen.

Pressure profile

The pressure as a function of indentation was determined using the method described in section 7.3.4 (Fig. 7.17). As the force curves displayed clear compaction of the clay material, the used model included the added volume due to compacted material as previously described in this chapter. The contact point was determined by finding the first data point that exceeded a force threshold of 0.5 nN. As for the measurements in air, the pressure diverts for small indentations due to underestimation of the contact area. For the majority of curves the found pressure saturated at large indentations.

To estimated the variance in the found material response, the 10% of data at the largest indentation for each pressure curve was averaged to attribute a single value to each measurement. The resulting values were roughly log-normally distributed (Fig. 7.18).

No clear correlation of the found pressure with approach speed was found (Table 7.1), indicating there is no viscoelasticity of the material at the speeds presently explored. This substantiates the assumption that the work due to drainage of water from the microstructure is small compared to the work required to break down the microstructure.

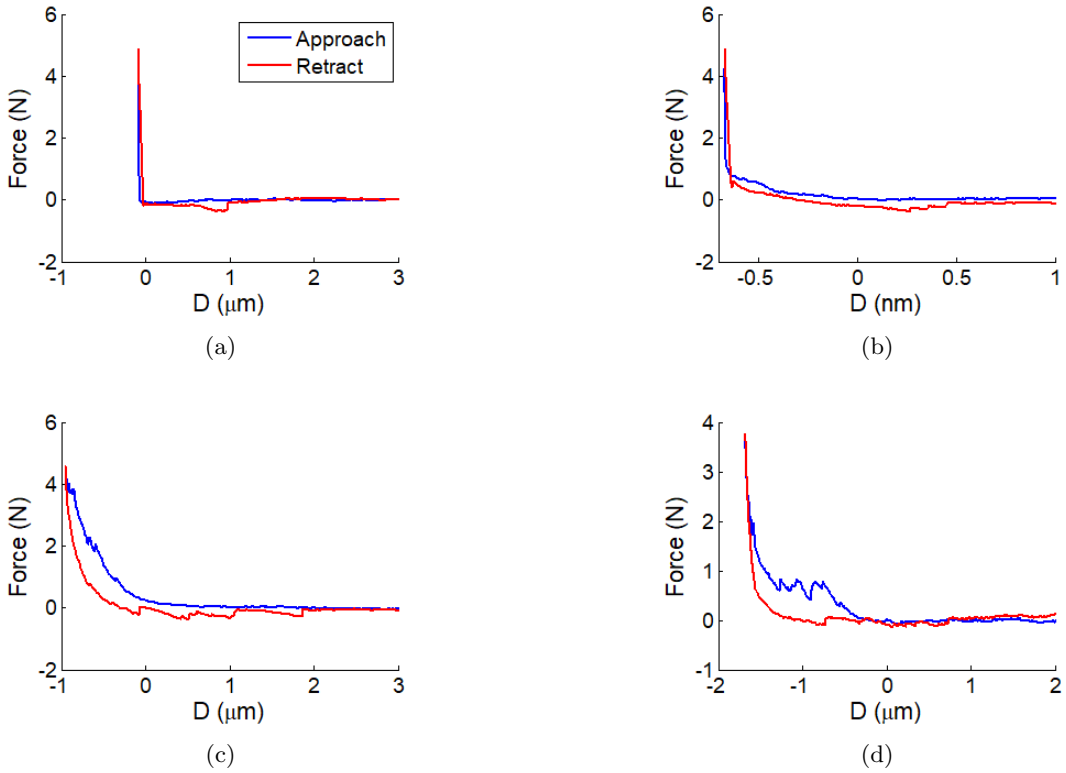

Figure 7.15: Force-distance measurements performed on the water saturated clay surface using conical indenters. (a) Sharp transition into high resistance. (b) High resistance preceded by softer material. (c) Indentation of 1 µm into soft material. (d) Material being displaced upon entry into the clay.

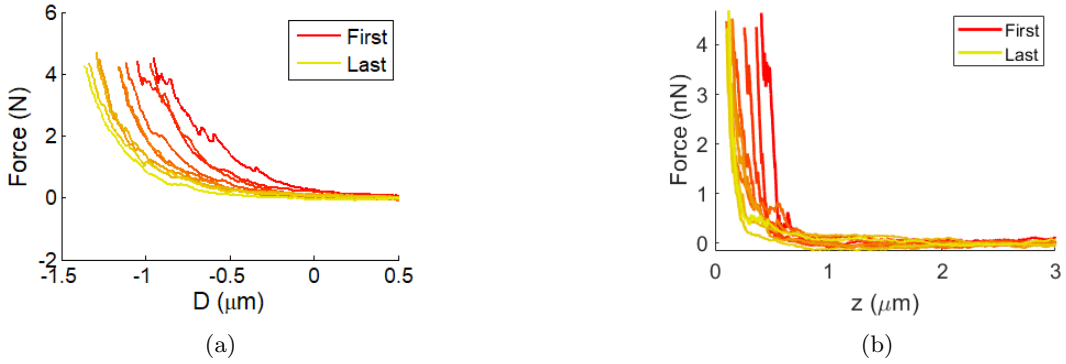

Figure 7.16: Repeated force distance measurements for conical indenters on water saturated clay samples. Repeated indentations were found to compact the clay material, both on (a) more and (b) less compliant areas of the clay surface.

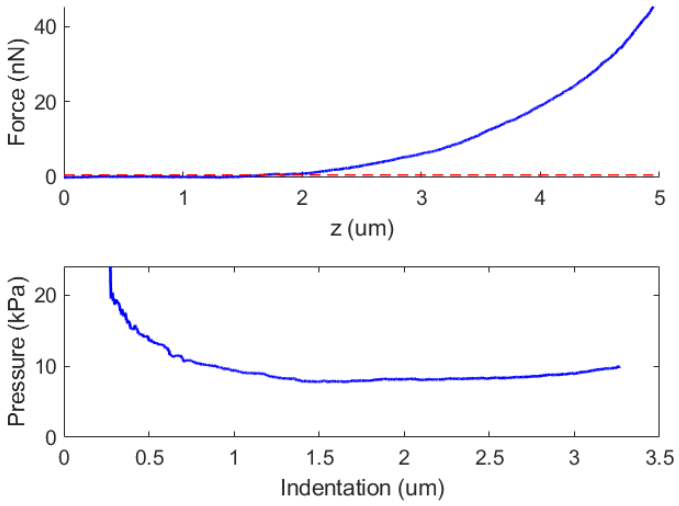

Figure 7.17: Force curve and corresponding pressure profile as measured using a conical indenter on a water saturated quick clay sample. The contact point is determined through a 0.5 nN setpoint. At small indentations the pressure profile diverges due to underestimation of the interaction surface area, but reaches a slowly rising value for larger indentations.

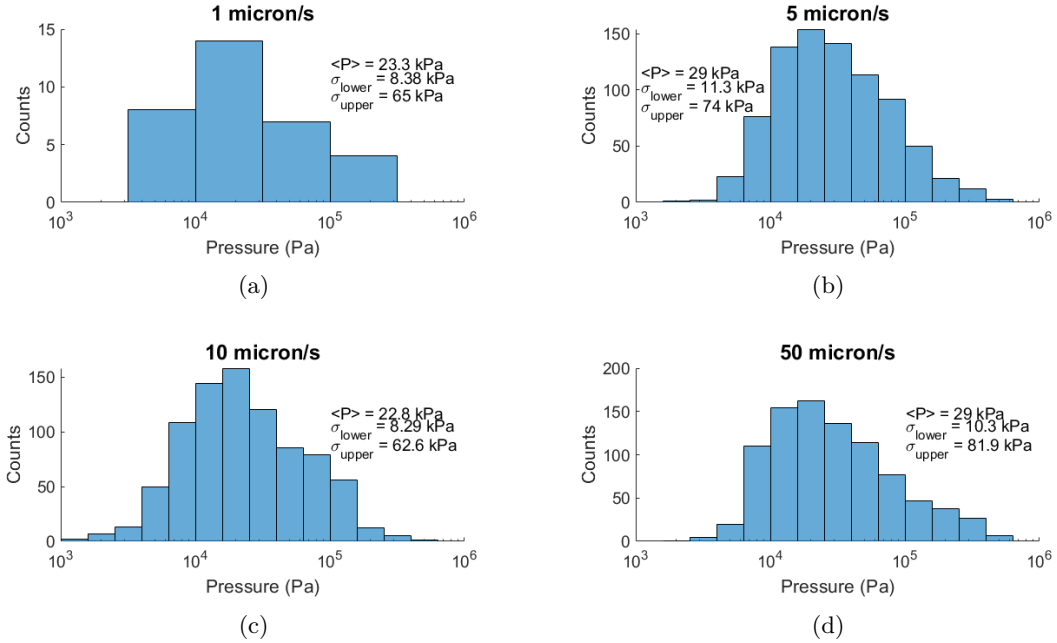

Figure 7.18: Distribution of fitted average pressures at maximum indentation as a function of approach speed, for force-indentation curves as measured on the water saturated clay surface using conical indenters. Each distribution was was fitted with a log-normal distribution, finding the average values and upper and lower standard deviations indicated in table 7.1.

V_{app} (µm/s)	$\langle P \rangle$ (kPa)	σ_{lower} (kPa)	σ_{upper} (kPa)
1	23.3	8.38	65
5	29	11.3	74
10	22.8	8.29	62.6
50	29	10.3	81.9

Table 7.1: Parameters resulting from fitting a log-normal distribution to the found average pressures for conical probes on water saturated clay per approach speed. No significant correlation between average pressure and the explored approach speeds was found.

Colloidal probes

Lastly the saturated clay samples were investigated through microindentation measurements using colloidal probes (Fig. 7.19). The resulting curves yet again revealed varying responses: A direct high resistance to compression (Fig. 7.19a), a slowly rising compliant response followed by higher resistance (Fig. 7.19b), or a compliance persisting up to the chosen force setpoint (Fig. 7.19c).

Displacement of material occurred in a minority of measured curves, indicated by the measured force suddenly dropping to lower value before increasing again. As the probe is bigger than the microstructure in the lateral direction any local displacement of material will be averaged out over the probe surface. This does not hold in the direction normal to the surface, where the probe is still sensitive to collapse of the sample material.

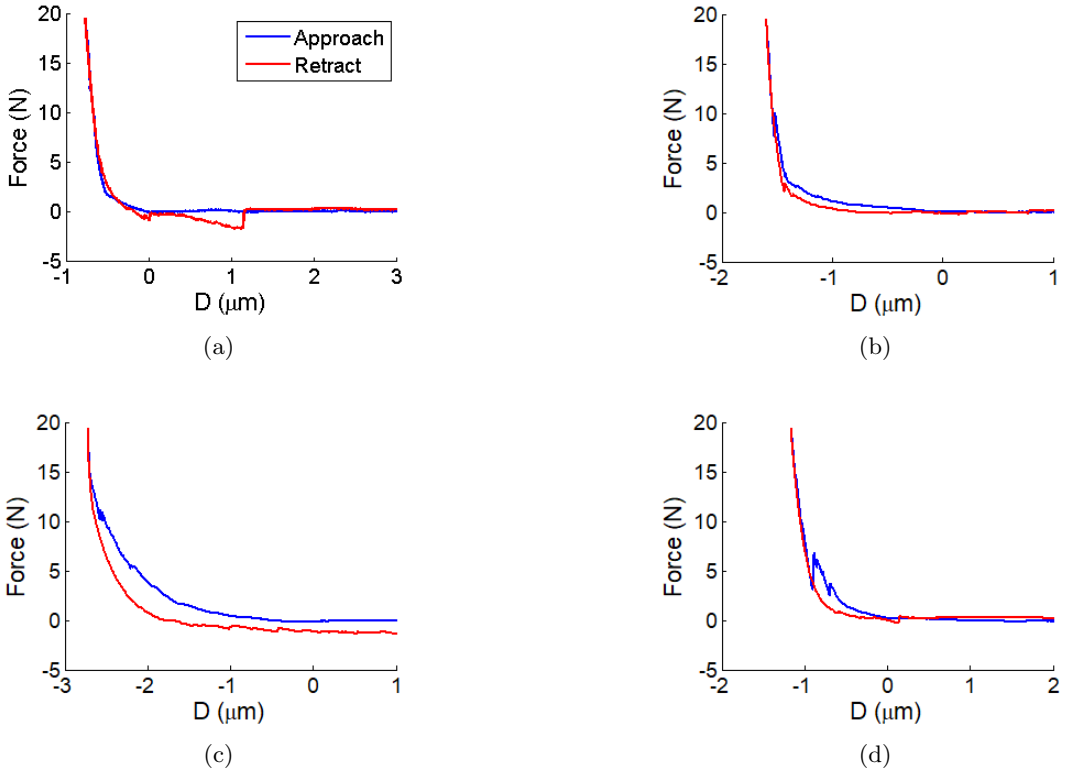

Figure 7.19: Force-distance curves as measured on a water saturated clay surface using colloidal probes. (a) & (b) Layer of compliant material followed by a stiffer response. (c) Continuously rising compliance under compression. (d) Displacement of material upon compression.

Repeated force-distance measurements on the same location revealed compacting off the material, demonstrated by the point of contact moving deeper into the surface for repeated indentations (Fig. 7.20a). The resistance of the material to compression increased for subsequent measurements (Fig. 7.20b).

To determine the variance in the pressure exerted by the water saturated clay sample upon compression, indentation measurements were performed over a map of 32 by 32 point, separated by at least 5 microns to prevent interference between measurements. Each measurement was

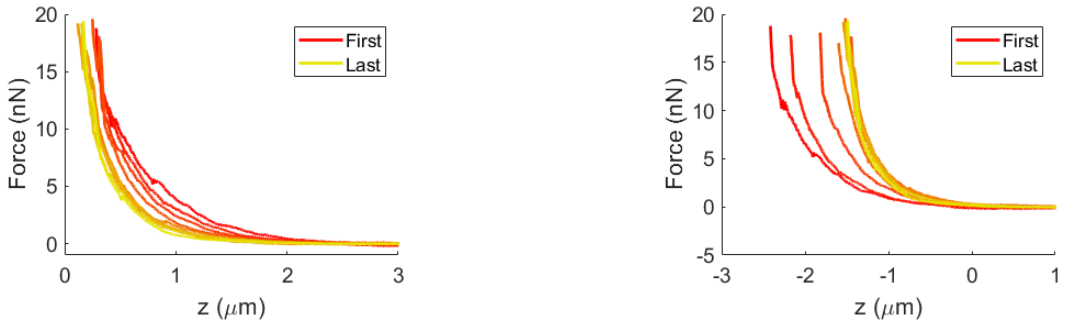

Figure 7.20: (a) Repeated measurements using colloidal probes on the water saturated clay surface show compression of the sample material indicated by the point of contact moving deeper into the sample material. (b) The same data as in (a) with the point of contact taken as 0 for each curve. The sample resistance of the sample material to compression increases for repeated measurements.

performed on a new location not previously disturbed by measurements. Only a single force-distance curve was gathered on each site, so only the response of uncompacted sample material was included.

The resulting average pressures were roughly log-normally distributed (Fig. 7.22). No clear correlation between approach speed and pressure found (Table 7.2), revealing no indication of viscoelastic behavior at the speeds explored.

V_{app} (µm/s)	$\langle P \rangle$ (Pa)	σ_{lower} (Pa)	σ_{upper} (Pa)
1	40.7	18.9	87.7
5	33.8	16.3	69.8
10	36.8	20.5	66.2
20	32.1	16.6	62.1
50	27	15.2	47.8

Table 7.2: Parameters resulting from fitting a log-normal distribution to the found average pressures for colloidal probes on water saturated clay per approach speed. No significant correlation between average pressure and the approach speeds investigated was found.

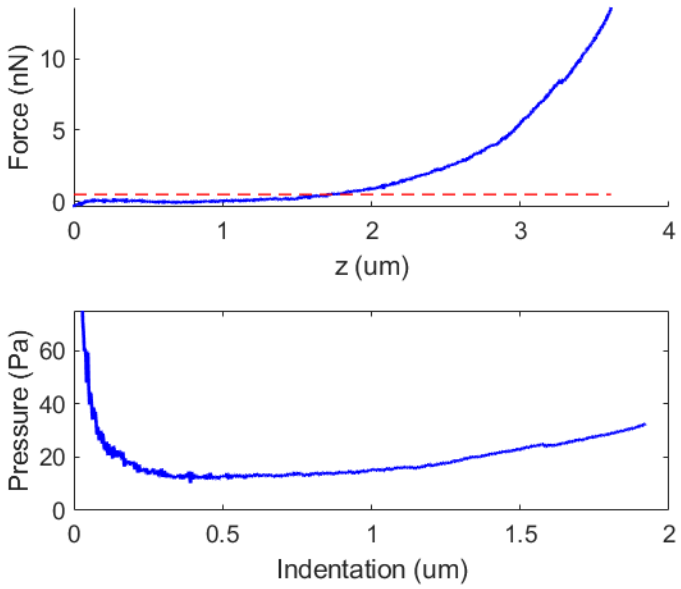

Figure 7.21: Force curve and corresponding pressure profile as measured using a colloidal indenter on a water saturated quick clay sample. The contact point is determined through a 0.5 nN setpoint. At small indentations the pressure profile diverges due to underestimation of the interaction surface area, but reaches a slowly rising value for larger indentations.

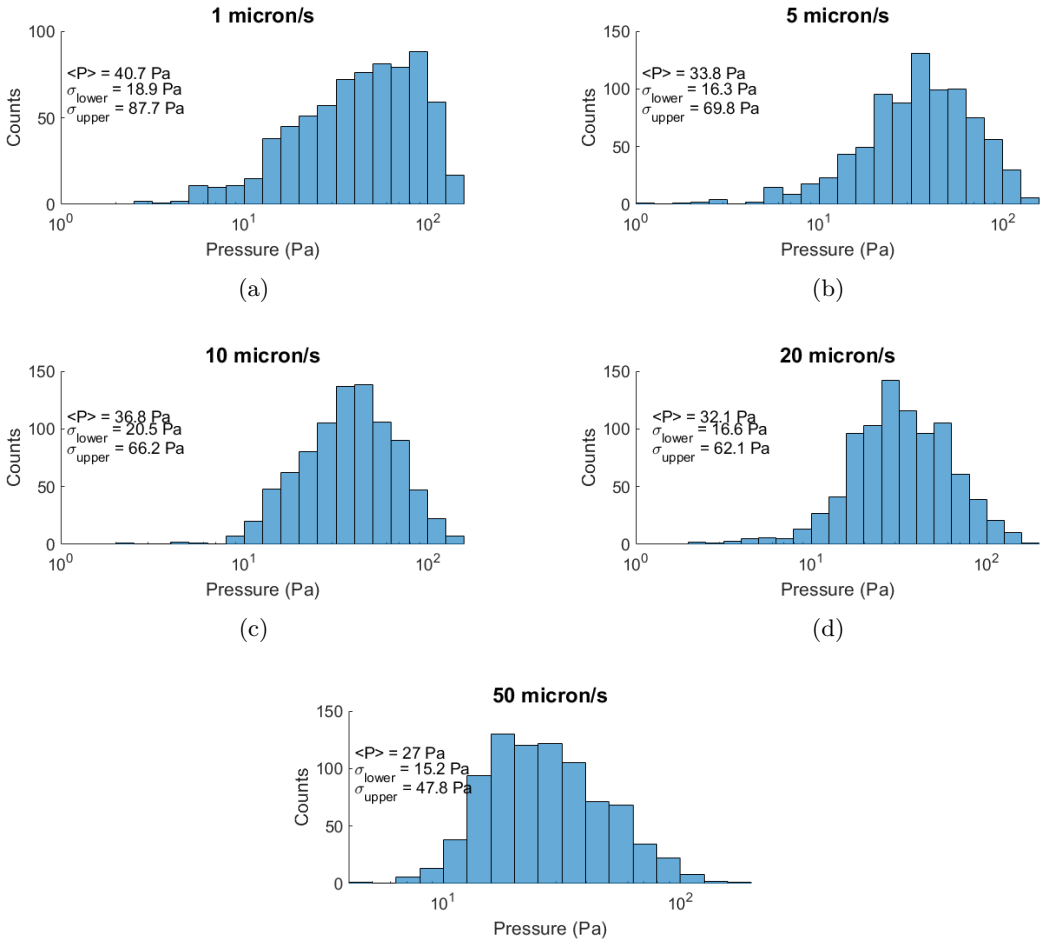

Figure 7.22: Distribution of fitted average pressures at maximum indentation as a function of approach speed, for force-indentation curves as measured on the water saturated clay surface using colloidal indenters. Each distribution was was fitted with a log-normal distribution, finding the average values and upper and lower standard deviations indicated in table 7.3.

7.7 Discussion

When comparing the measurements performed on the clay material in its dry and water saturated state the dry clay material resists compression three to five orders of magnitude more strongly than the water saturated clay (Table 7.3). This is not unexpected as we believe the microstructure of the water saturated material is held together by ionic bonds in between the clay platelets, while the response of the dry material is likely the result of solid-solid friction in between the particles. It is clear that the dry and water saturated clay system have different properties and measurements of the dry clay properties can not be used to predict the behavior the clay in a water saturated state.

$\langle P \rangle$	Dry	Water Sat.
Conical	0.1 GPa	10 kPa
Colloidal	1 kPa	10 Pa
Ratio	10^5	10^3

Table 7.3: Order of magnitude with which the clay material resists indentation for each of the scenarios explored in this manuscript.

The response of the clay material equally depends on the lengthscale at which it is probed. Sharp conical probes are sensitive to the local material properties of the clay microstructure, which are determined by the strength at with which individual platelets are bound within the microstructure. Colloidal probes that have an area of interaction larger than the microstructure will find less resistance of the material as the response is averaged out over the interaction surface (Fig. 7.23).

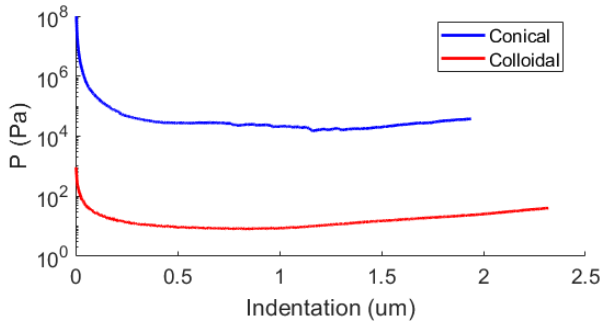

Figure 7.23: Comparison of typical pressure profiles found for conical and colloidal indenters on water saturated clay samples.

On the dry clay material this difference seems to be even more pronounced, but here the level of indentation of the surface is limited and the model of a colloid indenting a half plane likely breaks down. It is more likely that the colloid makes contact with a limited number of asperities, leading to overestimation of the interaction area, making the material appear to be more compliant.

Samples of similar natural clay material were found to have a strength on the 10 to 100 kPa in macroscopic experiments using oedometers. It should be noted that due to the storage in deionized water, our investigated samples are likely weaker relative to the natural state. [189] While the experiments using conical indenters replicate the values found for the natural clay

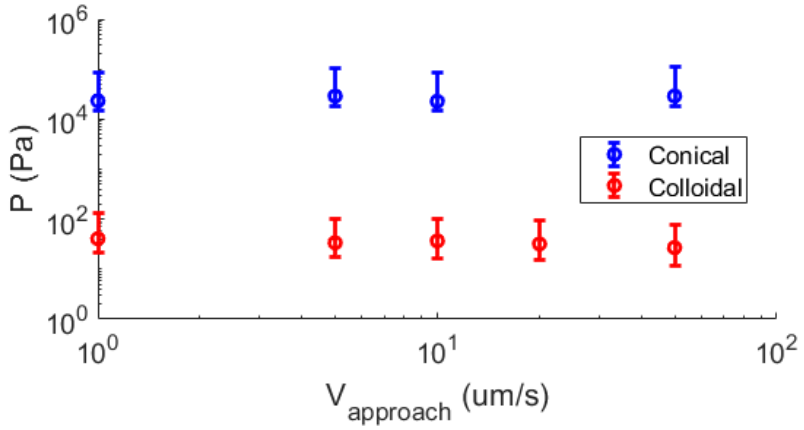

Figure 7.24: Found average pressure near maximum indentation for indentation measurements on the water saturated clay surface as a function of approach speed for both conical and colloidal indenters

material, the found values when using colloidal indenters are likely to more closely resemble the values found if macroscopic experiments had been performed on the sample material.

7.7.1 Bond density

As proposed in section 7.3.4 the pressure exerted by the water saturated clay material upon indentation can be related to an estimation of the bond energy density of the material. This interpretation is most applicable to the case of colloidal probes as the large interaction area leads to an averaging over the clay microstructure.

As the energy required to break a bond must be between 1 eV (covalent bond) and 0.025 eV (k_bT), we can make a rough estimate the bond density by taking $\epsilon_b = 0.1$eV. For a pressure of 10 Pa this estimates the bond density at 624 µm^{-3}, roughly taken a bond per 100 cubic nanometers. These bonds would only be present at platelet-platelet interfaces. Considering the structure as visible in the SEM images of figure 7.2 and the knowledge that about $\frac{2}{3}$ of the clay volume is water, this is not an unreasonable value. While the actual average bond energy might be an order of magnitude lower or higher, due to the cubic scaling the found bond density will not change significantly.

7.7.2 Viscoelasticity

As the clay material consists of a network of silica platelets filled with water, it is expected that at sufficiently short timescale the drainage speed of the water in the network will contribute to the resistance of the material to compression. No correlation between material response and approach speed was found for approach speeds between 1 to 50 µm (Fig. 7.24), for both conical and colloidal indenters. This is in agreement with a structure that is more than $\frac{2}{3}$ water by volume.

To further investigate possible viscoelastic properties of the material, it would be interesting to make use of dynamic measuring methods that utilize the harmonic oscillator properties of the AFM cantilever. Using such techniques, one can vary the excitation frequency ω and amplitude

A of the probe oscillation, creating an effective approach velocity of $\nu \approx \frac{A}{2\pi\omega}$. This would significantly enlarge the range of drainage speeds that can be explored.

7.7.3 Topographic imaging of the clay microstructure

As demonstrated, Force Volume Mapping is an effective technique to visualize the clay microstructure in a liquid environment. Albeit being a slow technique, it is conceptually straightforward, works well on soft materials and is compatible with the high surface roughness of the clay. Some care has to be taken when interpreting the result, as for each pixel one measures the height at which a certain force setpoint is reached to construct a topographic image of the surface, which does not deconvolute material indentation from the measured height. When a high force setpoint is chosen, the surface of softer material will have a lower apparent height.

An additional benefit of FVM is that the force-distance data of each pixel also contains the force-indentation data. Although not performed in the presented work, correlations between position and material response can be made. This allows material properties to be ascribed to specific parts of the microstructure, which can be usefull considering the heterogenous nature of extracted natural clay samples.

As AFM is compatible with water, the natural microstructure of clay can be investigated without the requirement of vitrifying the water through plunge-freezing or HPF. As such AFM can contribute in determining the validity of the various models for the natural microstructure of water saturated clay in existence, though this would require the control of additional experimental parameters.

7.8 Conclusions and Outlook

We have demonstrated that AFM can be used as a tool to probe the properties of water saturated clay materials, both at lengthscales below and above the typical size of the clay microstructure. Room temperature imaging of the clay topography at the microscale has been demonstrated, both in a dry and liquid environment.

The clay surface was found to have a surface roughness on the order of microns, both in the dry and water saturated state. Dry clay material resisted compression in the kPa to GPa range, much stronger than the water saturated clay, which only resisted in the Pa to kPa range.

For both dry and water saturated clay, resistance of the material to indentation was found to be higher below the lengthscale of the microstructure, as probed with conical indenters, than above this lengthscale, as probed with colloidal indenters.

To expand upon the current work, further control of the experimental parameters is required. The first is homogeneity of the clay material, as the natural clay samples include an uncontrolled fraction of non-clay particles such as silt. Using recently developed techniques it is possible to remove such fractions from the clay material and reconstitute the remainder into a new sensitive material through flocculated sedimentation and leaching in geotechnical centrifuge. [191]

The method used in this work to cleave the clay from the bulk, slicing with a thin steel wire, could possibly alter the state of the surface from its bulk form prior to measuring, especially considering the softness of the material. It should be confirmed that no such alterations take place when using the current method or a better cleaving method needs to be employed.

Another important parameter to control, the solute content of the water in which the clay material is submerged. Ideally this would have the exact same composition as the water naturally present inside the bulk clay, which is certainly different from the deionized water used in the current study. Assuming the solute content of the water does not significantly vary throughout a single sample, it should be possible to determine which concentrations of solutes

are present. Water with equal contents can then be recreated to submerge the clay material for AFM measurements.

These improvements are straightforward to implement and not new to the field. As such we are confident the currently presented work will form a foundation for further investigations into the clay microstructure and other complex material.

Bibliography

[1] Donald Ingber. Mechanobiology and diseases of mechanotransduction. *Annals of Medicine*, 35(8):564–577, January 2003.

[2] Viola Vogel and Michael Sheetz. Local force and geometry sensing regulate cell functions. *Nat Rev Mol Cell Biol*, 7(4):265–275, April 2006.

[3] A. Wayne Orr, Brian P. Helmke, Brett R. Blackman, and Martin A. Schwartz. Mechanisms of Mechanotransduction. *Developmental Cell*, 10(1):11–20, January 2006.

[4] C. S. Chen. Mechanotransduction - a field pulling together? *Journal of Cell Science*, 121(20):3285–3292, October 2008.

[5] Xin Wei, Xue Yang, Zhi-peng Han, Fang-fang Qu, Li Shao, and Yu-fang Shi. Mesenchymal stem cells: a new trend for cell therapy. *Acta Pharmacol Sin*, 34(6):747–754, June 2013.

[6] D. E. Discher, D. J. Mooney, and P. W. Zandstra. Growth Factors, Matrices, and Forces Combine and Control Stem Cells. *Science*, 324(5935):1673–1677, June 2009.

[7] Gwendolen C. Reilly and Adam J. Engler. Intrinsic extracellular matrix properties regulate stem cell differentiation. *Journal of Biomechanics*, 43(1):55–62, January 2010.

[8] Adam J. Engler, Shamik Sen, H. Lee Sweeney, and Dennis E. Discher. Matrix Elasticity Directs Stem Cell Lineage Specification. *Cell*, 126(4):677–689, August 2006.

[9] Ruyue Xue, Julie Yi-Shuan Li, Yiting Yeh, Li Yang, and Shu Chien. Effects of matrix elasticity and cell density on human mesenchymal stem cells differentiation: msc differentiation by elasticity and density. *J. Orthop. Res.*, 31(9):1360–1365, September 2013.

[10] Angelo S. Mao, Jae-Won Shin, and David J. Mooney. Effects of substrate stiffness and cell-cell contact on mesenchymal stem cell differentiation. *Biomaterials*, 98:184–191, August 2016.

[11] Matthew G. Haugh, Ted J. Vaughan, Christopher M. Madl, Rosanne M. Raftery, Laoise M. McNamara, Fergal J. O'Brien, and Sarah C. Heilshorn. Investigating the interplay between substrate stiffness and ligand chemistry in directing mesenchymal stem cell differentiation within 3D macro-porous substrates. *Biomaterials*, 171:23–33, July 2018.

[12] Krishanu Saha, Albert J. Keung, Elizabeth F. Irwin, Yang Li, Lauren Little, David V. Schaffer, and Kevin E. Healy. Substrate Modulus Directs Neural Stem Cell Behavior. *Biophysical Journal*, 95(9):4426–4438, November 2008.

[13] Yang-Kao Wang and Christopher S. Chen. Cell adhesion and mechanical stimulation in the regulation of mesenchymal stem cell differentiation. *J. Cell. Mol. Med.*, 17(7):823–832, July 2013.

[14] Andreas Engel and Daniel J Müller. Observing single biomolecules at work with the atomic force microscope. *nature structural biology*, 7(9):4, 2000.

[15] Kefeng Ren, Thomas Crouzier, Christian Roy, and Catherine Picart. Polyelectrolyte Multilayer Films of Controlled Stiffness Modulate Myoblast Cell Differentiation. *Adv. Funct. Mater.*, 18(9):1378–1389, April 2008.

[16] Claire Monge, Naresh Saha, Thomas Boudou, Cuauhtemoc Pózos-Vásquez, Virginie Dulong, Karine Glinel, and Catherine Picart. Rigidity-Patterned Polyelectrolyte Films to Control Myoblast Cell Adhesion and Spatial Organization. *Adv. Funct. Mater.*, 23(27):3432–3442, July 2013.

[17] Shan Li, Feng Zhao, Yuewei Zhan, Xiaoyi Liu, Tingting Hun, Haokang Zhang, Changjun Qiu, Jingwen He, Zongchun Yi, Yan Sun, and Yubo Fan. How Deep Might Myoblasts Sense: The Effect of Substrate Stiffness and Thickness on the Behavior of Myoblasts. *J. Med. Biol. Eng.*, 38(4):596–606, August 2017.

[18] Adam J. Engler, Maureen A. Griffin, Shamik Sen, Carsten G. Bönnemann, H. Lee Sweeney, and Dennis E. Discher. Myotubes differentiate optimally on substrates with tissue-like stiffness. *The Journal of Cell Biology*, 166(6):877–887, September 2004.

[19] Ilaria E. Palamà, Addolorata M. L. Coluccia, Giuseppe Gigli, and Mathis Riehle. Modulation of alignment and differentiation of skeletal myoblasts by biomimetic materials. *Integr. Biol.*, 4(10):1299, 2012.

[20] Jason A. Burdick, Ali Khademhosseini, and Robert Langer. Fabrication of Gradient Hydrogels Using a Microfluidics/Photopolymerization Process. *Langmuir*, 20(13):5153–5156, June 2004.

[21] Brett Isenberg, Paul DiMilia, Walker Matthew, Sooyoung Kim, and Joyce Wong. Vascular smooth muscle cell durotaxis depends on substrate stiffness gradient strength. *Biophysical Journal*, 97:1313–1322, September 2009.

[22] Justin R. Tse and Adam J. Engler. Stiffness Gradients Mimicking In Vivo Tissue Variation Regulate Mesenchymal Stem Cell Fate. *PLoS ONE*, 6(1):e15978, January 2011.

[23] Sarah E. Cross, Yu-Sheng Jin, Jianyu Rao, and James K. Gimzewski. Nanomechanical analysis of cells from cancer patients. *Nature Nanotech*, 2(12):780–783, December 2007.

[24] Andreas Stylianou, Malgorzata Lekka, and Triantafyllos Stylianopoulos. AFM assessing of nanomechanical fingerprints for cancer early diagnosis and classification: from single cell to tissue level. *Nanoscale*, 10(45):20930–20945, 2018.

[25] V. Swaminathan, K. Mythreye, E. T. O'Brien, A. Berchuck, G. C. Blobe, and R. Superfine. Mechanical Stiffness Grades Metastatic Potential in Patient Tumor Cells and in Cancer Cell Lines. *Cancer Research*, 71(15):5075–5080, August 2011.

[26] Małgorzata Lekka, Dorota Gil, Katarzyna Pogoda, Joanna Dulińska-Litewka, Robert Jach, Justyna Gostek, Olesya Klymenko, Szymon Prauzner-Bechcicki, Zbigniew Stachura, Joanna Wiltowska-Zuber, Krzysztof Okoń, and Piotr Laidler. Cancer cell detection in

tissue sections using AFM. *Archives of Biochemistry and Biophysics*, 518(2):151–156, February 2012.

[27] S. Chien, J. Dormandy, E. Ernst, and A. Matrai. *Clinical Hemorheology*. Springer Science+Business Media B.V., 1986. OCLC: 940688916.

[28] J. Dupire, M. Socol, and A. Viallat. Full dynamics of a red blood cell in shear flow. *Proceedings of the National Academy of Sciences*, 109(51):20808–20813, December 2012.

[29] M. Musielak. Red blood cell-deformability measurement: Review of techniques. *Clinical Hemorheology and Microcirculation*, 42(1):47–64, 2009.

[30] Kristen E. Bremmell, Allan Evans, and Clive A. Prestidge. Deformation and nano-rheology of red blood cells: An AFM investigation. *Colloids and Surfaces B: Biointerfaces*, 50(1):43–48, June 2006.

[31] F. H. Bosch, J. M. Werre, L Schipper, B. Roerdinkholder-Stoelwinder, T. Huls, F.L.A. Willekens, G. Wichers, and M. R. Halie. Determinants of red blood cell deformability in relation to cell age. *European Journal of Haematology*, 52(1):35–41, 1994.

[32] Luca Lanotte, Giovanna Tomaiuolo, Chaouqi Misbah, Lionel Bureau, and Stefano Guido. Red blood cell dynamics in polymer brush-coated microcapillaries: A model of endothelial glycocalyx *in vitro*. *Biomicrofluidics*, 8(1):014104, January 2014.

[33] Heather S. Davies, Delphine Débarre, Nouha El Amri, Claude Verdier, Ralf P. Richter, and Lionel Bureau. Elastohydrodynamic Lift at a Soft Wall. *Phys. Rev. Lett.*, 120(19):198001, May 2018.

[34] Heinrich Hertz. Ueber die Berührung fester elastischer Körper. *J. Reine Angew. Math.*, 92:156–171, 1881.

[35] K. L. Johnson, K. Kendall, and A. D. Roberts. Surface Energy and the Contact of Elastic Solids. *Proceedings of the Royal Society A: Mathematical, Physical and Engineering Sciences*, 324(1558):301–313, September 1971.

[36] B.V. Derjaguin, V.M. Muller, and Yu. P. Toporov. Effect of contact derformation on the adhesion of particles. *Journal of Colloid and Interface Science*, 53(2):314–326, November 1975.

[37] Kenneth R. Shull. Contact mechanics and the adhesion of soft solids. *Materials Science and Engineering: R: Reports*, 36(1):1–45, January 2002.

[38] D. F. Gerson and J. E. Zajic. The Biophysics of Cellular Adhesion. In K. Venkatsubramanian, editor, *Immobilized Microbial Cells*, volume 106, pages 29–57. American Chemical Society, Washington, D.C., August 1979.

[39] P.K Sharma and K Hanumantha Rao. Analysis of different approaches for evaluation of surface energy of microbial cells by contact angle goniometry. *Advances in Colloid and Interface Science*, 98(3):341–463, August 2002.

[40] M. Deruelle, H. Hervet, G. Jandeau, and L. Léger. Some remarks on JKR experiments. *Journal of Adhesion Science and Technology*, 12(2):225–247, January 1998.

[41] P M McGuiggan, J S Wallace, D T Smith, I Sridhar, Z W Zheng, and K L Johnson. Contact mechanics of layered elastic materials: experiment and theory. *J. Phys. D: Appl. Phys.*, 40(19):5984–5994, October 2007.

[42] Robert W. Style, Callen Hyland, Rostislav Boltyanskiy, John S. Wettlaufer, and Eric R. Dufresne. Surface tension and contact with soft elastic solids. *Nat Commun*, 4(1):2728, December 2013.

[43] Katharine E. Jensen, Raphael Sarfati, Robert W. Style, Rostislav Boltyanskiy, Aditi Chakrabarti, Manoj K. Chaudhury, and Eric R. Dufresne. Wetting and phase separation in soft adhesion. *Proc Natl Acad Sci USA*, 112(47):14490–14494, November 2015.

[44] J. P. Aimé, R. Boisgard, L. Nony, and G. Couturier. Influence of noncontact dissipation in the tapping mode: Attempt to extract quantitative information on the surface properties with the local force probe method. *The Journal of Chemical Physics*, 114(11):4945–4954, March 2001.

[45] C. Tardivat, H. Hervet, and L. Léger. Adhesion evaluation for a stratified system in JKR geometry. *Journal of Adhesion Science and Technology*, 15(9):1055–1078, January 2001.

[46] D. Johannsmann. The glass transition and contact mechanical experiments on polymer surfaces. *Eur. Phys. J. E*, 8(2):257–259, May 2002.

[47] P Mary, A Chateauminois, and C Fretigny. Deformation of elastic coatings in adhesive contacts with spherical probes. *J. Phys. D: Appl. Phys.*, 39(16):3665–3673, August 2006.

[48] E. Gacoin, C. Fretigny, A. Chateauminois, A. Perriot, and E. Barthel. Measurement of the mechanical properties of thin films mechanically confined within contacts. *Tribol Lett*, 21(3):245–252, March 2006.

[49] Thomas Salez, Michael Benzaquen, and Élie Raphaël. From adhesion to wetting of a soft particle. *Soft Matter*, 9(45):10699, 2013.

[50] Chung-Yuen Hui, Tianshu Liu, Thomas Salez, Elie Raphael, and Anand Jagota. Indentation of a rigid sphere into an elastic substrate with surface tension and adhesion. *Proc. R. Soc. A*, 471(2175):20140727, March 2015.

[51] Bruno Andreotti, Oliver Bäumchen, François Boulogne, Karen E. Daniels, Eric R. Dufresne, Hugo Perrin, Thomas Salez, Jacco H. Snoeijer, and Robert W. Style. Solid capillarity: when and how does surface tension deform soft solids? *Soft Matter*, 12(12):2993–2996, 2016.

[52] Samuel Leroy, Audrey Steinberger, Cécile Cottin-Bizonne, Frédéric Restagno, Liliane Léger, and Élisabeth Charlaix. Hydrodynamic Interaction between a Spherical Particle and an Elastic Surface: A Gentle Probe for Soft Thin Films. *Phys. Rev. Lett.*, 108(26):264501, June 2012.

[53] Frédéric Restagno, Jérôme Crassous, Élisabeth Charlaix, Cécile Cottin-Bizonne, and Michel Monchanin. A new surface forces apparatus for nanorheology. *Review of Scientific Instruments*, 73(6):2292–2297, June 2002.

[54] S. Leroy and E. Charlaix. Hydrodynamic interactions for the measurement of thin film elastic properties. *J. Fluid Mech.*, 674:389–407, May 2011.

[55] Wenhai Han, S. M. Lindsay, and Tianwei Jing. A magnetically driven oscillating probe microscope for operation in liquids. *Appl. Phys. Lett.*, 69(26):4111–4113, December 1996.

[56] J. Kokavecz and A. Mechler. Investigation of fluid cell resonances in intermittent contact mode atomic force microscopy. *Appl. Phys. Lett.*, 91(2):023113, July 2007.

[57] G. Binnig, C. F. Quate, and Ch. Gerber. Atomic Force Microscope. *Phys. Rev. Lett.*, 56(9):930–933, March 1986.

[58] Hans-Jürgen Butt, Brunero Cappella, and Michael Kappl. Force measurements with the atomic force microscope: Technique, interpretation and applications. *Surface Science Reports*, 59(1-6):1–152, October 2005.

[59] Seizō Morita, Franz J. Giessibl, and Roland Wiesendanger, editors. *Noncontact atomic force microscopy. Vol. 2.* NanoScience and technology. Springer, Berlin, 1. aufl edition, 2009. OCLC: 502397419.

[60] Ricardo Garcıa. *Amplitude Modulation Atomic Force Microscopy.* Wiley-VCH, 1 edition, 2010.

[61] S. Morita, E Meyer, and R. Wiesendanger. *Noncontact atomic force microscopy. Volume 1.* Springer, Place of publication not identified, 2013. OCLC: 925406779.

[62] Seizō Morita, Franz J. Gießibl, Ernst Meyer, and Roland Wiesendanger, editors. *Noncontact atomic force microscopy. Volume 3.* NanoScience and technology. Springer, Cham, 2015. OCLC: 918469789.

[63] Bert Voigtländer. *Scanning probe microscopy.* Springer Berlin Heidelberg, New York, NY, 2015.

[64] Ronald G. Reifenberger. *Fundamentals of atomic force microscopy.* Number volume 4 in Lessons from nanoscience: a lecture note series. World Scientific, [Hackensack] New Jersey, 2016.

[65] Nuno C. Santso and Filomena A. Carvalho. *Atomic force microscopy: methods and protocols.* Springer Science+Business Media, New York, NY, 2018.

[66] Kousuke Yokoyama, Taketoshi Ochi, Takayuki Uchihashi, Makoto Ashino, Yasuhiro Sugawara, Nobuhito Suehira, and Seizo Morita. Optical beam deflection noncontact atomic force microscope optimized with three-dimensional beam adjustment mechanism. *Review of Scientific Instruments*, 71(1):128–132, January 2000.

[67] D. Rugar, H. J. Mamin, R. Erlandsson, J. E. Stern, and B. D. Terris. Force microscope using a fiber-optic displacement sensor. *Review of Scientific Instruments*, 59(11):2337–2340, November 1988.

[68] Haider I. Rasool, Paul R. Wilkinson, Adam Z. Stieg, and James K. Gimzewski. A low noise all-fiber interferometer for high resolution frequency modulated atomic force microscopy imaging in liquids. *Review of Scientific Instruments*, 81(2):023703, February 2010.

[69] Z. M. Zhang, Q. An, J. W. Li, and W. J. Zhang. Piezoelectric friction–inertia actuator—a critical review and future perspective. *Int J Adv Manuf Technol*, 62(5-8):669–685, September 2012.

[70] Neal B. Hubbard, Martin L. Culpepper, and Larry L. Howell. Actuators for Micropositioners and Nanopositioners. *Applied Mechanics Reviews*, 59(6):324–334, November 2006.

[71] Abdelhamid Maali and Rodolphe Boisgard. Precise damping and stiffness extraction in acoustic driven cantilever in liquid. *Journal of Applied Physics*, 114(14):144302, October 2013.

[72] I-Chen Chen, Li-Han Chen, Xiang-Rong Ye, Chiara Daraio, Sungho Jin, Christine A. Orme, Arjan Quist, and Ratnesh Lal. Extremely sharp carbon nanocone probes for atomic force microscopy imaging. *Appl. Phys. Lett.*, 88(15):153102, April 2006.

[73] Kazi M. Zakir Hossain, Uresha Patel, and Ifty Ahmed. Development of microspheres for biomedical applications: a review. *Prog Biomater*, 4(1):1–19, March 2015.

[74] P. J. van Zwol, G. Palasantzas, M. van de Schootbrugge, J. Th. M. de Hosson, and V. S. J. Craig. Roughness of Microspheres for Force Measurements. *Langmuir*, 24(14):7528–7531, July 2008.

[75] F. J. Giessibl. Atomic Resolution of the Silicon (111)-(7x7) Surface by Atomic Force Microscopy. *Science*, 267(5194):68–71, January 1995.

[76] Franz J. Giessibl. Forces and frequency shifts in atomic-resolution dynamic-force microscopy. *Phys. Rev. B*, 56(24):16010–16015, December 1997.

[77] J. P. Cleveland, B. Anczykowski, A. E. Schmid, and V. B. Elings. Energy dissipation in tapping-mode atomic force microscopy. *Appl. Phys. Lett.*, 72(20):2613–2615, May 1998.

[78] Peter M. Hoffmann, Ahmet Oral, Ralph A. Grimble, H. Özgür özer, Steve Jeffery, and John B. Pethica. Direct measurement of interatomic force gradients using an ultra-low-amplitude atomic force microscope. *Proc. R. Soc. Lond. A*, 457(2009):1161–1174, May 2001.

[79] Shivprasad Patil, George Matei, Hang Dong, Peter M. Hoffmann, Mustafa Karaköse, and Ahmet Oral. A highly sensitive atomic force microscope for linear measurements of molecular forces in liquids. *Review of Scientific Instruments*, 76(10):103705, October 2005.

[80] Mario S. Rodrigues, Luca Costa, Joël Chevrier, and Fabio Comin. System analysis of force feedback microscopy. *Journal of Applied Physics*, 115(5):054309, February 2014.

[81] Luca Costa and Mario S. Rodrigues. Small amplitude Dynamic AFM: quantifying interactions with different tip detection and excitation schemes in presence of additional resonances. *Beilstein J. Nanotechnol.*, 6:420–427, February 2015. arXiv: 1404.5277.

[82] Simon Carpentier, Mario S. Rodrigues, Elisabeth Charlaix, and Joel Chevrier. Proximity effect on hydrodynamic interaction between a sphere and a plane measured by Force Feedback Microscopy at different frequencies. *arXiv:1505.06566 [cond-mat, physics:physics]*, May 2015. arXiv: 1505.06566.

[83] Q Zhong, K Kjoller, and V B Ehngs. Fractured polymer/silica fiber surface studied by tapping mode atomic force microscopy. *Surface Science Letters*, 290:688–692, December 1992.

[84] D Anselmetti, R Luthi, E Meyert, T Richmond, M Dreier, E Frommer, and H-J Guntherodt. Attractive-mode imaging of biological materials with dynamic force microscopy. *Nanotechnology*, 5:87–94, September 1995.

[85] P. K. Hansma, J. P. Cleveland, M. Radmacher, D. A. Walters, P. E. Hillner, M. Bezanilla, M. Fritz, D. Vie, H. G. Hansma, C. B. Prater, J. Massie, L. Fukunaga, J. Gurley, and V. Elings. Tapping mode atomic force microscopy in liquids. *Appl. Phys. Lett.*, 64(13):1738–1740, March 1994.

[86] Constant A. J. Putman, Kees O. Van der Werf, Bart G. De Grooth, Niek F. Van Hulst, and Jan Greve. Tapping mode atomic force microscopy in liquid. *Appl. Phys. Lett.*, 64(18):2454–2456, May 1994.

[87] T. E. Schäffer, J. P. Cleveland, F. Ohnesorge, D. A. Walters, and P. K. Hansma. Studies of vibrating atomic force microscope cantilevers in liquid. *Journal of Applied Physics*, 80(7):3622–3627, October 1996.

[88] Daniel Kiracofe and Arvind Raman. Quantitative force and dissipation measurements in liquids using piezo-excited atomic force microscopy: a unifying theory. *Nanotechnology*, 22(48):485502, December 2011.

[89] B. Rogers, D. York, N. Whisman, M. Jones, K. Murray, J. D. Adams, T. Sulchek, and S. C. Minne. Tapping mode atomic force microscopy in liquid with an insulated piezoelectric microactuator. *Review of Scientific Instruments*, 73(9):3242–3244, September 2002.

[90] Abdelhamid Maali, Cedric Hurth, Touria Cohen-Bouhacina, Gérard Couturier, and Jean-Pierre Aimé. Improved acoustic excitation of atomic force microscope cantilevers in liquids. *Appl. Phys. Lett.*, 88(16):163504, April 2006.

[91] C. Carrasco, P. Ares, P. J. de Pablo, and J. Gómez-Herrero. Cutting down the forest of peaks in acoustic dynamic atomic force microscopy in liquid. *Review of Scientific Instruments*, 79(12):126106, December 2008.

[92] Hitoshi Asakawa and Takeshi Fukuma. Spurious-free cantilever excitation in liquid by piezoactuator with flexure drive mechanism. *Review of Scientific Instruments*, 80(10):103703, October 2009.

[93] N. Umeda. Scanning attractive force microscope using photothermal vibration. *J. Vac. Sci. Technol. B*, 9(2):1318, March 1991.

[94] Glenn C. Ratcliff, Dorothy A. Erie, and Richard Superfine. Photothermal modulation for oscillating mode atomic force microscopy in solution. *Appl. Phys. Lett.*, 72(15):1911–1913, April 1998.

[95] D. Ramos, J. Tamayo, J. Mertens, and M. Calleja. Photothermal excitation of microcantilevers in liquids. *Journal of Applied Physics*, 99(12):124904, June 2006.

[96] A. Labuda, K. Kobayashi, D. Kiracofe, K. Suzuki, P. H. Grütter, and H. Yamada. Comparison of photothermal and piezoacoustic excitation methods for frequency and phase modulation atomic force microscopy in liquid environments. *AIP Advances*, 1(2):022136, 2011.

[97] Simon Carpentier. *Caractérisation à l'échelle micro/nanométrique par Force Feedback Microscope.* PhD thesis, Université Grenoble Alpes, Grenoble, 2016.

[98] Ken-ichi Umeda, Kei Kobayashi, Kazumi Matsushige, and Hirofumi Yamada. Direct actuation of cantilever in aqueous solutions by electrostatic force using high-frequency electric fields. *Appl. Phys. Lett.*, 101(12):123112, September 2012.

[99] Aleksander Labuda, Jason Cleveland, Nicholas A Geisse, Marta Kocun, Ben Ohler, Roger Proksch, Mario B Viani, and Deron Walters. Photothermal excitation for improved cantilever drive performance in tapping mode atomic force microscopy. page 6, 2014.

[100] Ernst-Ludwig Florin, Manfred Radmacher, Bernhard Fleck, and Hermann E. Gaub. Atomic force microscope with magnetic force modulation. *Review of Scientific Instruments*, 65(3):639–643, March 1994.

[101] Luca Costa. *The Force Feedback Microscope: an AFM for soft condensed matter*. PhD thesis, Université Grenoble Alpes, Grenoble, June 2014.

[102] Elena T. Herruzo and Ricardo Garcia. Frequency response of an atomic force microscope in liquids and air: Magnetic versus acoustic excitation. *Appl. Phys. Lett.*, 91(14):143113, October 2007.

[103] Bharat Bhushan, Ashok V. Kulkarni, Wayne Bonin, and Jerzy T. Wyrobek. Nanoindentation and picoindentation measurements using a capacitive transducer system in atomic force microscopy. *Philosophical Magazine A*, 74(5):1117–1128, November 1996.

[104] Marc P. Scherer, Gerhard Frank, and Anthony W. Gummer. Experimental determination of the mechanical impedance of atomic force microscopy cantilevers in fluids up to 70 kHz. *Journal of Applied Physics*, 88(5):2912–2920, September 2000.

[105] Raphaelle Dianoux. *Injection et détection de charges dans des nanostructures semiconductrices par Microscopie à Force Atomique*. PhD thesis, Université Joseph Fourrier, Grenoble, March 2005.

[106] M Nonnenmacher, M P O'Boyle, and H K Wickramasinghe. Kelvin probe force microscopy. *Applied Physics Letters*, 58(25):2921–2923, July 1991.

[107] A.B. Cook, Z. Barrett, S.B. Lyon, H.N. McMurray, J. Walton, and G. Williams. Calibration of the scanning Kelvin probe force microscope under controlled environmental conditions. *Electrochimica Acta*, 66:100–105, April 2012.

[108] Emmanuel Rousseau, Alessandro Siria, Guillaume Jourdan, Sebastian Volz, Fabio Comin, Joël Chevrier, and Jean-Jacques Greffet. Radiative heat transfer at the nanoscale. *Nature Photon*, 3(9):514–517, September 2009.

[109] P. J. van Zwol, L. Ranno, and J. Chevrier. Tuning Near Field Radiative Heat Flux through Surface Excitations with a Metal Insulator Transition. *Phys. Rev. Lett.*, 108(23):234301, June 2012.

[110] P. J. van Zwol, L. Ranno, and J. Chevrier. Emissivity measurements with an atomic force microscope. *Journal of Applied Physics*, 111(6):063110, March 2012.

[111] Constant A. J. Putman, Bart G. De Grooth, Niek F. Van Hulst, and Jan Greve. A detailed analysis of the optical beam deflection technique for use in atomic force microscopy. *Journal of Applied Physics*, 72(1):6–12, July 1992.

[112] Guillaume Jourdan. *Vers un microscope de force de Casimir: mesure quantitative de forces faibles et nanopositionnement absolu.* PhD thesis, Université Joseph Fourrier, Grenoble, 2007.

[113] M. Stark. Marking the Difference: Interferometric Detection vs Optical Beam Deflection in AFM. In *AIP Conference Proceedings*, volume 696, pages 385–391, Eindhoven, Netherlands, 2003. AIP.

[114] D. Rugar, H. J. Mamin, and P. Guethner. Improved fiber-optic interferometer for atomic force microscopy. *Appl. Phys. Lett.*, 55(25):2588–2590, December 1989.

[115] N A Burnham, X Chen, C S Hodges, G A Matei, E J Thoreson, C J Roberts, M C Davies, and S J B Tendler. Comparison of calibration methods for atomic-force microscopy cantilevers. *Nanotechnology*, 14(1):1–6, January 2003.

[116] Akihiro Torii, Minoru Sasaki, Kazuhiro Hane, and Shigeru Okuma. A method for determining the spring constant of cantilevers for atomic force microscopy. *Meas. Sci. Technol.*, 7(2):179–184, February 1996.

[117] J. P. Cleveland, S. Manne, D. Bocek, and P. K. Hansma. A nondestructive method for determining the spring constant of cantilevers for scanning force microscopy. *Review of Scientific Instruments*, 64(2):403–405, February 1993.

[118] John E. Sader, Ian Larson, Paul Mulvaney, and Lee R. White. Method for the calibration of atomic force microscope cantilevers. *Review of Scientific Instruments*, 66(7):3789–3798, July 1995.

[119] John Elie Sader. Frequency response of cantilever beams immersed in viscous fluids with applications to the atomic force microscope. *Journal of Applied Physics*, 84(1):64–76, July 1998.

[120] Jeffrey L. Hutter and John Bechhoefer. Calibration of atomic-force microscope tips. *Review of Scientific Instruments*, 64(7):1868–1873, July 1993.

[121] Hans-Jürgen Butt and Manfred Jaschke. Calculation of thermal noise in atomic force microscopy. *Nanotechnology*, 6:1–7, 1995.

[122] Tobias Pirzer and Thorsten Hugel. Atomic force microscopy spring constant determination in viscous liquids. *Review of Scientific Instruments*, 80(3):035110, March 2009.

[123] Justine Laurent, Audrey Steinberger, and Ludovic Bellon. Functionalized AFM probes for force spectroscopy: eigenmodes shape and stiffness calibration through thermal noise measurements. *Nanotechnology*, 24(22):225504, June 2018. arXiv: 1302.2583.

[124] J. Laurent, H. Sellier, A. Mosset, S. Huant, and J. Chevrier. Casimir force measurements in Au-Au and Au-Si cavities at low temperature. *Phys. Rev. B*, 85(3):035426, January 2012.

[125] G. Jourdan, A. Lambrecht, F. Comin, and J. Chevrier. Quantitative non-contact dynamic Casimir force measurements. *Europhys. Lett.*, 85(3):31001, February 2009.

[126] J.R. Taylor. *Classical Mechanics.* University Science Books, 2005.

[127] E. Durand. *Electrostatique, Vol. 2: Problèmes Généraux Conducteurs.* May 1967.

[128] L Boyer, F Houze, A Tonck, J L Loubet, and J M Georges. The influence of surface roughness on the capacitance between a sphere and a plane. *J. Phys. D: Appl. Phys.*, 27(7):1504–1508, July 1994.

[129] M. Morita, T. Ohmi, E. Hasegawa, M. Kawakami, and M. Ohwada. Growth of native oxide on a silicon surface. *Journal of Applied Physics*, 68(3):1272–1281, August 1990.

[130] Raymond M Hakim, Ronald G Olivier, and Hugues St-Onge. The dielectric properties of silicone fluids. *IEEE Trans. Electr. Insul*, (5):11, 1977.

[131] Sissi de Beer, Dirk van den Ende, and Frieder Mugele. Atomic force microscopy cantilever dynamics in liquid in the presence of tip sample interaction. *Appl. Phys. Lett.*, 93(25):253106, December 2008.

[132] M. Gouy. Sur la constitution de la charge électrique à la surface d'un électrolyte. *J. Phys. Theor. Appl.*, 9(1):457–468, 1910.

[133] David Leonard Chapman. A contribution to the theory of electrocapillarity. *The London, Edinburgh, and Dublin Philosophical Magazine and Journal of Science*, 25(148):475–481, April 1913.

[134] O. Stern. Zur theorie der elektrischen doppelschicht. *Zeitschrift fur elektrochemie*, 30:9, 1924.

[135] R. Buchner, J. Barthel, and J. Stauber. The dielectric relaxation of water between 0°C and 35°C. *Chemical Physics Letters*, 306(1-2):57–63, June 1999.

[136] Ting Chen, Glenn Hefter, and Richard Buchner. Dielectric Spectroscopy of Aqueous Solutions of KCl and CsCl. *J. Phys. Chem. A*, 107(20):4025–4031, May 2003.

[137] W. M. Haynes. *CRC Handbook of Chemistry and Physics*. CRC Press, Cleveland, Ohio, 71 edition, 1977.

[138] Yifei Wang, S. R. Narayanan, and Wei Wu. Field-Assisted Splitting of Pure Water Based on Deep-Sub-Debye-Length Nanogap Electrochemical Cells. *ACS Nano*, 11(8):8421–8428, August 2017.

[139] Badih El-Kareh and Lou N. Hutter. *Fundamentals of semiconductor processing technology*. Springer US, New York, NY, 1 edition, 1995. OCLC: 939472719.

[140] Omar Azzaroni. Polymer brushes here, there, and everywhere: Recent advances in their practical applications and emerging opportunities in multiple research fields. *J. Polym. Sci. A Polym. Chem.*, 50(16):3225–3258, August 2012.

[141] Tao Chen, Robert Ferris, Jianming Zhang, Robert Ducker, and Stefan Zauscher. Stimulus-responsive polymer brushes on surfaces: Transduction mechanisms and applications. *Progress in Polymer Science*, 35(1-2):94–112, January 2010.

[142] E Gil and S Hudson. Stimuli-reponsive polymers and their bioconjugates. *Progress in Polymer Science*, 29(12):1173–1222, December 2004.

[143] Igor Luzinov, Sergiy Minko, and Vladimir V Tsukruk. Adaptive and responsive surfaces through controlled reorganization of interfacial polymer layers. *Progress in Polymer Science*, 29(7):635–698, July 2004.

[144] Martin A. Cole, Nicolas H. Voelcker, Helmut Thissen, and Hans J. Griesser. Stimuli-responsive interfaces and systems for the control of protein–surface and cell–surface interactions. *Biomaterials*, 30(9):1827–1850, March 2009.

[145] H.G. Schild. Poly(N-isopropylacrylamide): experiment, theory and application. *Progress in Polymer Science*, 17(2):163–249, January 1992.

[146] R. Steitz, V. Leiner, K. Tauer, V. Khrenov, and R. v. Klitzing. Temperature-induced changes in polyelectrolyte films at the solid-liquid interface. *Applied Physics A: Materials Science & Processing*, 74(0):s519–s521, December 2002.

[147] Diane Goodman, Jayachandran N. Kizhakkedathu, and Donald E. Brooks. Attractive Bridging Interactions in Dense Polymer Brushes in Good Solvent Measured by Atomic Force Microscopy. *Langmuir*, 20(6):2333–2340, March 2004.

[148] K Kato. Polymer surface with graft chains. *Progress in Polymer Science*, 28(2):209–259, February 2003.

[149] Kenichi Nagase, Jun Kobayashi, and Teruo Okano. Temperature-responsive intelligent interfaces for biomolecular separation and cell sheet engineering. *J. R. Soc. Interface*, 6, June 2009.

[150] X. Zhu, C. Yan, F. M. Winnik, and D. Leckband. End-Grafted Low-Molecular-Weight PNIPAM Does Not Collapse above the LCST. *Langmuir*, 23(1):162–169, January 2007.

[151] Ibrahim Bou Malham and Lionel Bureau. Density effects on collapse, compression and adhesion of thermoresponsive polymer brushes. *arXiv:0909.3709 [cond-mat]*, September 2009. arXiv: 0909.3709.

[152] Franck Montagne, Jérome Polesel-Maris, Raphael Pugin, and Harry Heinzelmann. Poly(*N* -isopropylacrylamide) Thin Films Densely Grafted onto Gold Surface: Preparation, Characterization, and Dynamic AFM Study of Temperature-Induced Chain Conformational Changes. *Langmuir*, 25(2):983–991, January 2009.

[153] Yunlong Yu, Bernard D. Kieviet, Fei Liu, Igor Siretanu, Edit Kutnyánszky, G. Julius Vancso, and Sissi de Beer. Stretching of collapsed polymers causes an enhanced dissipative response of PNIPAM brushes near their LCST. *Soft Matter*, 11(43):8508–8516, 2015.

[154] Satoru Kidoaki, Shoji Ohya, Yasuhide Nakayama, and Takehisa Matsuda. Thermoresponsive Structural Change of a Poly(N-isopropylacrylamide) Graft Layer Measured with an Atomic Force Microscope. *Langmuir*, 17(8):2402–2407, April 2001.

[155] Xiaofeng Sui, Qi Chen, Mark A. Hempenius, and G. Julius Vancso. Probing the Collapse Dynamics of Poly(N-isopropylacrylamide) Brushes by AFM: Effects of Co-nonsolvency and Grafting Densities. *Small*, 7(10):1440–1447, May 2011.

[156] Naoyuki Ishida and Simon Biggs. Direct Observation of the Phase Transition for a Poly(*N* -isopropylacryamide) Layer Grafted onto a Solid Surface by AFM and QCM-D. *Langmuir*, 23(22):11083–11088, October 2007.

[157] D.H. Napper. Steric Stabilization. *Journal of Colloid and Interface Science*, 58(2):390–407, February 1977.

[158] Xuanhong Cheng, Heather E. Canavan, M. Jeanette Stein, James R. Hull, Sasha J. Kweskin, Matthew S. Wagner, Gabor A. Somorjai, David G. Castner, and Buddy D. Ratner. Surface Chemical and Mechanical Properties of Plasma-Polymerized *N* - Isopropylacrylamide. *Langmuir*, 21(17):7833–7841, August 2005.

[159] E.M. Benetti, S. Zapotoczny, and G.J. Vancso. Tunable Thermoresponsive Polymeric Platforms on Gold by Photoiniferter-Based Surface Grafting. *Adv. Mater.*, 19(2):268–271, January 2007.

[160] Andrew A. Brown, Neelam S. Khan, Lorenz Steinbock, and Wilhelm T.S. Huck. Synthesis of oligo(ethylene glycol) methacrylate polymer brushes. *European Polymer Journal*, 41(8):1757–1765, August 2005.

[161] Phanindhar Shivapooja, Linnea K. Ista, Heather E. Canavan, and Gabriel P. Lopez. ARGET–ATRP Synthesis and Characterization of PNIPAAm Brushes for Quantitative Cell Detachment Studies. *Biointerphases*, 7(1):32, December 2012.

[162] Siddhartha Varma, Lionel Bureau, and Delphine Débarre. The Conformation of Thermoresponsive Polymer Brushes Probed by Optical Reflectivity. *Langmuir*, 32(13):3152–3163, April 2016.

[163] Ricardo García and Alvaro San Paulo. Dynamics of a vibrating tip near or in intermittent contact with a surface. *Phys. Rev. B*, 61(20):R13381–R13384, May 2000.

[164] Marian Kaholek, Woo-Kyung Lee, Sang-Jung Ahn, Hongwei Ma, Kenneth C. Caster, Bruce LaMattina, and Stefan Zauscher. Stimulus-Responsive Poly(*N* - isopropylacrylamide) Brushes and Nanopatterns Prepared by Surface-Initiated Polymerization. *Chem. Mater.*, 16(19):3688–3696, September 2004.

[165] Karl Terzaghi. Erdbaumechanik auf bodenphysikalischer Grundlage. *F. Deuticke*, page 399, 1925.

[166] Ivan Th. Rosenqvist. Remarks to the Mechanical Properties of Soil Water Systems. *Geologiska Föreningen i Stockholm Förhandlingar*, 80(4):435–457, November 1958.

[167] Haydn H Murray. Traditional and new applications for kaolin, smectite, and palygorskite: a general overview. *Applied Clay Science*, 17(5-6):207–221, November 2000.

[168] Faïza Bergaya, editor. *Handbook of clay science*. Number 1 in Developments in clay science. Elsevier, Amsterdam, 1. ed., reprint edition, 2008. OCLC: 845249284.

[169] P Y Hicher, H Wahyudi, and D Tessier. Microstructural analysis of inherent and induced anisotropy in clay. page 31, 2000.

[170] Y H Wang and W K Siu. Structure characteristics and mechanical properties of kaolinite soils. I. Surface charges and structural characterizations. *Can. Geotech. J.*, 43(6):587–600, June 2006.

[171] Georgios Birmpilis, Reza Ahmadi-Naghadeh, and Jelke Dijkstra. Towards a methodology for the characterisation of the fabric of wet clays using X-ray scattering. *E3S Web Conf.*, 92:01005, 2019.

[172] Amer Deirieh, Irene Y. Chang, Michael L. Whittaker, Steven Weigand, Denis Keane, James Rix, John T. Germaine, Derk Joester, and Peter B. Flemings. Particle arrangements in clay slurries: The case against the honeycomb structure. *Applied Clay Science*, 152:166–172, February 2018.

[173] James Mitchell and Kenichi Soga. *Fundamentals of Soil Behaviour*. Wiley, 3rd edition, May 2005.

[174] V.M. Goldschmidt. Undersokelser over lersedimenter. *Nordisk Jordbrugs Forskuing*, 4(7):435–445, 1926.

[175] t.w. Lambe. The structure of inorganic soil. *Proc. Am. Soc. Civ. Eng.*, 79:1–49, 1953.

[176] H van Olphen. Internal mutual flocculation in clay suspensions. *Journal of Colloid Science*, 19(4):313–322, April 1964.

[177] R.K Khandal and Th.F Tadros. Application of viscoelastic measurements to the investigation of the swelling of sodium montmorillonite suspensions. *Journal of Colloid and Interface Science*, 125(1):122–128, September 1988.

[178] A Casagrande. The structure of clay and its importance in foundation engineering. *Boston Society Civil Engineering Journal*, 19(4):168–209, 1932.

[179] Armin von Weiss and R Frank. Über den Bau der Gerüste in thixotropen Gelen. *Zeitschrift für Naturforschung*, 16(b):141–142, October 1961.

[180] K. Norrish. The swelling of montmorillonite. *Discuss. Faraday Soc.*, 18:120, 1954.

[181] I. C. Callaghan and R. H. Ottewill. Interparticle forces in montmorillonite gels. *Faraday Discuss. Chem. Soc.*, 57:110, 1974.

[182] Neal R. O'Brien. Fabric of Kaolinite and Illite Floccules. *Clays and Clay Minerals*, 19(6):353–359, 1971.

[183] V. I. Osipov and V. N. Sokolov. Relation between the microfabric of clay soils and their origin and degree of compaction. *Bulletin of the International Association of Engineering Geology*, 18(1):73–81, December 1978.

[184] Janusz Stawiński. Influence of Calcium and Sodium Concentration on the Microstructure of Bentonite and Kaolin. *Clays and Clay Minerals*, 38(6):617–622, 1990.

[185] Marek S. Zbik, Roger St.C. Smart, and Gayle E. Morris. Kaolinite flocculation structure. *Journal of Colloid and Interface Science*, 328(1):73–80, December 2008.

[186] Jianhua Du, Rada A. Pushkarova, and Roger St.C. Smart. A cryo-SEM study of aggregate and floc structure changes during clay settling and raking processes. *International Journal of Mineral Processing*, 93(1):66–72, September 2009.

[187] Gayle E. Morris and Marek S. Żbik. Smectite suspension structural behaviour. *International Journal of Mineral Processing*, 93(1):20–25, September 2009.

[188] Jianhua Du, Gayle Morris, Rada A. Pushkarova, and Roger St. C. Smart. Effect of Surface Structure of Kaolinite on Aggregation, Settling Rate, and Bed Density. *Langmuir*, 26(16):13227–13235, August 2010.

[189] G.J. Meijer. *Reconstitution of sensitive clays*. PhD thesis, TU Delft, Delft, October 2012.

[190] Roland Pusch. Quick-clay microstructure. *Eng. Geo.*, 1(6):433–443, August 1966.

[191] Gertjan Meijer and Jelke Dijkstra. A novel methodology to regain sensitivity of quick clay in a geotechnical centrifuge. *Can. Geotech. J.*, 50(9):995–1000, September 2013.

[192] Pierre Delage and Guy Lefebvre. Study of the structure of a sensitive Champlain clay and of its evolution during consolidation. 21:15, 1984.

[193] Yves F Dufrêne, Christophe J.P Boonaert, Henny C van der Mei, Henk J Busscher, and Paul G Rouxhet. Probing molecular interactions and mechanical properties of microbial cell surfaces by atomic force microscopy. *Ultramicroscopy*, 86(1-2):113–120, January 2001.

[194] M.J. Doktycz, C.J. Sullivan, P.R. Hoyt, D.A. Pelletier, S. Wu, and D.P. Allison. AFM imaging of bacteria in liquid media immobilized on gelatin coated mica surfaces. *Ultramicroscopy*, 97(1-4):209–216, October 2003.

[195] Michael Krieg, Gotthold Fläschner, David Alsteens, Benjamin M. Gaub, Wouter H. Roos, Gijs J. L. Wuite, Hermann E. Gaub, Christoph Gerber, Yves F. Dufrêne, and Daniel J. Müller. Atomic force microscopy-based mechanobiology. *Nat Rev Phys*, 1(1):41–57, January 2019.

[196] Jun Long, Zhenghe Xu, and Jacob H. Masliyah. Role of illite–illite interactions in oil sands processing. *Colloids and Surfaces A: Physicochemical and Engineering Aspects*, 281(1-3):202–214, June 2006.

[197] Bo Feng, Hanyi Liu, Yingli Li, Xinmin Liu, Rui Tian, Rui Li, and Hang Li. AFM measurements of Hofmeister effects on clay mineral particle interaction forces. *Applied Clay Science*, 186:105443, March 2020.

[198] Y. Martin, C. C. Williams, and H. K. Wickramasinghe. Atomic force microscope–force mapping and profiling on a sub 100-Å scale. *Journal of Applied Physics*, 61(10):4723–4729, May 1987.

[199] Karin Rankka, Yvonne Andersson-Sköld, Carina Hultén, Rolf Larsson, Virginie Leroux, and Torleif Dahlin. Quick clay in Sweden. Technical Report 65, Statens Geotekniska Institut, Linköping, 2004.

[200] Yvonne Andersson-Sköld, J. Kenneth Torrance, Bo Lind, Karin Odén, Rodney L. Stevens, and Karin Rankka. Quick clay—A case study of chemical perspective in Southwest Sweden. *Engineering Geology*, 82(2):107–118, December 2005.

[201] Mats Karlsson, Arnfinn Emdal, and Jelke Dijkstra. Consequences of sample disturbance when predicting long-term settlements in soft clay. *Can. Geotech. J.*, 53(12):1965–1977, December 2016.